TRANSONIC LIFT AUGMENTATION OF TWO-DIMENSIONAL SUPERCRITICAL AEROFOILS BY MEANS OF AFT CAMBER, SLOT BLOWING AND JET FLAPS, IN HIGH REYNOLDS NUMBER FLOW

D.J. Peake*, A.J. Bowker, M. Mokry
National Aeronautical Establishment
National Research Council of Canada
Ottawa, Ontario, Canada

and

H. Yoshihara*, R. Magnus
Convair Aerospace Division of General Dynamics
San Diego, California, U.S.A.

Abstract

A series of experiments has been run at NAE, at chord Reynolds numbers close to 30 million, to determine how best to augment lift on two-dimensional supercritical aerofoils in transonic flow. The means chosen were deflecting the aft camber line in conjunction with slot blowing, and the use of jet flaps. Measurements included wing pressures and forces, wake profiles, and static pressures adjacent to the tunnel ceiling and floor, to assist in estimating wind tunnel wall interference effects.

It was demonstrated that the jet flap in conjunction with slot blowing provided the best lifting performance, yielding maximum lift coefficients around 1.5 at Mach 0.85, with blowing momentum coefficients of 0.02.

1.0 Introduction

The goal of the present study was to find effective means by which the design lift coefficients of high performance, two-dimensional aerofoils, could be augmented in transonic flow, for such augmentation from aerodynamic control devices offers potential improvements to the manoeuvrability of aircraft. If the development of the additional lift were sufficiently responsive and effective throughout the desired lift range, then it might also be used to control lateral instabilities and prevent entry into "post-stall" gyrations. Furthermore, if large lifts could be obtained by either active or passive means, was it possible to generate these high lifts without substantial increments in drag?

The maximum lift that can be produced by an aerofoil in transonic flow is curtailed sooner or later by the appearance of boundary-layer separation on the aerofoil upper surface, either at the leading-edge, or at points close to or downstream of the shock wave. At the higher subsonic Mach numbers of interest to us, extensive separation resulting from the pressure rise through a relatively strong shock wave (which usually causes undesirable buffetting) is responsible for the bounding of the lift, since the appearance of leading-edge separation may generally be offset by a blunting or cambering of the nose. It is thus the separations generated by shock waves upon which we must focus our attention in our search to increase the aerofoil lift.

The incorporation of aft camber into an aerofoil profile is a proven means to extend the upper limit of usable lift. The important effects of the aft camber on the aerofoil pressure distribution are, the generation of increased positive pressure coefficients across the lower surface of the aerofoil; added suction pressures over the nose of the upper surface; and a significant displacement downstream of the upper surface shock wave; all of which contribute to the lift production without increasing the strength of the shock wave. With the use of aft camber, a given (large) lift can be achieved at a much lower angle of incidence than if incidence alone were used to produce the lift. Consequently, the onset of boundary-layer separation can be delayed, and greater maximum lift coefficients with smaller drags should result.

The amount of aft camber that can be employed has its limit, since separation of the upper surface boundary layer will eventually take place near the trailing-edge, and will be hastened, in all likelihood, by the presence of shock wave/boundary-layer interactions further upstream. The outcome of any separation upstream of the trailing-edge is to reduce the effective aft camber due to the substantial increase in boundary-layer displacement thickness; in turn, such reduction of the effective aft camber will promote an upstream movement of the shock wave on the upper surface that will cause a decrease of the lift. The form drag will also increase substantially.

We have seen that in transonic flow, a means to achieve an increased effective aft camber without incurring the above effects of boundary-layer separation, is the use of jet flaps.[1] Lift augmentation by the jet flap is produced in an analogous way to that of 'solid' aft camber, but, in addition, increased suction pressures are generated over the upper aft surface downstream of the shock wave. Communication of pressures between the upper and lower surfaces near the trailing-edge is prevented by the jet sheet, which curves in such a way as to balance the forces generated by the local pressure field. Hence, although the flow should still depart smoothly from the aerofoil trailing-edge, the requirement that the trailing-edge pressure recover to the same level on either side of the trailing-edge is not necessary because of the effective extension of the camber-line by the jet sheet. The existence of the aft suction pressures on the top surface of the aerofoil contributes to the lift, but it also adds a nose-down increment to the pitching moment. These suction pressures also tend to increase the pressure drag, because of their action on rearward facing surface elements. Moreover, a thrust recovery equivalent to a large

*Senior Authors

fraction of the jet flap momentum coefficient is not realised,[2] the cause for which is suggested to be the thrust loss associated with the mixing that occurs between the jet and the mainstream, especially within the pressure field of the wing, as proposed by Stratford for the jet flap in subcritical flow.[3] The manner in which the thrust or drag increments are induced on the aerofoil may be viewed in the light of the sink effect produced by the jet in its absorption of the external flow.

One other means to extend the effectiveness of aft cambering is to employ boundary-layer control by tangential slot blowing to suppress or destroy the effects of separation.[4,5,6] The utilisation of the auxiliary air supply in the boundary-layer control mode might well be more effective than in the jet flap mode, particularly when there are limitations on the air supply; because the available jet momentum coefficient, C_μ, might be adequate to suppress the separation effects arising from a given increase of 'solid' aft camber, but inadequate to cope with the separation on the upper surface when operating in the jet flap mode. Perhaps a combination of the jet flap with slot blowing would produce the most benefit.

In order to determine the relative effectiveness of the various means of augmenting lift that we have introduced above, a third series of tests to supplement earlier work[1,7] was conducted in the NAE 15-inch × 60-inch two-dimensional high Reynolds number wind tunnel. The bulk of the tests was carried out at nominal Mach numbers, M_∞, of 0.75, 0.80 and 0.85, at a constant Reynolds number, R_c, of 30 million based on the aerofoil chord and tunnel mainstream conditions. In addition, some further tests were attempted at Mach numbers both higher and lower than the above values to determine wall interference parameters.

Figures 1 and 2 illustrate the types of aerofoil section of interest to us. The base aerofoil design shown on these figures possessed a thickness/chord ratio of ten percent, with a "peaky nose" and a modest aft camber deflection of about 10 degrees at the trailing-edge, that would be suitable for cruise. To provide the jet flap, a sonic nozzle was incorporated into the lower surface of the aerofoil, just upstream of the trailing-edge, with an initial jet flap angle of $\theta_j = 85$ degrees relative to the aerofoil chord line. This aerofoil was designated as configuration I with no blowing, and configuration IJ with blowing. It was essentially the same aerofoil that was tested earlier[1] with $\theta_j = 30$ and 85 degrees; but on this occasion, an additional jet flap angle of 120 degrees was also investigated - see Figure 3.2. The second aerofoil on Figure 1, labelled configuration II, was identical with Aerofoil I forward of the 70 percent chord station, but a greater aft camber with a trailing-edge angle of about 20 degrees, was incorporated aft of the 70 percent station, by changing a removable trailing-edge section. Aerofoil II was provided with a slot blowing nozzle on the upper surface at the 80 percent chord station, as well as with a jet flap nozzle of the same configuration as Aerofoil I: see Figure 3.3. Aerofoil II was tested in the slot blowing mode (called IIS) as well as in the combined slot and jet flap blowing modes (IISJ). Aerofoil II in the jet flap mode (IIJ) was tested earlier,[7] and some of the previous results are used herein for comparison.

The third aerofoil configuration from which measurements were gathered, called IF2J, was a hybrid configuration having the Aerofoil I upper surface and the Aerofoil II lower surface, but with a jet flap incorporated to exhaust across the resulting enlargement in base area, as shown on Figure 3.1.

In all runs, aerofoil surface pressure distributions and force and moment measurements from sidewall balances were obtained, as well as wake surveys at three spanwise stations. Static pressure distributions near both the perforated ceiling and floor of the wind tunnel were also measured using pressure orifices mounted on thin rails along the tunnel centre-line, which projected two inches from the walls into the stream.

The NAE tunnel is equipped with top and bottom perforated walls of 20.5 percent porosity (open to total area ratio), so that we would expect wall interference effects somewhere between those obtained when testing in an open jet environment and those obtained when using a solid wall. This implies that the major correction should be a reduction in angle of attack of the aerofoil, with a negligible correction to the mainstream Mach number. In References 1 and 8, a procedure was proposed to obtain the incidence correction via a streamwise momentum analysis, assuming that the blockage correction was negligible. Such a procedure was devised, because it was felt that at the higher Mach numers of the tests, conventional wall interference corrections[9,10] deduced using subsonic linearised theory, were inappropriate. An important adjunct of the present investigation, in fact, has been a comparison between angle of attack corrections calculated using the momentum method, and an updated subcritical flow theory[11] (for test results up to M_∞ of about 0.8) in which different porosity factors are derived for the tunnel floor and ceiling, by comparing calculated pressure distributions near the tunnel walls with experimental pressure measurements at the same locations. Thirdly, the finite difference procedure of Reference 12 together with the measured pressure distributions along the aerofoil and the walls have also been used to calculate as a spot check the angle of attack and blockage corrections at one incidence and Mach number. Here the procedure has been to find an aerofoil pressure distribution in free air that matches the measured aerofoil pressure distribution in the wind tunnel; and secondly, to calculate the free air pressure distribution at the same geometric incidence as in the wind tunnel flow. Results from the three methods are discussed in Section 6.0.

In summary, we may quote the objectives of the present study as:

(a) To determine in the wind tunnel at high Reynolds numbers, the relative merits of 'solid' aft camber, jet flaps, and upper aft surface boundary-layer control by tangential blowing from a slot, applied separately or in combination, to extend the buffet onset boundaries. The assessment will include a review of the resulting lift/drag polars and lift/pitching moment performance. In addition, to obtain measurements of fluctuating pressure levels on the wing and in the mainstream at lift coefficients representative of cruise and buffet onset.

(b) To obtain details of the shock-induced separations and separations near the trailing-edge at

high lifts and high Reynolds numbers, insofar as they can be inferred from interpreting the wing pressure distributions and wake flows.

(c) To examine the wall interference effects using a streamwise momentum method,[8] a new subcritical theory[11] and the solution of the transonic flow field by the finite difference procedure of Magnus and Yoshihara,[12] the second and third techniques utilising the static pressures measured adjacent to the tunnel floor and ceiling.

2.0 The Test Facility

The basic NAE intermittent blowdown facility is the 60-inch × 60-inch trisonic wind tunnel, in which sidewall inserts are used within the transonic test section to form a 15-inch wide by 60-inch high two-dimensional test section. We note that the transonic test section is situated in tandem with the flexible nozzle section of the wind tunnel. An aerofoil model of 15-inches span is mounted in the test section mid-way between the ceiling and floor, the model interconnecting two sidewall balances in the port and starboard walls.

Figure 4 shows the installation of the '2-D insert' into the transonic working section where we observe the port side balance situated within an area of the sidewall devoted to suction boundary-layer control, and the 20.5 percent porosity, normal hole perforated top and bottom walls of the tunnel, that form the corresponding ceiling and floor of the 2-D test section.

The boundary layers on the solid sidewalls are controlled at two locations in the facility. First of all, at the entrance of the contraction to the 2-D insert, ram bleed ducts remove the approaching turbulent boundary layers that have grown along the nozzle sidewalls of the wind tunnel. Secondly, uniformly distributed suction is provided via 24-inch long by 18-inch high compressed steel screen, porous sections, situated in the insert sidewalls in the vicinity of the model, to control the end-wall constraint, in order to create uniform loading and boundary-layer growth across the aerofoil span. The clearances between the model and the sidewalls are sealed with spring-loaded nylon strips. The appropriate suction levels have been established[1,7] to provide confidence that nominally two-dimensional flow conditions are achieved in the tunnel, by observing oil dots on the wing surface streaking downstream parallel to the sidewalls, supplemented by the good agreement obtained between the sidewall balance and integrated surface pressure measurement values of normal force coefficient and quarter chord pitching moment coefficient. The optimum ratio of velocity normal to the sidewall compared with that of the tunnel mainstream is close to 0.55 percent, for parallelism of the flow up to the onset of buffetting.

Figure 5 demonstrates typical oil streak results for the basic aerofoil shown on Figure 1, at a test Mach number of 0.8 and a chord Reynolds number of 30 million. The first and second photographs on the left-hand side illustrate the upper and lower surfaces when $C_\mu = 0$. We note satisfactory parallelism of the surface shear stress trajectories except in the top surface corners in close proximity to the trailing-edge. The third and fourth photographs show that with the jet flap operating at $C_\mu \triangleq 0.02$ and 0.03, the uniformity is good across the entire upper surface.

We will comment briefly upon some additional indicators of flow two-dimensionality. Figure 6.1 for instance, reveals the good agreement obtained for several aerofoil configurations, between the normal force coefficients, that result from integrating the chordwise centre-line pressure distributions, C_{NP}, and from the sidewall balance measurements (measuring an overall effect across the span), C_{NB}. Even when the drag polars turn around as the onset of buffetting is approached, and the aerofoil wakes exhibit large spanwise three-dimensionalities - see the top graph of Figure 6.1 - the agreement between C_{NP} and C_{NB} remains relatively satisfactory. The plot on Figure 6.2 again demonstrates better than reasonable agreement between the integrated pressure and sidewall balance one-quarter chord pitching moment coefficients. Other indicators of flow two-dimensionality are shown on Figures 7.1 and 7.2. The spanwise pressure distributions at 20 percent and 60 percent chord stations on another supercritical aerofoil design similar to the section under review, appear on Figure 7.1, for the same optimum sidewall boundary-layer control rate, but at a mainstream Mach number of 0.84. We note that the distributions are plotted on an isometric graph with angle of attack, α_c, as a parameter. The spanwise uniformity is quite acceptable right up to the onset of buffetting after which gross three-dimensionality sets in. Figure 7.2 illustrates typical wake profiles measured one chord length downstream of Aerofoil I at $C_\mu = 0$. From the zero lift condition up to buffet onset, the records from the three spanwise stations yield profile drag coefficients within a spread of ±12 drag counts. The spiky appearance of the last profile is for an aerofoil setting past the onset of buffetting, when as we saw on Figure 7.1, spanwise uniformity over the aerofoil has broken down.

The resultant forces and moments on the aerofoil model are measured by the two, three-component sidewall balances, situated at the extremities of the wing. The total capacity of the balances is 20,000 lb.wt. normal force at zero pitching moment, to 22,500 lb.wt-inches pitching moment with zero normal force. The limit on the total applied axial force is 2000 lb.wt. Static calibration of the balances indicates that the balance output loads are measured to within 0.2 percent of the applied load, with a repeatability during tests of better than $\Delta C_{NB} = \pm 0.002$ and $\Delta C_{XB} = \pm 0.0003$ in the high subsonic flow régime, where C_{NB} and C_{XB} are the normal and axial force coefficients. With the model mounted on the balance pins in the wind tunnel, the possibility was also explored of interference and hysteresis on the balance outputs from the rigging of the pressure lines and the blowing system. Typical interference forces were within the band width ±3 lb.wt. and hysteresis within ±1 lb.wt. on the normal force outputs, which are very small compared with the full scale balance output. The interference on the axial force output was within ±2 lb.wt. with hysteresis in the band width ±0.3 lb.wt. Again, these latter values are no more than 0.1 percent of the maximum safe axial force. We note that typical balance loads in the wind tunnel were usually up to 30 to 50 percent of the full scale ratings for the flexures.

The model angle of incidence is provided by

driving the port sidewall balance in pitch, any variation in angle of incidence between the two ends of the wing being determined from incidence potentiometers on the port and starboard balance shafts. The level of twist between the two ends is generally inconsequential. At the maximum one-quarter pitching moment coefficient, the value of which may exceed -0.3, 0.1 degree of twist might typically be measured. At this pitching moment, for example, we are close to a C_{LMAX} of 1.5 for configuration IISJ.

The aerofoil and wall static pressures are measured by means of four fast-scan scanivalve/transducer modules located in the plenum chamber of the transonic test section. The ports of the scanivalves were sampled at a rate of twenty per second, which was determined to be an acceptable scan rate from the point of view of system response, due to the high absolute levels of static pressure that were used in the wind tunnel (between 125 psia and 46 psia). The aerofoil wake was surveyed in a plane 15-inches downstream of the aerofoil trailing-edge with a rake accommodating (for most of the tests) three total pressure probes at spanwise stations nearest the tunnel centre-line, and one disc static pressure probe, insensitive to pitch, at the inboard span station. 2.25 inches from the wall. Figure 8 shows the wake rake, and Figure 9, the disposition of the probes relative to the model wing. The static and pitot probes were interchangeable. Indeed, some additional tests were run, with three more calibrated disc static probes installed at the four stations on the wake rake, to investigate the uniformity of static pressure level across the semi-span of the wind tunnel (see Section 5.1). Traverses of the wake rake in the vertical plane were made between the limits of 19-inches above and 9-inches below the tunnel axis. At a given angle of incidence, simultaneous measurements were made of the wing pressure distribution, the wake pressure distributions, the wall pressure distributions and the balance forces and moments. The time for gathering this data was nominally three seconds, and five angles of incidence could typically be managed in any given tunnel run.

During a series of runs at $M_\infty \cong 0.8$ to measure the stream levels of pressure fluctuation, where the wing was kept at a constant angle of attack throughout the run, five wing pressure and wake rake scans were tried, to assess the repeatability of pressure data. The wing pressure scans showed remarkable agreement, while the wake rake profile drag coefficients repeated to within (typically) ±20 drag counts.

We comment next upon the static pressure measurements made close to the floor and ceiling of the 2-D insert. These were accomplished using two 80-inch long rails, shown on Figure 10 that were mounted to the wind tunnel ceiling and floor mid-way between the tunnel sidewalls.

The cross-sectional shape of the rail is shown on Figure 11. Because of the likelihood of outflow from the tunnel working section into the plenum chamber, each static pressure orifice was placed downstream of an elliptical nose (in the cross-flow sense), such that the orifice location was at a station where the cross-flow had returned to its oncoming value.[13] To cater for inflow from the plenum into the working section, the static hole was, in turn, kept at a reasonable distance from the tunnel wall, to reduce to a minimum the local effects of irregularities in the flow-field emerging from the normal hole perforations. (The calibration of the 2-D insert had shown that static pressures measured at the locations in the solid wall between the normal hole perforations, were subject to large disturbances, resulting from local flow non-uniformities.[14]) The base of each rail covered only one line of perforations in the ceiling and the floor.

Of substantial interest has been the low frequency fluctuation levels of the static and total pressures in the tunnel mainstream, and the static pressure upon the wing, during cruise operation of the aerofoil and at the onset of buffetting. To accommodate the mainstream measurements, a special sturdy pitot-static probe was designed, and is shown on Figure 12. The probe incorporated tuned differential pressure transducers being located in close proximity to one another. Each transducer differential output was required to be that due only to the pressure fluctuations, so that a rapid roll-off in response to fluctuating signal levels above 10 Hz was necessary for the reference side of each transducer. The roll-off was accomplished by tuning a variable volume in the reference line in series with a suitable orifice diameter at the reference pressure port, using a horn driver at nominally atmospheric pressure conditions. As an example, Figure 13 shows the frequency response of the fluctuation pitot pressure transducer, the differential output being reasonably flat between 20 Hz and 1000 Hz, in the frequency range of interest. Previous microphone tests[7,15] in the tunnel upstream of the 2-D contraction section had provided narrow band spectra to suggest that, peak noise outputs were in the 30 to 40 Hz range, which were thought to result from low frequency eddying motions generated at the tunnel control valve. It was thought pertinent to investigate whether these low frequency fluctuations were superimposed upon the working section and wing pressure spectra, and whether they were noticeable at the onset of buffetting.

The pitot-static probe was mounted from the ceiling of the 2-D insert with the face of the pitot in the plane of the wake survey. The centre of the pitot was located approximately 7.5 inches from the ceiling and 4.75 inches from the starboard sidewall of the insert.

A third differential pressure transducer was installed in the wing top surface at the 50 percent chord station to measure the local fluctuation pressure level. The tuning of this transducer module was accomplished as described above for the pitot/static probe.

The illustration on Figure 10 shows a side-view of the 2-D insert to display the relative dispositions of the rails on the ceiling and floor, the pitot/static probe and the wake rake.

3.0 The Models

The models were all of 10 percent thickness/chord ratio with span and chord dimensions of 15 inches. Each section employed a blunt nose and a suitable aft-camber with a 1.5 percent chord trailing-edge bluntness. The models were fabricated from heat-treated Armco stainless steel, with a nominal external finish of 16 micro-inches, and

consisted of a centre-section (20 percent to 70 percent chord station) a nose section, and a trailing-edge section - see Figure 2. The auxiliary air for the jet flap and slot blowing was introduced through the ends of the model and then ducted to the flap nozzle or blowing slot via a carefully designed set of turning vanes to provide a uniform jet discharge across the model span. The internal vanes extended within the wing plenum almost as far as the trailing-edge and structurally tied the upper and lower skins of the aerofoil together, preventing displacement of the nozzle walls when the high pressure air was introduced into the model. A rotary chopper valve was incorporated into the air supply line on each side of the wing, to provide (a) an on/off capability, to determine the response of the wing forces to the decay in the jet flap momentum; (b) a steady-state blowing supply with the valves positioned open; or (c) no air supply at all, with the valves closed. The control logic for the valves ensured that the two of them rotated in phase, to open or close-off the air supply.

The mass flux available with the slot flow or jet flap flow choked at exit from the wing, yielded values of C_μ up to 0.03 for use in the transonic Mach number range, at chord Reynolds numbers of 30 million.

The various model configurations described earlier in the Introduction are shown on Figure 1, and are obtained by changing the trailing-edge section. A photograph of some of the model components is shown on Figure 2.

The models were instrumented with seventy, 0.018 inch diameter static pressure orifices (forty on the upper surface) that were located approximately at mid-span. Two additional pneumatic lines led from a pitot in the jet blowing duct inside the wing, and from a wall pressure orifice within the wing plenum chamber, to permit the jet total pressure, p_D, to be measured. The stagnation temperature of the jet flow was also recorded by means of a calibrated diode sensor in the air supply line.

No artificial transition device was attached to any of the models, for at chord Reynolds numbers of 30 million, transition should occur close to the leading-edge. Operating at these high Reynolds numbers, however, dictates that the surface roughness of the models should be less than about 10 micro-inches, for the roughness around the leading-edge to be immersed in the laminar sub-layer of the viscous flow. The aforementioned surface roughness of 16 micro-inches implies that the model was not hydraulically smooth, and because of the inability to fill in smoothly the numerous countersunk screw holes, a measurable roughness friction drag must be expected in these tests as was found in the earlier tests.[1,7] On the other hand, the roughness around the leading-edge should assist the transition from the laminar to the turbulent boundary-layer state to be at a station close to the leading-edge, the position of which should be relatively uniform across the aerofoil span.

4.0 Detection of Buffet Onset

The technique employed to determine the onset of buffetting was the observance of the sudden divergence from the more-or-less predictable output of the rms balance normal force, N_{2N}, the primary measurement; supplemented by the rms static pressure fluctuations, p_w, measured at the 50 percent chord station by the tuned differential pressure transducer, that we discussed in Section 2.0. The force, N_{2N}, is that measured on the rear normal force flexure of the port sidewall balance. This output was chosen after the response of the wing-plus-balance to sinusoidal shaking had been determined.

At the onset of buffetting, the earlier tests[1,7] had shown that the shock wave on the upper wing surface was somewhere near to the 50 percent chord station, so that the position of the calibration loading was concentrated between the 40 and 70 percent chord stations at the centre of the wing. These loading positions were then probably representative of the location of the forcing function from the strong shock wave/boundary-layer interactions at buffet onset. (The position of the p_w differential pressure transducer was hence also suggested from the earlier tests.) On the calibration graphs, the output of N_{2N} was virtually flat from 10 to 300 Hz for the loading points considered, although a hint of amplification might be construed to occur around 100 to 130 Hz and at 180 Hz. A dominant frequency of 130 Hz was observed and reported in Reference 1, and this would appear consistent with the foregoing remarks.

The rms outputs from the N_{2N} flexure and the p_w pressure transducer were fed to separate channels of an oscillograph recorder, each channel demonstrating significant attenuation above 100 Hz. This recorder provided a rectilinear presentation of rms force and pressure outputs with respect to run duration, the step changes in incidence during a run being identified by means of a third pen trace between the N_{2N} and p_w charts. Figure 26 shows some representative examples of these charts. The angle of incidence at which the N_{2N} rms output suddenly increased in amplitude was taken to be the onset of buffetting; usually the divergence in the p_w rms output occurred at the same angle of incidence, although this was not always so. For purposes of reference, the divergence in rms amplitude was noted mostly at an angle of incidence slightly greater than that at which the maximum lift coefficient, C_{LMAX}, was measured, but as a conservative estimate for buffet onset on these aerofoils, α_w at C_{LMAX} is a satisfactory value.

We will note on Figure 26 that unsteadiness in the tunnel flow and in the wing boundary layer results in a measurable rms output even before the occurrence of buffet onset. At Mach 0.8, for example, at a cruise lift coefficient of 0.6 and at a chord Reynolds number of 30 million, the rms output in coefficient form, $\Delta C_{N\ N2N} \cong 0.002$ and the rms fluctuating pressure level on the wing was 1.0 percent of the mainstream dynamic pressure. These values on the wing would increase typically by a factor of 4 or 5 at buffet onset.[16]

It was seen in Reference 1, that at mainstream Mach numbers greater than 0.8, buffet onset as indicated by the divergence in trailing-edge pressure, led the onset as determined from the divergence in the rms output of N_{2N}. The physical explanation for the dissimilarity between the buffet loci, was associated with the presence of shock-induced boundary-layer separations on the lower surface of the aerofoil. These separations (and hence pressure divergence) commenced at low,

but off-design, values of incidence, to depress C_{pTE}. The undersurface separation was small in extent and frequently produced no measurable increase in output on N_{2N}. Consequently, the monitoring of the rms N_{2N} output was adjudged to be the more reliable indicator of buffet onset, in preference to the continuous recording of the trailing-edge pressure. The fluctuating force measurement would appear the correct choice; for flight measurements with supercritical wings have demonstrated the same differences between the two measurements, with the force measurement providing the proper indicator of wing buffet.

5.0 The Test Results

5.1 Force and Pressure Measurements

As we recollect, the primary objective of these investigations, was to obtain a measure of the relative effectiveness of geometric aft camber and externally supplied air in the jet flap or upper surface tangential blowing modes used separately or in combination, to increase the supercritical lift. In assessing the overal performance, we will comment upon the accompanying "drag due to lift" and pitching moment increments, as well as the buffet onset loci (C_{LBO} versus M_∞) for each configuration. Before proceeding further, however, it is necessary to consider two qualifying aspects of the tests, the chief of which is the effect of tunnel wall interference, and secondarily, the definition of the blowing momentum coefficient, C_μ.

We remember that the upper and lower walls of the wind tunnel test section were perforated with an open to total area ratio of 20.5 percent. Such a porosity has continued to be used, to reduce the contemplated wall interference correction, to primarily one of angle of attack. Subcritical experience would suggest that the partially open-jet character of the wall calculated with a porosity factor P = 1.2,[10] produces only a very small correction to the mainstream Mach number, M_∞, and virtually no correction due to the effects of streamline curvature. Thus, in such circumstances, the influence of the wall interference would not hinder directly the performance assessment of the various configurations insofar as lift and pitching moment were concerned: but, ignorance of the true or correct angle of incidence would preclude the determination of the absolute value of drag from the sidewall balance measurements, which provide normal and axial forces with respect to the wing chord line.

For the drag levels, we must rely on the measurement of profile drag from the wake surveys, with the attendant difficulties of spanwise non-uniformities and the corrections to be included for the jet flap momentum added from outside the tunnel, coupled with changes in local static pressure across the plane of the wake traverse. Subcritical correction techniques, such as those of References 9 and 10, were assumed to be questionable, because it was not proven that subsonic flow conditions did exist at the walls, at the high Mach numbers of the tests; nor was it proven that identical porosity factors attributed to the ceiling and floor in the subcritical theory, were necessarily correct.

As a result there has been a continuing effort to evolve at least a viable approximate correction for the wall interference[1,7,16] in which an incidence correction was obtained on the assumption that the mainstream Mach number was not affected by the wall interference. The procedure outlined there was suggested on a tentative basis, and is in need of further corroborating evidence to justify its use. For this purpose, and to obtain further insight into the wall interference in the above tests, the wall pressures on both the tunnel ceiling and floor were gathered for each test incidence of the wing. The wall pressures were then used in the time dependent, finite difference calculation procedure of Magnus and Yoshihara[12] to obtain an independent assessment of the incidence (and blockage) corrections. Though the single example to be presented is intended as a spot-check of the above postulated correction method, the finite difference procedure, in principle, can be utilised to evolve a less tentative wall interference correction. Thirdly, a revised subcritical flow calculation procedure[11] will be discussed in which the measured wall pressures are used to infer different porosity factors for the ceiling and floor of the wind tunnel, and the computed corrections are in turn compared with the previous two techniques.

The second qualifying remark relates to the definition of the momentum parameter characterising the jet flap or tangential slot blowing. In the case of the jet flap, it is customary to define a jet momentum coefficient

$$C_\mu = \frac{\dot{m}_j u_j}{q_\infty S'}$$

where $\dot{m}_j$ is the mass flow rate, q_∞ is the mainstream dynamic pressure, S' a relevant area (in this case, the wing area equivalent to the span of the jet slot), and u_j, a fictitious velocity calculated on the assumption of an isentropic expansion from the jet flap stagnation conditions to the test section static pressure. Such an arbitrary definition for u_j would not appear to be relevant in characterising the jet flap flow in the vicinity of the nozzle exit where the flap air mixes with the local ambient stream. In particular, the above definition in no way accounts for the degree of under-expansion of the jet (pluming) as it emerges from the nozzle nor for any shock losses in the local supersonic region in the jet adjacent to the jet flap slot. Clearly, one might use the lower local sonic velocity, a_j^*, corresponding with the temperature of the jet flow, but this would be as arbitrary as the previous definition.

The appropriate characterisation of the jet in the slot blowing case is as important, since the degree of jet expansion as it emerges from the nozzle, can affect the mixing between it and the boundary layer to be re-energised. In Reference 5, for example, and in earlier work referenced therein, the jet momentum was specified as the excess momentum available at the jet exit

$$m_j (u_j - u_1)$$

(where u_1 was the local mainstream value at the boundary-layer edge). The definitions are virtually the same except for sign:

$$\text{momentum deficiency} = \rho u_1^2 \theta = \int \rho u (u_1 - u) dy = \int (u_1 - u) dm.$$

This is a convenient and rational method of

representing the injection fluid, where u_j can be measured at the jet exit. Unfortunately, the latter measurement was not available in the aerofoil tests, and so the same definition of C_μ was used for both the slot blowing and the jet flap tests.

At a given mainstream condition, with only one nozzle configuration, the problem of the appropriate representation of the blowing does not arise, provided a consistent definition of C_μ, for example as given conventionally, is used. We see that the value of C_μ serves only to identify the magnitude of the blowing. If, on the other hand, a jet flap or slot blowing experiment is carried out using different sized sonic nozzles, a simple matching of the C_μ as stipulated above, even with identical tunnel conditions, would perhaps be insufficient to yield identical blowing effects.

With the foregoing comments in mind, let us proceed to the test results. On Figures 14 to 16, we show the forces and moments for the various configurations at nominal M_∞ values of 0.75, 0.80 and 0.85. Here, the pitching moment coefficients at one-quarter chord and the lift coefficients are obtained from the sidewall balance measurements while the recorded aerofoil profile drag coefficient, C_{DWC}*, that has been suitably corrected for the momentum addition from outside of the tunnel, see Equation 6.6, is computed from a spanwise integration of the wake survey results at the three pitot probes. The abscissae of the lift/drag polars are plotted as $[C_{DWC}+C_\mu]$, in order to place the non-blowing and blowing cases on an equal footing. The profile drag coefficient at a given spanwise station, is calculated according to the method advocated in Reference 17, in which the actual conditions measured in the wake, one chord length downstream of the aerofoil trailing-edge, are related to conditions in a substitute plane downstream of the model, where the mainstream has returned to p_∞, q_∞ and M_∞. (In the tunnel, with the model chord to tunnel height ratios of 0.25 that we are using, and operating at high C_L values, the static pressure measurements near the walls show that the flow in the tunnel never does, in fact, relax to "infinity" conditions before discharging into the diffuser.) We reiterate then, that the local static pressure in the wake at the traversing station does not equal p_∞, but the inclusion of the former instead of p_∞ in the equation for C_{DW} only reduces C_{DW} by about one percent. Notwithstanding, there is a substantial linear static pressure gradient across the stroke height of the wake rake, the pressure increasing in the direction from the ceiling to the floor, see Figures 17.1 and 17.2. The linearity is perturbed upon traversing through the viscous wake itself. The pressure gradient across the tunnel follows from the significant inflow along the ceiling that is induced by the high suctions of the upper surface pressure field of the wing, which causes, in turn, a substantial curving downflow in the wind tunnel aft of the model. As the injected momentum rate from the aerofoil increases, so does the pressure gradient across the tunnel. Such linear pressure gradients, however, only influence the wake profile drag measurements insofar as they change the local static pressure in the wake flow itself.

*$C_{DWC} \equiv C_{DW} - C_\mu \frac{u_\infty}{u_j}$

In assessing the force data, let us keep in view that our overall objective is the generation of as large a buffet-free lift coefficient as possible, with the smallest drag. For the maximum buffet-free C_L, we may conservatively take the maximum lift coefficient, C_{LMAX}, since an examination of the rms fluctuating output from the N_{2N} balance flexure, indicated buffet onset to occur at an angle of incidence no smaller than that for C_{LMAX}.

Consider first of all, the lift/drag polars exhibited on Figures 14, 15 and 16. We indicate here the configurations forming the $(L/D)_{MAX}$ envelope. The general appearance of the polars departs from the usual shape obtained for more conventional aerofoils, due to the consequences of the high degrees of aft cambering that require the use of negative angles of incidence to achieve moderate to low values of the lift coefficient. We should perhaps focus our attention, therefore, not on the off-design settings of the aerofoils, but on C_L values of 0.6 and above. A comparison of the polars at the three Mach numbers illustrates that a convenient progression in flap change is needed at each Mach number to progress along the $(L/D)_{MAX}$ envelope. Beginning at the lower lifts, Aerofoil I with the 10-degrees of aft camber and no blowing provides the least drag at all Mach numbers. Above C_L values of about 0.8, the optimum L/D polar is, however, sensitive to which change of geometry is activated. For instance, at Mach numbers up to 0.8, the jet flap issuing from Aerofoil I, shows to be of benefit at C_L values close to unity; but at $M_\infty \cong 0.85$, deflection of the aft camber line to 20-degrees on Aerofoil II, coupled with a small C_μ of 0.006 for boundary-layer control, provides the best performance. For the production of higher lifts approaching the level of C_{LMAX} of configuration II, see Figures 15.1 and 16.1, the slot blowing aerofoil IIS takes over with increasing C_μ necessary, until the train of configuration changes is completed by enlisting the assistance of the jet flap, on configuration IISJ. The superior performance of IISJ, achieving a maximum lift coefficient of 1.58 at $M_\infty \cong 0.85$ shows substantial promise. We note further, that at $M_\infty \cong 0.85$ especially, all of the blown configurations are relatively competitive at C_L values near 1.2. At $M_\infty \cong 0.75$, on the other hand, the jet flapped aerofoil IIJ, indicates an advantageous performance over the slot blowing configuration, IIS. On the latter configuration, the terminal shock wave on the upper surface would appear to be too far upstream for the slot blowing to have its maximum beneficial effect, except near the C_{LMAX} of 1.4. Aerofoil IIJ produces a substantial C_{LMAX} of 1.6, and Figure 14.1 demonstrates its superiority.

We should comment in passing, that an earlier preliminary assessment of results in Reference 18, where uncorrected balance drags were used - that is, the balance normal and axial forces were resolved with respect to the wind tunnel axis - led to a somewhat different overview of the relative merits of the various aerofoils. In summary, at the higher Mach numbers of 0.8 and 0.85, and high lifts, the use of an increasing degree of aft camber, coupled subsequently with slot blowing, and then, finally, in conjunction with the jet flap, provide the optimum lift/drag performance of the aerofoils

under consideration. At the highest Mach number of 0.85, it was surprising that the increase of C_{LMAX} in the case of Aerofoil IISJ with $C_\mu \cong 0.02$, relative to the base Aerofoil I with $C_\mu = 0$, was as large as $\Delta C_{LMAX} = 0.6$.

An examination of the pitching moment coefficients about the one-quarter chord station, indicates a near invariance with C_L at $M_\infty \cong 0.75$, but there is a shift to greater negative values as the aft camber effects are increased. At Mach 0.8, the invariance of C_M with C_L remains below C_L values of unity; but above, there is a substantial increase in the nose-down moment where slot blowing and the jet flap are employed together (IISJ). Finally, at $M_\infty \cong 0.85$, we note larger changes in C_M at the low off-design C_L values, than those observed at the lower Mach numbers.

To investigate the manner in which the lift augmentation (and drag augmentation!) was generated, let us next examine some comparisons of representative pressure distributions. In Figure 18, we first compare the pressure distributions for Aerofoils I and IJ at $M_\infty \cong 0.8$ and at the same corrected angles of attack $\cong 0.9$ degree, for respective C_μ values of 0 and 0.02. The lift augmentation here is indicated by the shaded area, and exhibits the familiar pattern discussed earlier. (In the comparison, the corrected incidence obtained from the streamwise momentum method is quoted here.) We note that the two configurations are at roughly the same corrected incidence, with the jet flap, although producing an increase in lift of $\Delta C_L \cong 0.52$, decreasing the lift/drag ratio from about 35 to 26.

On Figure 19, we show the effect of the increased aft camber in the comparison of the pressure distributions for Aerofoils I and II at $M_\infty \cong 0.80$, $C_\mu = 0$ and at $\alpha_c \cong 1$ degree. Here, the expected aft camber lift augmentation pattern is seen in a moderately extreme form. In the case of Aerofoil II, we see a significant strengthening of the upper surface shock wave that has now produced a confined separation bubble. Because of the high Reynolds number, separation towards the trailing-edge appears to be confined downstream of the 90 percent chord station. In comparison with Figure 18, we observe the distinct advantage in using the jet flap at these lift coefficients rather than deflection of the aft camber line alone.

Figure 20 shows the distributions for Aerofoil II at $M_\infty \cong 0.85$ and $\alpha_c \cong 3$ degrees, with first of all only slot blowing added, and then slot blowing in conjunction with the jet flap. At this condition, Aerofoil II ($C_\mu = 0$) is about at C_{LMAX} (see Figure 16.1) and at or on the verge of buffet onset with the shock-induced separated flow extending beyond the trailing-edge. The overall effect of the slot blowing alone at $C_\mu \cong 0.01$ is particularly beneficial here, for it increases the effective aft camber, as evidenced by the increased plateau loading and the rearward displacement of the upper surface shock wave by almost 30 percent of the wing chord. In spite of a local separation bubble downstream of the jet slot position at $x/c = 0.80$, the flow almost recovers to a positive pressure coefficient at the trailing-edge. The addition of the jet flap with $C_\mu \cong 0.01$ in combination with slot blowing at the same C_μ value, now improves the entire chordwise loading over the lower surface, as well as providing some increased suction on the aft upper surface. The position of the upper surface shock wave does not appear to change, however. We see that, even at this high M_∞ of 0.85, the combined slot blowing and jet flap flows have provided a significant lift augmentation of $\Delta C_L \cong 0.38$ (see Figure 20), with no significant loss in C_L/C_D ratio.

Let us take a cut across Figure 15.1 at a constant lift coefficient of $C_L \cong 1.2$, at $M_\infty \cong 0.8$. It so happens that at this C_L, we have available pressure distributions the integrations of which from four configurations (at various angles of attack) all provide the same C_L. It is instructive to view how the lift is generated over the chord, and what levels of drag result. Figure 21, in fact, displays these four pressure distributions from Aerofoils II, IIS, IJ and IF2J, the latter three pumping air with $C_\mu \cong 0.02$. Let us observe the tabular format at the heading of Figure 21. As already shown on Figure 15.1, we see the clear superiority of the jet flap configuration IJ, at this lift coefficient. Aerofoil IJ at a corrected incidence of 0°, has the highest lift/drag ratio, and the lowest component of axial force acting parallel to the chordline. It is perhaps somewhat surprising at first glance that in spite of the different angle of attack settings of the four aerofoils that the pressure distributions over 90 percent of the undersurface virtually overplot, even though the "solid and pneumatic" aft-camber geometry is substantially changed in each configuration. Clearly the predominant differences are reflected in the upper surface pressure distributions. As angle of attack increases, the acceleration of the flow increases around the nose to produce higher suction plateau pressure levels. Aerofoil IF2J produces the most uniform pressure distribution with the terminal upper surface shock wave near $x/c \cong 0.90$, but yields a lower suction plateau pressure level. The remaining configurations demonstrate a trade-off between increasing lift developing over the initial 70 percent chord at the expense of the normal shock moving upstream as incidence increases. Aerofoil IIS is a special case, however, for the slot blowing is too far downstream of the shock boundary-layer interaction region, and the jet expands to a high supersonic Mach number before "shocking-out" in turn at $x/c \cong 0.9$. But in so doing a large region of suction pressure is developed.

Aside from the above experiments designed to assess the relative performance of changing the aft camber by solid or pneumatic means, further tests were conducted at $M_\infty \cong 0.8$ to obtain the effect of varying the angle of the jet flap efflux with respect to the wing chord-line on Aerofoil IJ; and to obtain the effect of varying the blowing coefficient, C_μ, on Aerofoils IF2J and IIS. Figure 22 demonstrates the increasing usefulness of rotating the jet efflux downwards as lift is increasing, to obtain the optimum lift/drag polar. We note that up to C_L's of about unity, a 30 degree jet angle is most advantageous, while between $C_L \cong 1.0$ and 1.3, rotation to 85 degrees provides significant improvement on C_{LMAX}. Finally above $C_L \cong 1.3$, ejecting the jet flap air against the direction of the freestream at $\theta_j = 120$ degrees, yields the maximum performance of Aerofoil IJ.

In Figure 23, we show the lift coefficients for Aerofoil IF2J, plotted first of all, against the geometric angle of attack α_w, on Figure 23.1; against drag coefficient on Figure 23.2 and against

pitching moment coefficient on Figure 23.3, for various blowing rates up to $C_\mu \cong 0.03$ at $M_\infty \cong 0.8$. Similar, and corresponding force coefficients for Aerofoil IIS are displayed on Figures 24.1, 24.2 and 24.3.

In the case of Aerofoil IF2J, the breaks in the lift curve slope (for example, at $\alpha_w \cong 2$ degrees where $C_\mu \cong 0.02$) are primarily due to the reversal of the downstream movement of the upper surface shock wave, but there appears to be no loss here in the generation of high suction pressure levels ("peakiness") around the nose. For a given α_w, the rate of change of the lift augmentation ΔC_L with C_μ is relatively uniform above C_μ of 0.01, at a value about one-half of the initial slope. In the case of Aerofoil IIS the breaks in the lift curve slope of Figure 24.1 are again due to the reversal in rearward movement of the upper surface shock wave with increase of incidence. Here a given slot blowing momentum appears less and less adequate to maintain the aft camber as α_w increases; for shock-induced separation becomes worsened with the increasing shock pressure ratio. Whereas the jet flap provides a lift increment at all incidences (Figure 23.1) by providing a 'supercirculation' effect, the mechanism of the slot blowing, on the other hand, is one of delaying boundary-layer separation, for up to unit values of C_L, C_μ has insignificant effect on the dispositions of the lift curve slopes (Figure 24.1).

On the basis of the drag coefficient that we have elected to use throughout - we remember the wake profile drag is first of all corrected for the momentum added from outside the tunnel stream and then C_μ is added to C_{DWC} to provide some (conservative) measure of the penalty for supplying C_μ - we see from Figures 23.2 and 24.2 that the blowing does not provide an optimum lift/drag polar for configurations IF2J or IIS until C_L exceeds 1.1. There is no obvious winner between these two configurations. The true benefit of blowing is clearly to enhance C_{LMAX}. It is not economic around design cruise lift values.

The increasing nose-down pitching moments generated about the section one-quarter chord position, Figures 23.3 and 24.3, as C_μ is increased, would presumably be detrimental because of additional drag that would arise in the eventual trimming of these moments on a three-dimensional configuration. The slot blowing configuration, IIS, is to be preferred.

In Reference 16, a complete compilation of the results from all of the configurations tested, is available. We emphasize that only some of the salient features found during the tests are presented in this review.

5.2 Lift and Drag at Buffet Onset

In the reading of the results so far, we should remember that the configurations tested were intended to be representative of desirable supercritical aerofoil designs, but by no means should they be considered as optimum geometries. Thus, for example, the location of the upper surface slot blowing was selected at 80 percent chord, and this proved suitable for controlling the shock/boundary-layer interaction at $M_\infty \cong 0.85$, but was not judiciously placed for lower test Mach numbers around 0.7, where the upper surface shock wave was usually situated ahead of the slot. Even in the latter cases, however, there was beneficial re-energisation of the top surface boundary-layer.

Let us now consider the relative performance of the configurations with respect to the buffet onset loci that are shown on Figure 25. We recollect that the lift coefficient, C_{LBO}, at the onset of buffetting, was determined from studying oscillograph records of the angle of incidence at which the divergence occurred in rms fluctuating normal force measurements (called N_{2N}) from the rear flexure of one sidewall balance - and supplemented by rms surface pressure measurements (p_w) at the 50 percent upper surface wing chord station. Figure 26 displays typical traces from the N_{2N} and p_w measurements for Aerofoils I and II at $M_\infty \cong 0.8$. The response of the recorder is virtually flat at frequencies from 100 Hz down to 50 Hz, but begins to roll-off at frequencies less than this value. A quick inspection of the charts indicates a good correlation between the incidence at which the divergences in pressure and force signals occur. We see also, that on the results from Aerofoils I and II, buffetting occurs at large negative angles of attack due to undersurface shock/boundary-layer interactions and separations. We further observe that the introduction of the slot blowing air produces a substantial increase in the fluctuation force level at the cruise incidences of Aerofoil II, prior to the onset of buffetting; while, as we might expect, the amplitude of the rms fluctuations past buffet onset is generally suppressed by the blowing. Since the onset of buffetting occurs approximately at the same geometric angle of incidence for $C_\mu = 0$ and $C_\mu > 0$, the effect of the pneumatic additive is clearly analogous to deflecting the aft camber line (that is, drooping a trailing-edge flap).

Although no data were obtained at $M_\infty = 0.75$, plausible extrapolation of the buffet onset locus on Figure 25 for Aerofoil IISJ, would indicate that this configuration with combined slot blowing and jet flap, would have the highest overall buffet onset locus. At the lower Mach numbers, it is clear that Aerofoil IIJ with a jet flap (tested previously - see References 1 and 7) has good performance, which, however, diminishes as the shock strength on the upper surface increases with increasing M_∞. We see at $M_\infty = 0.8$ and above, that improved buffet onset performance is obtained with slot blowing, IIS, rather than with the jet flap alone. The loci for the jet flap configurations all tend to drop substantially towards $M_\infty \cong 0.85$ where slot blowing is not employed. Such a decrease is due to the rapid loss of upper surface suctions caused by shock-induced separations that remain unsuppressed without slot blowing boundary-layer control.

Thus, if we consider Aerofoil I (C_μ=0) as the reference aerofoil, at $M_\infty = 0.75$ we see that IIJ with $C_\mu \cong 0.015$ has produced an increase in C_{LBO} of 0.56 (IF2J is only slightly inferior with $\Delta C_{LBO} \cong 0.50$); whilst at $M_\infty = 0.80$ and 0.85, Aerofoil IISJ ($C_\mu \cong 0.02$ total) has produced respective increases of $\Delta C_{LBO} = 0.51$ and 0.56. These augmentations, particularly the latter, must be considered as substantial especially since the base aerofoil itself is a high manoeuvre performance aerofoil, and the lift augmentations in the transonic régime are difficult to achieve due to the ease with which

weak shock waves can be converted into those that cause buffetting. Before leaving Figure 25, let us remark on one surprising result. The rotation of the jet flap efflux from $\theta_j = 85$ degrees to 120 degrees (see Figure 3.2) produces a surprising and useful increase in buffet onset performance with and without the jet flap. The small spoiler introduced by the geometry change to 120 degrees shown on Figure 3.2 clearly causes a gross change in the aerofoil pressure distribution. At $M_\infty \cong 0.8$, for instance, the ΔC_{LBO} produced for $C_\mu = 0$ and $C_\mu > 0$ is about 0.1, when measured against the $\theta_j = 85°$ results.

To assess the resulting drag polars let us return to Figures 14.1, 15.1 and 16.1. Here we have shown in the C_L, C_D plots the configurations that would form the best C_L/C_D envelope. Although we have demonstrated that the maximum lift values at buffet onset are given, for example, by Aerofoil IISJ at Mach 0.8 and above, this is accomplished at the expense of generating considerable absolute drag. The lift/drag ratio at buffet onset for this Aerofoil falls from about 19 at $M_\infty \cong 0.8$ to about 11 at $M_\infty \cong 0.85$. On the other hand, we note on Figures 14-16 that at a given large C_L, the use of powered lift can lead to substantial reductions in drag relative to the base Aerofoil I configuration. Thus at $M_\infty \cong 0.8$, the use of the jet flap with $C_\mu \cong 0.02$ has produced a drag reduction of 430 drag counts at the buffet onset lift coefficient of $C_L = 1.08$, and a reduction of 360 drag counts at $C_L = 0.91$ at $M_\infty \cong 0.85$.

Finally, in the discussion of the buffet onset results, we should like to show fluctuation static and pitot rms pressure measurements made with the pitot/static probe described in Section 2.0 and with Aerofoil I in the wind tunnel at $M_\infty \cong 0.8$ and $R_c \cong 30$ million. The fluctuation measurements were recorded on FM tape and reviewed after the run. The previously described balance (N_{2N}) and wing surface pressure (p_w) fluctuations were also recorded on to the tape simultaneously with the probe measurements. Figures 27.1 and 27.2 present the broadband (unfiltered) and narrowband (filtered 1/3 octave centre frequency) spectra versus run duration, each column of results representing one channel of data.

Across the top line of Figure 27.1, we see the columns of results for the pitot, static, wing pressures and N_{2N} balance forces in turn. We remember that the pitot/static probe was located in the plane of the wake survey above the tunnel centre-line, (see Section 2.0). The deciBel charts in the first row are the overall or broadband outputs from the four channels. The dB level is evaluated with respect to a pressure of 0.0002 dynes/sq.cm. We note on the top left hand chart that the geometric incidence of the wing, α_w, changes from a cruise incidence of 1.24 degrees to one of 6.01 degrees at buffet onset about one-quarter way through the run at which time all of the broadband outputs increase significantly. That is, the effects of buffetting on the wing are transmitted into the tunnel mainstream (at least downstream of the aerofoil) to increase the mainstream fluctuation levels by as much as 5 dB. The short table on Figure 27.1 displays the fluctuation levels in quantitative terms, and we note that as a percentage of mainstream dynamic pressure, the probe, $\Delta p_{rms}/q_\infty \cong 1.2$ percent at buffet onset. We see also that the fluctuations are virtually isotropic in character for the probe pitot and static pressure outputs correlate in absolute level. The rms fluctuation pressure level on the wing at cruise lift coefficient is about 3 dB more than the significant amplitude of 156 dB in the mainstream. In contrast, at the onset of buffetting, the wing measurement is approximately 12 dB higher than the (elevated) mainstream level.

If we now return to peruse the broadband and narrowband outputs with the wing at buffet onset, they do not appear to show any step function changes in output at the time the tunnel control valve unchokes. Such time is usually about half way through the run at this Reynolds number. The broadband outputs from the wing sensors are relatively uniform throughout the duration of measurement at buffet onset, although we perhaps can discern some changes in output at the low 1/3 octave centre-frequencies, corresponding with the valve unchoking. Additional tests made at lower Reynolds numbers demonstrate the rms pressure fluctuation amplitudes to scale with the mainstream dynamic pressures, and to yield the same percentage fluctuation levels.

5.3 The Jet Flap in an On/Off Mode

We shall conclude Section 5 by presenting some additional test results in which the response times were investigated for the decay in jet flap effectiveness, for such information is relevant if the jet flap is to be used as a direct lift or lateral control device. The volume of the feed-air pipes to the wing precluded the testing for response in an off/on mode, due to the long lag times in establishing a constant jet flap flow (and which was always set prior to the commencement of the tunnel wind-on phase).

The on/off tests were carried out for Aerofoil I at $\alpha_w = 3°$ at $M_\infty \cong 0.76$, 0.8 and 0.85, with a starting $C_\mu = 0.021$. The Reynolds number was 30 million based on the wing chord and tunnel mainstream flow conditions. Only the instantaneous forces and moments were recorded, and since the qualitative features of the results were the same at all Mach numbers, we shall show only those obtained at $M_\infty \cong 0.76$. In interpreting the results, it is necessary to be familiar with the jet flap air supply system. The air is supplied from the discharge of the main tunnel compressor at 320 psia, and is then ducted through a 6-inch diameter pipe and through a flow meter and a pressure control valve. The air subsequently enters the model from both sides via 1-inch diameter pipes. Just outside of the test section, co-ordinated rotating cylinder chopper valves were installed, to operate the jet flap not only in a steady state mode, but also in a step function mode. During the check-out of the valves, contaminants in the air supply caused the valves to seize, necessitating a reduction in the radius of the cylinder. As a result, the chopper valves could pass a small leakage flow.

In Figure 28, we show the results for the on/off tests for $M_\infty \cong 0.76$, with the time histories for C_μ and the balance outputs illustrated on the left. Upon closing of the chopper valves, the volume of the air within the wing exhausts into the tunnel flow in about 50 millisecs, with the decay of the balance forces and moments virtually following the decay in C_μ. On the right hand side of the

figure, we show the pressure distributions (but at a somewhat lower angle of attack) representing the initial and final steady states of the on/off mode. The shaded area is particularly significant, since it represents the additional lift provided by the jet flap. As the jet flap is turned off, the immediate effect is a rapid drop in the trailing-edge pressure on the lower surface and a rapid increase in the trailing-edge pressure on the upper surface, resulting soon after in a sudden loss of aft loading. This accounts for the change in pitching moment to a smaller negative value. Somewhat later as these effects propagate upstream on the upper surface to the downstream side of the shock wave, an upstream movement of the shock wave now occurs to accommodate the unsteady jump conditions across the shock wave. The slowest adjustment is in the level of the upper surface plateau pressures upstream of the shock wave. Here, since the most direct route is "blocked" by the upper surface supersonic region, the jet flap decay effect must propagate along the lower surface from the trailing-edge to the nose, and then over the nose to the upper surface. If we take the representative propagation speed as the speed of sound minus the mainstream velocity, at $M_\infty \cong 0.76$, it would require about 5 millisecs to travel the 15-inch chord length, an order of magnitude less than the drop time for C_μ. A quasi-steady assumption here would therefore not be unreasonable.

There is, however, a further undesirable, but interesting, complication. As the lift is decreased by turning off the jet flap, the wall interference diminishes resulting in an increase in the effective angle of attack. In the quasi-steady case, for example, at $M_\infty \cong 0.76$, the effective incidence, α_c, would change upwards by about 0.6° as the jet flap is turned off. Though the propagation length of this effect is larger (model to the wall and return), the propagation speed is higher in the tranverse direction, so that the adjustment times for the wall effect would still be of the same order as that required for the surface pressures to adjust directly to the jet flap effect.

Therefore, in the practical application of the jet flap effect in a control mode, as might have been anticipated, it is not the aerodynamic response times, but the mechanical response time characteristic of the air supply, that would most probably dictate the control effectiveness.

6.0 Wind Tunnel Wall Interference

We know that wind tunnels never actually represent the unconfined, free air conditions around an aircraft or missile, that are encountered in flight. In the transonic flow régime, in particular, many variations on the theme of slotted and porous walls for wind tunnels have been used to reduce to a minimum the chance of reflecting shock waves back on to the models. But even with these ventilated walls, the essential problem of the effects of the boundary constraint upon the flow field surrounding the model, still remains, and these effects are significant unless the model is very small compared with the wind tunnel dimensions. Moreover, if the constraint applied by the walls, results in substantial perturbation velocities other than those producing a uniform change of angle of attack, it is doubtful whether the constraint effects can indeed be estimated adequately. Certainly, at the higher subsonic Mach numbers (typically $M_\infty \geq 0.8$), where to obtain the highest test Reynolds number, we use a model with relatively large dimensions compared with those of the ventilated wind tunnel, wall effects have not lent themselves to accurate estimation, and these effects on the measured aerodynamic parameters cannot be legitimately accounted for by linearised flow correction procedures.

In principle then, we have as our ultimate goal in wind-tunnel testing, the desire to produce the same flow field around the model in the wind tunnel that will be met in flight. The proposal of the "Self Correcting Wind Tunnel" by Sears[19], is one design of facility so arranged that by applying different rates of suction control at given stations along the perforated walls of the test section, the free-air conditions adjacent to the model are caused to be set up. But, as of now, we are committed to testing in existing wind tunnel facilities without such sophistication, where the effects of the given boundary constraints must be assessed to provide a true test Mach number and model angle of attack.

How then, have we chosen to approximate the two-dimensional, infinite stream condition about the model, after obtaining the wind tunnel measurements? We have elected to attempt this by three methods. First of all, we assume that the 20.5 percent porosity of the tunnel ceiling and floor is sufficiently "open" that there is negligible correction to the stream conditions due to model blockage. Then, taking due account of the streamwise momentum deficit through the floor and ceiling, (the tunnel plenum is open to diffuser suction), a streamwise momentum balance[8] enables one to estimate the correction to model angle of attack.

Secondly, a subcritical calculation approach is tried, wherein the effects of unequal porosity factors, ascribed to the floor and ceiling, are investigated with a mathematical model, that utilises a point-vortex and a point-doublet placed mid-way between the two walls. Closed form solutions are derived, using the method of images, for wall pressure distributions, and corrections to Mach number and model angle of attack. The predicted wall pressure distributions are compared with the experimental results, and agreement is shown to be markedly better than is possible with the use of equal porosity factors; the reasonable agreement continuing up to tunnel mainstream Mach numbers of about 0.8. (Prior to the approach, we should remember that a constant wall porosity factor was used for both walls, and derived in an often unconvincing manner!)

In a third technique, the measured wall pressures are used in the finite difference transonic flow calculation method of Magnus and Yoshihara[12], to obtain a spot check on the incidence and Mach number correction at a mainstream Mach number of approximately 0.8.

The philosophies of the three approaches are enlarged upon below, and a comparison of the results, where appropriate, is made in the following paragraphs.

6.1 Streamwise Momentum Analysis

The basis of the wall interference correction

procedure by the streamwise momentum analysis, is that the open area of the tunnel ceiling and floor is considered sufficiently great that the effect of the walls is simply one to adjust the model angle of attack; and that no correction need be made to the value of M_∞. The implication is that neither the wing pressure distribution nor the wing skin friction distribution are affected by the walls, so that the profile drag of the aerofoil is given by surveying the viscous wake downstream of the trailing-edge. We, further, neglect any displacement effects of the wake. At the time of initially formulating the method, we realised that this was, perhaps, a too simple-minded approach, but the alternative linearised methods clearly depended upon their implicit restriction, that the flow at the walls must be subsonic. When extensive regions of supercritical flow exist around an aerofoil model, we may legitimately enquire whether subcritical flow conditions do in fact exist at the tunnel walls, at high lift coefficients, and with aerofoil chord to tunnel height ratios, c/H, as large as 0.25 (as in the present tests). For we have seen that calculations in inviscid flow[21], have shown that at $M_\infty = 0.85$ and $\alpha = 2$ degrees, the lateral extent of the supersonic region on the top surface of Aerofoil I, extends in free-air past the position of the tunnel ceiling. Clearly, if subcritical conditions do not exist at the walls, then in principle, there is no basis whatever for applying subcritical flow theory. These were some of the thoughts, then, behind the devising of a correction technique, free of the restrictions of linearisation procedures, prior to the availability of the wall static pressure measurements.

Let us look at a rectangular control surface within the confines of the wind tunnel walls, CDEF, and unmolested by the wall boundary-layers. CD and FE are assumed to be cuts normal to the stream where mainstream conditions exist upstream and downstream of the aerofoil. BA is taken to be a plane in which a wake survey is accomplished, say between the points B' and A', about one chord length downstream of the aerofoil. For generality,

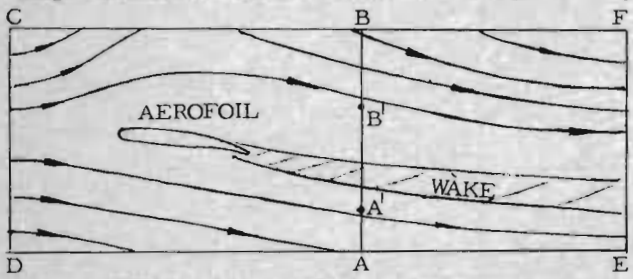

let us consider the aerofoil to be operating with a jet flap, where the blowing source is separate and distinct from the tunnel mainstream.

We know (subsequently!) from the measurements of static pressure adjacent to the wind tunnel walls and in the plane of the wake survey that:

(1) the static pressure in the wind tunnel never actually returns to p_∞ downstream of the model, so that in our diagram, FE is, in fact, a fictitious plane.

(2) there is a small outflow from the tunnel to the plenum surrounding the test section, just ahead of the wing, followed by a substantial inflow from the plenum to the tunnel, along the remainder of the tunnel ceiling. A loss of momentum will occur each time the stream crosses the wall, due to the effects of viscosity in the normal holes of the perforated wall.

(3) an outflow from the tunnel to the plenum exists all along the floor.

(4) the local static pressure in the plane of the wake survey is not equal to p_∞ and is not a constant, (see Figures 17.1 and 17.2). A significant, but linear static pressure gradient was measured across the stroke height of the wake rake, the pressure increasing in the direction from the ceiling to the floor. The linearity is perturbed upon traversing through the viscous wake itself. The pressure gradient across the tunnel follows from the significant inflow along the ceiling that is induced by the high suctions of the upper surface pressure field of the model, which causes, in turn, a significant curving down-flow in the wind tunnel, aft of the model.

If mass and streamwise momentum are to be conserved in a steady flow, within contour DEFC, then the combination of the continuity equation and streamwise momentum equations results in:[8]

$$(C_{NB}\sin\alpha_w + C_{XB}\cos\alpha_w)q_\infty S = \int_{SPAN}\left\{\int_E^F (p_\infty - p)dy\right. \qquad \text{(I)}$$

$$\left. + \int_E^F \rho u(u_\infty - u)dy - \dot{m}_j u_\infty + \int_D^E \rho u'v dx - \int_F^C \rho u'v dx\right\} dz \quad 6.1$$

(II) (III) (IV)

The force coefficients on the left-hand side of Equation 6.1, C_{NB} and C_{XB}, relate to the normal and axial forces determined by the sidewall balances, while α_w is the geometric angle of attack measured with respect to the tunnel axis. On the opposite side of the equation, m_j is the jet flap mass flow rate per unit span of the aerofoil, whose stagnation temperature is the same as that for the mainstream. The terms $u = u_\infty + u'$, and v, are the component velocities parallel and normal respectively to the tunnel axis.

The form drag and skin friction forces on the aerofoil are together manifested finally by a loss of momentum in the wake. The term labelled (I) above clearly disappears since $p \equiv p_\infty$ everywhere along FE. The term (II) is the required profile drag of the aerofoil, that we must relate to the actual measurements in the plane of the wake survey. The third term is required to "correct" the profile drag for the foreign but additional momentum added from outside the confines of the momentum contour (a source term in effect), while in term (IV), we see the net effect of streamwise momentum flux across the tunnel ceiling and floor, which may be either large or small, depending upon the cross-flow velocities.

Now, in Reference 17, the flow parameters at a plane corresponding with BA are related to the terms in the plane EF, by assuming that the total energy is constant everywhere in the flow, and that mean streamlines may be drawn in the wake along which the total pressure may be assumed to be

constant between the planes BA and FE. The first assumption implies that the stagnation temperature should be constant everywhere, while the second is equivalent to assuming that the entropy is constant along each streamline.

Writing the profile drag,

$$D = \int_E^F \rho u(u_\infty - u)dy \ , \qquad 6.2$$

then, in coefficient form,

$$C_{DW} = \frac{1}{q_\infty S} \int_{SPAN} \int_E^F C_D' dy \qquad 6.3$$

Making the aforementioned assumptions, we find that in terms of the ACTUAL conditions measured in the plane AB, C_D' becomes:

$$C_D' = 2\left(\frac{p_{TW}}{p_0}\right)^{.286}\left(\frac{p_{SW}}{p_\infty}\right)^{.715}\left\{\frac{1-\left(\frac{p_{SW}}{p_{TW}}\right)^{.286}}{1-\left(\frac{p_\infty}{p_0}\right)^{.286}}\right\}^{0.5} \cdot \left[1-\left\{\frac{1-\left(\frac{p_\infty}{p_{TW}}\right)^{.286}}{1-\left(\frac{p_\infty}{p_0}\right)^{.286}}\right\}^{0.5}\right] \qquad 6.4$$

which is the required equation in p_∞, p_0, p_{TW} and the LOCAL STATIC PRESSURE IN THE WAKE, p_{SW}.

We must now consider the integrals in term IV of Equation 6.1. Their treatment follows the course outlined in Reference 8, where, if we take Equation 6.1 for the flow in free-air and then subtract it from the equation for flow in the wind tunnel, the change in force on the aerofoil in the streamwise sense, due to the walls, may be written (equation (66) of Reference 8) as:

$$\Delta C_D q_\infty S = (C_{DW} - C_{DWF}) q_\infty S + \Delta WF - \Delta WF_F \qquad 6.5$$

WF refers to the streamwise momentum flux through the walls and C_{DW} is the profile drag of the aerofoil. The terms with suffix F are those in free air, in the absence of the tunnel walls. Now C_{DW} in the wind tunnel flow is derived by allowing the conditions in the measuring plane, AB, to relax to mainstream levels. The free-air pressure, being the same, results in the first term on the RHS of Equation 6.5 equalling zero. Furthermore, ΔWF_F may be proved identically equal to zero in the free-air. In other words, the ΔC_D term is a direct result of the net momentum flux through the walls in the wind tunnel flow (as well as local buoyancy effects due to the sidewall suction system) and is thus equivalent to term IV in Equation 6.1. We note that for a solid wall, $\Delta WF = 0$, so that ΔC_D and hence $\Delta\alpha$, tend to zero, if we disregard the aforementioned buoyancy effects. This is indeed what subcritical, first order flow theory would tell us.

In coefficient notation, Equation 6.1 then becomes:

$$C_{NB}\sin\alpha_w + C_{XB}\cos\alpha_w = \left(C_{DW} - C_\mu \frac{u_\infty}{u_j}\right) + \Delta C_D \qquad 6.6$$

The relatively large open area of the tunnel floor and ceiling will cause the predominant correction to be that due to downwash effects; where one would anticipate that $\Delta C_D \triangleq \Delta\alpha C_{NB}$. This correction, however, did not collapse the deduced drag from the sidewall balance on to the data obtained from the wake surveys for a consistency check as $C_{NB} \to 0$, always showed the balance axial force coefficient to read differently from the profile drag coefficient. Consequently, a constant, ΔC_{DO}, was introduced, so that

$$\Delta C_D = \Delta C_{DO} + \Delta\alpha \, C_{NB} \qquad 6.7$$

and where ΔC_{DO} was considered to arise from the net flux of streamwise momentum through the ceiling and floor, at zero lift, due to thickness and camber effects, coupled with any buoyancy effects due to the sidewall suction boundary-layer control system. The incidence correction, $\Delta\alpha$, is the difference between the geometric and corrected angles of attack.

Much of the scatter in the original effort of Reference 1 was eliminated by performing a spanwise integration of the wake profile drag coefficients. To simplify the correction procedure further, we also postulated that $\Delta\alpha$ was directly proportional to C_{NB}, so that

$$\Delta\alpha = KC_{NB} \qquad 6.8$$

Knowing that $\alpha_w \ll 1$ and $\alpha_c \ll 1$, Equation 6.6 was written as:

$$C_{DB} - \left(C_{DW} - C_\mu \frac{u_\infty}{u_j}\right) = KC_{NB}^2 + \Delta C_{DO} \qquad 6.9$$

When a plot of these measured quantities is made at a prescribed Mach number and Reynolds number, the slope K (and hence $\Delta\alpha$) along with the intercept, ΔC_{DO}, allows the corrected angle of incidence and balance drag to be computed for a given aerofoil section.

The corrected lift and drag coefficients are then:

$$C_{LC} = C_{NB}\cos\alpha_c - C_{XB}\sin\alpha_c \qquad 6.10$$

and

$$C_{DC} = C_{NB}\sin\alpha_c + C_{XB}\cos\alpha_c - \Delta C_{DO} \qquad 6.11$$

$$= C_{DW} - C_\mu \frac{u_\infty}{u_j}$$

6.2 Subcritical Flow Method, Using Wall Static Pressure Measurements to Deduce the Different Porosity Factors for the Tunnel Ceiling and Floor

The use of subcritical, linearised flow theory has been a recognised, but sometimes controversial, approach to determine the effects of wind tunnel walls when the mainstream flow is at a high subsonic Mach number. At the distant walls the aerofoil perturbations are usually small enough that the linearisation applies up to high subsonic velocities in the regions along the walls. The aerofoil far field at the wind tunnel walls can be

represented by the flow field generated by a point vortex, whose strength is determined from the lift coefficient of the wing, and by a doublet, whose strength is dependent upon the area of the aerofoil section. A point source may also be included to represent the displacement effect of the wing wake. The singularities are usually and most suitably placed in the vicinity of the aerofoil one-quarter chord position (that is normally close to the centre of pressure and the centroid of the aerofoil cross section) to ensure that effects of the next higher order singularities, whose strengths are represented by the pitching moment and the static moment of the aerofoil area,[10] are negligible. (It is clear that we are now able to select the location of the singularities within the aerofoil on a more logical basis, by matching the position of the computed peak suction pressure close to the wall with that measured in the wind tunnel.) Another important aspect of the vortex and doublet representation is that it applies formally to a far field even if there are local supersonic regions on the aerofoil. There is a difference between the subsonic and transonic scaling rules, of course, but qualitatively the far fields in both cases are similar, see References 22 and 23.

To investigate whether the flow adjacent to the floor and ceiling of the wind tunnel was indeed subcritical or supercritical, a design of static pressure rail was devised to measure pressures adjacent to the wind tunnel walls, but positioned far enough away from the walls to be free from the local disturbance effects of the discrete holes in the ceiling and floor, see Section 2.0.

Once the static pressure measurements along the floor and ceiling were available, it was clear that the flow near the walls was always subcritical, at least for c/H ratios up to 0.25, at $C_L \approx 1$ and at $M_\infty \approx 0.9$. It was then possible to make a valid comparison with the wall pressure distributions predicted by conventional wall interference theory, References 24-28, using a linear characteristic for the walls (velocity component, v, normal to the wall proportional to pressure difference, Δp, across the wall), up to this Mach number.

Now References 29 and 30 indicate that perforated walls usually offer less resistance to flow from the plenum chamber into the test section (inflow) than to flow in the opposite direction (outflow). This is understandable in view of a different flow pattern on the opposite sides of the wind tunnel wall. On the test section side, there is a high speed flow virtually tangent to the wall, whereas on the plenum chamber side, the air is practically at rest.

A mathematical treatment of a "differential" wall characteristic, having different slopes for outflow and inflow along one wall, involves considerable difficulties, since such a boundary condition is, in fact, non-linear. However, a simple solution based on the principle of superposition can still be obtained if there is only inflow along one wall and only outflow along the other wall. The problem is then linear, equivalent to that of two walls with different linear characteristics.

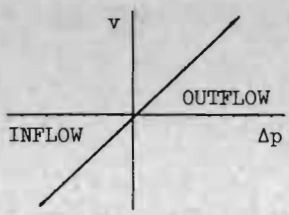

LINEAR CHARACTERISTIC OF PERFORATED WALL

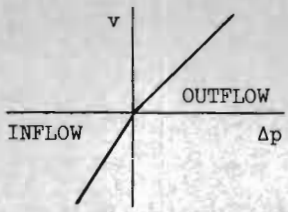

DIFFERENTIAL CHARACTERISTIC OF PERFORATED WALL

INFLOW - From plenum to test section
OUTFLOW - From test section to plenum

This approach, which appears to be realistic, is studied in detail in Reference 11. The analysis shows that along the wall facing the suction side of a (lifting) aerofoil, there is outflow forward of the aerofoil and inflow thereafter, whereas along the wall facing the pressure side, there is only outflow. Of substantial importance, in addition, is that the wall pressure distributions calculated according to the present theory are, in a great many cases, in good agreement with experimental values.

The outcome of the analysis of Reference 11 is that the correction to model angle of attack is written as $\Delta\alpha$ radians:

$$\Delta\alpha = +\frac{1}{4}\frac{c}{H}C_L\left[\frac{t_U+t_L}{2}+\frac{1}{2}\left[\cos\pi\frac{t_U-t_L}{2}-1\right]\right] - \frac{\pi}{4\beta^2}\left(\frac{c}{H}\right)^2 A\left(\frac{t_U+t_L}{2}-\frac{1}{2}\right)\sin\left(\pi\frac{t_U-t_L}{2}\right) \qquad 6.10$$

where t_U and t_L are parameters depending on the porosity factors ascribed to the ceiling and floor of the wind tunnel test section, and A depends on the area of the aerofoil section. We note that the sign of $\Delta\alpha$ here is the same as in Section 6.1 so that $\alpha_c = \alpha_w - \Delta\alpha$.

The correction to the mainstream Mach number was obtained as

$$\Delta M_\infty = (1+0.2M_\infty^2)M_\infty\left[-\frac{1}{8\beta}\frac{c}{H}C_L\sin\left(\pi\frac{t_U-t_L}{2}\right) + \frac{\pi}{6\beta^3}\left(\frac{c}{H}\right)^2 A\left[1-3\frac{t_U+t_L}{2}+\frac{3}{2}\left(\frac{t_U+t_L}{2}\right)^2 - \frac{3}{2}\left(\frac{t_U+t_L}{2}-\frac{1}{2}\right)\left[\cos\left(\pi\frac{t_U-t_L}{2}\right)-1\right]\right]\right] \qquad 6.11$$

The blockage correction appears to be a significant factor, in contradistinction to the case when the walls have equal porosity factors, i.e. $t_U=t_L$. It reduces the mainstream Mach number. We may argue that in the cases where essentially supercritical flows exist around the aerofoil (but not from wall to wall) that the above subcritical correction procedure should not be applicable. We may reason that in such flows, a so-called forbidden zone embedding the aerofoil arises, where the linear solution is no longer valid. Notwithstanding, if the flow adjacent to the walls can be described by Prandtl-Glauert linearised theory, the potential due to the walls, ϕ_w, can still be determined, since the far field potential due to the model, ϕ_M, can still be represented by the vortex and doublet singularities at the model position. The use,

however, of the resulting ϕ_w cannot, we may rationalise, be extended into the forbidden zone - in particular to the aerofoil location - since ϕ_w does not represent a solution to the flow field equations in the non-linear region. On this basis, we must admit that the subcritical procedure to obtain $\Delta\alpha$, ΔM_∞ corrections at high Mach numbers cannot be justified, although we shall use it for purposes of comparison. We should note in passing that the philosophical background for subcritical theory has been intuitive rather than justified by rigorous mathematical proof, and that some of the accepted subtleties of the subcritical theory may certainly be disputed. One is that even in incompressible flow, ϕ_w does not satisfy the boundary condition at the model surface. Moreover, the local combined flow field adjacent to the model singularities, is in no way representative of the model in the wind tunnel flow. The effect of ϕ_w has always been considered as a perturbation to the mainstream alone, and not to the combined flow of the model with the mainstream. Nevertheless, as the mainstream potential will be little different in the transonic régime to that in subsonic flow, it is perhaps not unreasonable to accept that the subcritical approach is perhaps useful up to Mach numbers of say $M_\infty \stackrel{\sim}{=} 0.8$, for the aerofoil and tunnel geometries reviewed herein. Clearly, the continuing use of the subcritical corrections to very high Mach numbers, will lead to exaggerated corrections, since the intensity of flow perturbations in the lateral direction will require, for example, a smaller change in M_∞ or α to cause a given wall effect, than when compared with the subcritical estimates. The appropriate transonic scaling would then be important.

6.3 Finite Difference Calculation

It is well known that viscous effects, arising specifically from the interaction of relatively strong shock waves with the aerofoil turbulent boundary-layers, can cause a drastic modification to the supercritical airflow described in an inviscid framework. For example, for the class of aft-cambered aerofoils considered herein, such viscous effects can cause an appreciable upstream displacement of the upper surface shock wave (10 to 20 percent chord not being unusual) as well as a reduction in the aerofoil aft camber that will alter the entire aerofoil surface pressure distribution. Since we still do not have available a satisfactory calculation procedure to treat the complex viscous/inviscid coupling in these real flows, we have attempted to model the flow field over the rear of the aerofoil using an artifice that we have labelled a "viscous ramp".[31] In so doing, we prescribe the boundary condition at the aerofoil in the following way: we consider that the viscous displacement effects are relatively unimportant along the aerofoil upper surface, ahead of the shock wave; and along the forward half of the lower surface, where, in both instances, we retain the conventional condition of the aerofoil surface slopes. Where we expect important viscous displacement effects, along the aerofoil upper surface, at the station of, and aft of the shock wave, and along the aft portion of the lower surface, we prescribe the measured surface pressures, that must contain some resultant effects of the boundary-layer displacement. The finite difference calculations[12] are then performed using this mixed boundary condition at the surface, the results yielding the surface pressures where the slopes were detailed, and the effective shape of the aerofoil (geometric shape plus displacement layer) where the measured pressures were specified. In this calculation, we attempt to find the displacement thicknesses of the model boundary layers of the configuration in the wind tunnel, using in addition, the measured static pressures adjacent to the tunnel walls as a boundary value input to the calculation.

The above procedure was used to spot-check the wall interference corrections found by the momentum balance and the subcritical flow approaches. The results of the calculations with the wall pressures prescribed and with the aerofoil at a geometric angle of attack, α_w, of 2.36 degrees, at a test Mach number of $M_\infty = 0.812$, are shown on Figures 29.1 and 29.2. Here the calculated pressure distribution on the aerofoil is in reasonable agreement with the measured pressures except in the plateau region on the upper surface, where the bulging in the measurements is due probably to reflected perturbations from less than ideal flow around the nose, perhaps from a small separation bubble. The aft measured pressures that were prescribed in the calculations are distinguished by the different symbol. There is a satisfactory consistency of the initial wedge angle of the viscous ramp with the value of the surface Mach numbers upstream and downstream of the shock wave corresponding with the case of a "strong" attached shock wave.

In Figure 28.1, the slopes of the viscous ramp on the aerofoil upper surface may be interpreted to indicate the presence of a local separation bubble (the initial wedge) followed by a reattached flow and a final thickening of the boundary-layer as the trailing-edge is approached. On the lower surface a similar thickening is also suggested.

Although this calculation procedure appears plausible for the effective displacement surface of the aerofoil, two potential drawbacks should be cited. First of all, we should mention that the two to three percent loss in stagnation pressure across the upper surface shock wave has not been included in the measurements, so that the aft surface pressure ratios that are based on the upstream stagnation pressure will yield local Mach numbers that will be in slight error. And secondly, and perhaps of greater importance, there are transverse (normal) pressure gradients generated in the boundary-layer, in regions of shock induced boundary layer separation and high surface curvature, so that the static pressure measured at the aerofoil surface may not be that at the boundary-layer edge. (For example, see Reference 32, and the more recent work of Myring and Young[33].) In fact, the boundary-layer "softens" the pressure rise, so that the pressures measured at the edge of the boundary-layer exhibit a much sharper rise than those measured at the aerofoil surface. Hence, depending on the severity of the normal pressure gradients, we can see that the utilisation of the surface pressures might yield a displacement surface in our calculation that is not tangential to the direction of the local streamline, and in so doing, we do not obtain the true aerofoil shape.

Bearing these qualifications in mind, the inviscid flow calculation was repeated, keeping the same angle of attack and mainstream Mach number and retaining the "viscous ramps" as determined above, but removing the constraint of the pressures at the

tunnel walls, and prescribing instead, the mainstream conditions at infinity. The resulting pressure distribution is shown on Figure 30. We note that the upper surface pressures in the nose region are virtually unaffected by the wall interference, with changes between the upper surface pressures being confined to locations further downstream. The large changes downstream of the shock wave are perhaps due to the retention of a viscous ramp now somewhat incompatible with the changed state of the flow. The other significant effect of the wall interference appears on the lower surface, where there is a decrease in the level of overpressures over most of the chord. At a constant angle of attack, and assuming no blockage correction, we then have a measure of the wall interference, ΔC_L, from integrations of the two pressure distributions. The free-air case provides us with a point X on Figure 31.

Alternatively, we can also look at the problem of wall interference in the light of finding a "free-air" case that recovers the measured wind tunnel pressure distribution at a new angle of attack (and if necessary, a new Mach number). Neglecting the small change in Mach number likely to result, this would yield a correction to α at a virtually constant C_L. A calculation in free-air at $M_\infty = 0.812-0.025$ and $\alpha = \alpha_w - 0.49$, actually reproduced the experimental pressure distribution as shown on Figure 30, and this flow case is indicated as point Y on Figure 31. In this calculation, we have retained the original viscous ramps of Figure 29.1, which should not be unreasonable, since the original measured pressure distribution has been recovered with what we assume is a corrected α and M_∞.

6.4 Test Results from all Three Methods

Figure 32 shows the results at mainstream test Mach numbers close to 0.8, of plotting the difference between uncorrected balance drag and wake profile drag, corrected for jet flap momentum supply from outside the wind tunnel, versus the square of the normal force coefficient. We remember that the slope, K, of this graph, along with the intercept on the ordinate axis that yields ΔC_{DO}, are the substance of the empirical streamwise momentum approach discussed in Section 6.1. We note on Figure 32, where configurations with and without blowing are plotted together, that there is no clear dependency of the slope K on the aerofoil geometries. Single graphs of K versus M_∞ for all configurations, and one for ΔC_{DO} versus M_∞, were hence obtained to summarise these wall interference factors - see Figure 33. Third order curve fits were made to the experimental results. One clear discrepancy is the K value at $M_\infty \triangleq 0.7$, and no explanation is evident for this anomaly. The K and ΔC_{DO} factors on Figure 33 were applied to obtain $\Delta\alpha$ (and thus α_c) and the corrected balance lift and drag values were as given in Equations 6.10 and 6.11 and where the weighted profile drag coefficient

$$C_{DW} = \frac{1}{3}\left(C_{DW1} + C_{DW2} + C_{DW3}\right) ,$$

the numbers 1, 2 and 3 denoting the respective section profile drag coefficients at the three pitot tubes (see Figure 9).

A measure of the consistency that results between C_{DC} and C_{DWC} is indicated in Figures 34 and 35. Some discrepancies are noted at the high lift values, and these result in part from non-uniformities in the wake flow generated by the strong interactions between the wing shock wave(s) and boundary-layers. The corrected $C_L - \alpha$ plot for Aerofoil I and $M_\infty \triangleq 0.8$ is illustrated on Figure 31.

Figures 36 and 37, on the other hand, show comparison between some calculated wall pressure distributions from the subcritical flow method and those from the experiment, at Mach numbers equal to 0.7 and 0.8. The respective negative and positive values of pressure coefficient along the ceiling and the floor of the wind tunnel are symptomatic of the inflow into, and the outflow out of, the wind tunnel test section through the walls. As we might expect, the absolute values of the wall pressure coefficients become progressively larger as the wing lift increases. We see on these figures, that when the values of the floor and ceiling porosity factors, $P_F = 0.5$ and $P_C = 1.5$ are used, there is substantial agreement between the calculated and measured pressure coefficients. The corresponding calculated angle of attack correction, $\Delta\alpha$, and blockage correction to Mach number, ΔM_∞, are shown adjacent to the charts. Some discrepancy exists as $C_L \to 0$, because suction and compression zones exist on each side of the aerofoil, the effects from which appear to extend to the walls. We note moreover, on Figure 37.2, that the experimental wall pressure distributions appear to depend more-or-less upon the lift coefficient and not upon the means to produce the lift. For example, for Aerofoil I at $C_{NB} = 1.071$, the wall pressure distributions measured when $C_\mu = 0$ at $\alpha_w = 5.5$ degrees and when $C_\mu \triangleq 0.02$ at $\alpha_w = 1.20$ degrees, bear close resemblance.

In contrast, however, we should discuss the results depicted on Figure 38, where the measured wall pressure distribution at $M_\infty = 0.812$ and $\alpha_w = 2.36$ degrees, is set against equivalent free-air pressure distributions, calculated according to subcritical linearised theory, and according to the finite difference method of Magnus and Yoshihara. The first impression is the most significant effect of the wall interference. The second is that even though the flow is subcritical, the finite difference calculation exhibits fore and aft asymmetry when compared with the Prandtl-Glauert result, indicating that at least in the free-air, the flow field is non-linear at the station where the line of static pressures was situated in the wind tunnel flow. A logical extrapolation of these findings with the finite difference method, then, would lead one to presume that the flow, adjacent to the walls in the wind-tunnel, although subcritical, would also be non-linear. If one accepts this statement, we obviously have contradicted the fundamental assumption of the subcritical flow analysis!

Clearly, the results of our three methods of attempting to assess wind tunnel wall interference, produce differing results. The differences for a typical example are displayed on Figure 31, on the lift/angle of attack plots for Aerofoil I at $M_\infty \triangleq 0.8$. The streamwise momentum and the subcritical flow approaches produce $\Delta\alpha$ (and hence α_c) values that are relatively close to one another. On the other hand, the differing porosity factors attributed to the floor and ceiling yield significant blockage effects for our tunnel wall geometry of 20 percent porosity, in contrast with earlier results obtained assuming the same porosity factors.[9,10]

And then in our third try of assessment, with the finite difference method, the computed $\Delta\alpha$ is only about 30 percent of that found by the previous two methods, although the blockage Mach number agrees with that found in the subcritical analysis for the case that we spot-checked (the same $M_\infty \cong 0.8$, $\alpha_w = 2.36$ degrees flow for Aerofoil I). The resolution of the wing balance normal and axial force coefficients through α_c derived with respect to the finite difference $\Delta\alpha$ correction, however, produces a drag coefficient thirty percent larger than the measured wake profile drag coefficient, which appears unreasonable.

One further point of conflict between the subcritical assessment and that from the spot check finite difference result concerns the porosity factors. The perforated wall boundary condition is assumed to be given by

$$\phi_x \pm \frac{1}{P}\phi_y = 0$$

where ϕ_x and ϕ_y are perturbation velocities; P is the wall porosity factor characterising the wall; and the optional signs are associated with the upper and lower walls. Since we have measured $C_p \sim \phi_x$ at the wall, and have calculated, utilising the finite difference programme, the corresponding ϕ_y distribution, we can thereby determine the distribution of P along the walls. Such distributions are plotted on Figure 39. The results here indicate that for this same $M_\infty = 0.8$ flow case considered previously, the P factor can be taken as a constant along the floor at about 0.5, which was the result alluded to from the subcritical flow analysis. Along the upstream portion of the tunnel ceiling, P is still close to 0.5, but thereafter it departs from a constant as we proceed downstream. The infinite value of P on the ceiling where ϕ_x, $\phi_y \to 0$ indicates the inadequacy of the postulated perforated wall boundary condition in this region. If we neglect this region, we see that a more-or-less uniform P factor exists where there is an outflow from the test section to the wind tunnel plenum chamber, while departures from a constant P value arise directly above and downstream of the aerofoil where an inflow is present. The monotonically increasing P in this region indicates a growing tendency of the wall to behave increasingly as an open jet. The increasing "softening" of the tunnel ceiling here can be attributed to the growing buffer layer of low energy air adjacent to the wall, that emanates from the ceiling plenum chamber. We see that the arbitrary prescription of the ceiling porosity factor at $P_c \cong 1.5$ in the subcritical analysis, is perhaps difficult to justify on the basis of Figure 39.

The non-uniqueness of the wall corrections raises doubts as to which correction technique is to be preferred. In basing the correction procedure on a match of the aerofoil surface pressures when an M_∞ correction is also required (in the finite difference calculations) the representation of the distributions in p/p_o format is more logical than the usual pressure coefficient form, since in homentropic flow, the local value of p/p_o depends only upon the local Mach number, whereas C_p depends in addition upon the mainstream Mach number. Any anomalies in the determination of the mainstream Mach number are then removed from the pressure distribution data, if the p/p_o format is adopted. (We remember that

$$C_p = \frac{p-p_\infty}{q_\infty} = \frac{p}{p_o}\frac{(1+\cdot 2M_\infty^2)^{3\cdot 5}}{0.7M_\infty^2} - \frac{1}{0.7M_\infty^2}\ )$$

The use of the finite difference procedure for the determination of the wall corrections is relatively unassailable in principle, as long as the inputs are reliable and an (M_∞,α) correction is meaningful. However, the discrepancy between the resolved drag using α_c and the profile drag; the possible difficulty in interpreting a true δ^* line because of normal pressure gradients; and the determination of $\Delta\alpha$, ΔM_∞ so far at only one Mach number and angle of attack; must preclude any judgement at this time on the effectiveness of the finite difference procedure for assessing wall interference, until more test cases have been tried.

7.0 Concluding Remarks

In transonic flow, the use of aft camber, jet flaps and slot blowing in combination, leads to significant increases in the maximum (buffet-free) lift coefficient obtained; or, for a given high C_L, a substantial improvement in the drag polars, with decreases in the drag coefficient of several times C_μ. The onset of buffet could be delayed to lift coefficients, greater than 1.5, with expenditure of blowing C_μ equal to 0.02. These gains were accompanied by a rearward shift in the centre of pressure, the consequence of which will depend upon the aircraft configuration into which the high lift device is incorporated.

The significant high Reynolds number of the tests, namely 30 million based on the aerofoil 15-inch chord, restrains the scale of the separations to relevant values. At more conventional wind tunnel test Reynolds numbers, we would not see the highly localised shock-induced separation bubbles, and trailing-edge separations, that are obtained herein. Lower Reynolds numbers increase the scales of disturbance of the aerofoil boundary-layers and reduce the aerofoil performance, as we proved in earlier tests.[1] Moreover, leading-edge pressure "peakiness" was invariably present in the results.

Although progress on tunnel wall interference effects has been achieved in the present study, the results have posed as many new queries as they have answered, and have served to illustrate how difficult our ultimate goal may be of acquiring a viable and absolute wall correction.

Acknowledgements

The authors would like to express their gratitude to Mr. R. Murray of Convair, and to Mr. G. Lanouette of NAE for their expert technical assistance during the wind tunnel programmes; and to the painstaking efforts of the NAE 5 ft × 5 ft Blowdown Wind Tunnel Group, which under the guidance of Mr. R.H. Piper, provided the basis for the successful tests. We should also like to thank Mr. J. Ashley and Mr. D. Thomason of NAE who spent considerable hours in preparing the illustrations. The General Dynamics participation was funded by the U.S. Office of Naval Research (Code 461).

References

1. Peake, D.J., Yoshihara, H., Murray, R., Carter, W., "The Transonic Performance of Two-Dimensional Jet-Flapped Aerofoils at High Reynolds Number", AGARD CP-83-71, April 1971.

2. Yoshihara, H., Magnus, R., Zonars, D., "Transonic Drag Due to Lift of Planer Jet-Flapped Airfoils", AGARD CP-124, April 1973.

3. Stratford, B.S., "Mixing and the Jet Flap", The Aeronautical Quarterly, Volume VII, May 1956, pp. 85-105.

4. Pearcey, H.H., Stuart, C.M., "Methods of Boundary-Layer Control for Postponing and Alleviating Buffetting and Other Effects of Shock-Induced Separation", IAS Paper FF22, June 1959.

5. Peake, D.J., "The Use of Air Injection to Prevent Separation of the Turbulent Boundary-Layer in Supersonic Flow", ARC CP-890, 1966.

6. Grahame, W., Headley, J., "Recent Experience in the Transonic Testing of Two-Dimensional Swept and Straight Wings with High Lift Devices", AGARD CP-83-71, April 1971.

7. Peake, D.J., Bowker, A.J., "Phase 1 and 2 Transonic Wind Tunnel Tests in the 15 × 60-inch 2-D Insert of Peaky-Nosed, Aft-Cambered Aerofoil Sections Incorporating Jet Flaps", NRC NAE Wind Tunnel Project Report 5×5/0055, and LTR-HA-5×5/0056, October 1972 and March 1973.

8. Peake, D.J., Bowker, A.J., "A Simple Streamwise Momentum Analysis to Indicate an Empirical Correction to Angle of Incidence in Two-Dimensional Transonic Flow due to a Perforated Floor and Ceiling of the Wind Tunnel", NRC NAE LTR-HA-11, 1973.

9. Mokry, M., "Analysis of the Subsonic Wall Interference Effects in a Two-Dimensional Perforated Wall Wind Tunnel", NRC NAE LTR-HA-5, June 1970.

10. Mokry, M., "Higher-Order Theory of Two-Dimensional Subsonic Wall Interference in a Perforated Wall Wing Tunnel", NRC Aeronautical Report, LR-553, October 1971.

11. Mokry, M., Peake, D.J., Bowker, A.J., "Wall Interference on Two-Dimensional Supercritical Airfoils, using Wall Pressure Measurements to Determine the Porosity Factors for Tunnel Floor and Ceiling", NRC Aeronautical Report LR-575, 1974.

12. Magnus R., Yoshihara, H., "Steady Inviscid Transonic Flows over Planar Airfoils - A Search for a Simplified Procedure", NASA CR-2186, 1972.

13. Peake, D.J., Galway, R.D., "The Three-Dimensional Separation Produced by a Circular Cylinder Mounted Normal to a Flat Plate", NRC Aeronautical Report, LR-428, May 1965.

14. Ohman, L.H., Brown, D., "The NAE High Reynolds Number 15-inch × 60-inch Two-Dimensional Test Facility; Part 2, Results of Initial Calibration", NRC NAE LTR-HA-4, September 1970.

15. Brown, D., Ohman, L.H., "Further Calibration of the 15-inch × 60-inch Two-Dimensional Test Facility with 6% Open Floor and Ceiling at the Test Section", NRC NAE Wind Tunnel Project Report 5×5/0050, September 1971.

16. Peake, D.J., Bowker, A.J., "Phase 3 Transonic Wind Tunnel Tests in the 15 × 60-inch 2-D Insert of Peaky-Nosed, Aft-Cambered Aerofoil Sections Incorporating Jet Flaps and Slot Blowing", NRC NAE Wind Tunnel Laboratory Test Report, LTR-HA-5×5/0071, January 1974.

17. Howarth, L., Ed., "Modern Developments in Fluid Dynamics - High Speed Flow - Vol. II", Oxford: at the Clarendon Press, 1956, Ch. XI, p. 32.

18. Yoshihara, H., Magnus, R., Carter, W., Murray, R., "Lift Augmentation on Planar Airfoils in the Transonic Régime - a High Reynolds Number Wind Tunnel Study", Convair Aerospace Report, CASD-NSC-73-001, September 1973.

19. Sears, W.R., "Self-Correcting Wind Tunnels", Calspan Report No. RK-5070-A-2, July 1973.

20. Gomer, H.C., Rogers, E.W.E., Acum, W.E.A., Maskell, E.C., "Subsonic Wind Tunnel Wall Corrections", AGARDograph 109, 1966, Ch. 6.

21. Yoshihara, H., "Some Recent Developments in Planar Inviscid Transonic Airfoil Theory", AGARD-AG-156, February 1972.

22. Cole, J.D., "Twenty Years of Transonic Flow", Boeing Scientific Research Laboratories Document D1-82-0878, July 1969.

23. Murman, E.M., "Computation of Wall Interference Effects in Ventilated Transonic Wind Tunnels", AIAA Paper No. 72-1007, September 1972.

24. Goodman, T.R., "The Porous Wall Wind Tunnel, Part II, Interference Effect on a Cylindrical Body in Two-Dimensional Tunnel at Subsonic Speed", AD-594-A-3, Cornell Aero. Lab., Buffalo, New York, November 1950.

25. Kassner, R.R., "Subsonic Flow over a Body Between Porous Walls", Tech. Report 52-9, Weight Air Dev. Center, 1952.

26. Baldwin, B.S., Jr., Turner, J.B., Knechtel, E.D., "Wall Interference in Wind Tunnels with Slotted and Porous Boundaries at Subsonic Speeds", NACA Tech. Note 3176, Ames Aero. Lab., Moffett Field, California, May 1954.

27. Maeder, P.F., Wood, A.D., "Transonic Wind Tunnel Test Sections", Zeitschrift für angewandte Mathematik und Physik, Vol. 7, 1956, pp. 177-212.

28. Wright, R.H., "The Effectiveness of the Transonic Wind-Tunnel as a Device for Minimizing Tunnel-Boundary Interference for Model Tests at Transonic Speeds", AGARD Report 294, March 1959.

29. Chew, W.L., "Characteristics of Perforated Plates with Conventional and Differential

Resistance to Cross-Flow and Airflow Parallel to the Plates", Proceedings of PWT Transonic Seminar, Vol. 1, July 1956.

30. Lukasiewicz, J., "Effects of Boundary-Layer and Geometry on Characteristics of Perforated Walls for Transonic Wind Tunnels", Aerospace Engineering, April 1961.

31. Yoshihara, H., Magnus, R., "Wind Tunnel Wall Interference in Recent High Reynolds Number Transonic Tests on Two-Dimensional, Supercritical Aerofoils", General Dynamics/Convair Aerospace Rept. No. GDC-ERR-73-011, December 1973.

32. Howarth, L., Ed., "Modern Developments in Fluid Dynamics - High Speed Flow - Vol. II", Oxford: at the Clarendon Press, 1956, p.617.

33. Myring, D., Young, A., "The Isobars in Boundary Layers at Supersonic Speeds", The Aeronautical Quarterly, Vol. XIX, May 1968, pp. 105-126.

Appendix A

List of Symbols

(Any symbols not listed are defined in the text.)

a_j^*	sonic velocity at jet slot exit
α	angle of incidence of aerofoil in free-air
α_{BO}	geometric angle of incidence at the onset of buffetting
α_c	corrected angle of incidence derived from α_w; that is, corrected for tunnel top and bottom boundary constraints
α_w	geometric angle of incidence between wing chord-line and tunnel centre-line
c	aerofoil chord, equal to 15 inches
C_D	drag coefficient
C_{DB}	"uncorrected" drag coefficient of aerofoil section corresponding with α_w
C_{DC}	"corrected" drag coefficient of aerofoil section corresponding with α_c
C_{DW}	profile drag of aerofoil as measured by wake traverse, determined from integrating (that is, weighting) measurements from probes 1, 2 and 3
C_{DWC}	profile drag corrected for addition of momentum in jet flap flow/slot blowing flow from outside the tunnel, $\equiv C_{DW} - C_\mu \frac{u_\infty}{u_j}$
C_{LBO}	lift coefficient at buffet onset
C_L	lift coefficient
C_{LMAX}	maximum value of lift coefficient
C_{MC4}	pitching moment coefficient about 1/4-chord point of aerofoil
C_{MC4B}	pitching moment coefficient about 1/4-chord point of aerofoil, from sidewall balance measurements
C_{MC4P}	pitching moment coefficient about 1/4-chord point of aerofoil, from integration of centre-line static pressure measurements about aerofoil contour
C_μ	blowing momentum coefficient of jet flap, or jet slot, $\frac{\dot{m}_j u_j}{q_\infty S'}$
C_N	normal force coefficient; direction is normal to chord-line
C_{NMAX}	maximum value of normal force coefficient
C_{NB}	normal force coefficient, derived from sidewall balance measurements
C_{NP}	normal force coefficient, derived from integration of wing static pressures
C_p	pressure coefficient, $\frac{p-p_\infty}{q_\infty}$
C_{pDISC}	pressure coefficient, $\frac{p_{DISC}-p_\infty}{q_\infty}$, measured by means of disc static probe
C_{pTE}	pressure coefficient at or near aerofoil trailing-edge
C_p^*	pressure coefficient, $\frac{p^*-p_\infty}{q_\infty}$, corresponding with local sonic conditions at a given mainstream Mach number
C_{XB}	axial force coefficient, derived from sidewall balance measurements
f	frequency, Hz
h	vertical distance in direction of wake traverse
H	tunnel height
K	slope of $\Delta\alpha$ versus C_N curve
$(L/D)_{MAX}$	maximum lift/drag ratio of aerofoil section
$\dot{m}_j$	jet slot mass flow per sec
M_∞	mainstream Mach number
N_{2N}	"north" component of normal force measured by strain gauge network on flexure aft of balance centre (on wing port side)
P	porosity factor of wind tunnel floor or ceiling
p	local static pressure anywhere in the flow-field
p_D	stagnation pressure in jet flap blowing duct
p_∞	mainstream static pressure
p_0	stagnation pressure of tunnel mainstream
p_W	static pressure on wing at x/c = 0.50
p_{SW}	static pressure in wake survey plane
p_{TW}	pitot pressure in wake survey plane
ϕ	perturbation velocity potential
q_∞	dynamic pressure of mainstream flow
R_c	Reynolds number based on aerofoil chord and mainstream conditions
S	planform area of wing
S'	planform of wing consistent with span of jet slot

t_L, t_U	$\frac{2}{\pi} \tan^{-1} \frac{P_{L,U}}{\beta}$, $0 \leq t_{L,U} < 1$; wall porosity parameters
θ	slope of aerofoil surface with respect to wing chord-line, in degrees
θ_j	angle of jet flap efflux to aerofoil chord-line
θ_s	angle of slot boundary-layer control efflux to aerofoil chord-line
θ_{TE}	nominal flap angle of aft-cambered section of aerofoil with respect to section chord-line
u	local velocity parallel to tunnel centre-line
u_∞	mainstream velocity
u_j	jet velocity, assuming flow expands isentropically to mainstream p_∞
v	local velocity normal to tunnel centre-line, towards top perforated wall
x	distance along aerofoil chord from leading-edge; also used for distance along tunnel axis
y	distance normal to tunnel centre-line
z	distance from sidewall in spanwise sense; origin at starboard sidewall
$\Delta\alpha$	correction to angle of incidence, $=\alpha_w - \alpha_c$
ΔC_D	drag correction, see Equation 6.7
ΔC_{DW}	$C_\mu \frac{u_\infty}{u_j}$, correction to measurement of wake profile drag, due to addition of momentum from outside of the wind tunnel flow
ΔC_{DO}	correction to drag at zero lift, see Equation 6.7
ΔC_N rms	root-mean-square of fluctuating normal force coefficient measured on sidewall balance rear normal force element
ΔM_∞	correction to mainstream Mach number due to blockage
Δp rms	root-mean-square of fluctuating pressure measured in tunnel stream or upon wing surface

Suffices

BO	buffet onset
∞	wind tunnel mainstream conditions
j	jet flap efflux
s	blowing slot efflux

Appendix B

Abbreviations

I	Aerofoil No. I
IJ	Aerofoil No. I with Jet Flap, $\theta_j = 85°$, unless otherwise noted.
II	Aerofoil No. II
IIJ	Aerofoil No. II with Jet Flap
IIS	Aerofoil No. II with Slot Blowing
IISJ	Aerofoil No. II with Slot Blowing and Jet Flap
IF2J	Aerofoil No. 1 with Flap Addition F2 and Jet Flap
dB	deciBel
mV	millivolt
psia	lb.wt. per sq.in.
rms	root-mean-square
2-D	two-dimensional

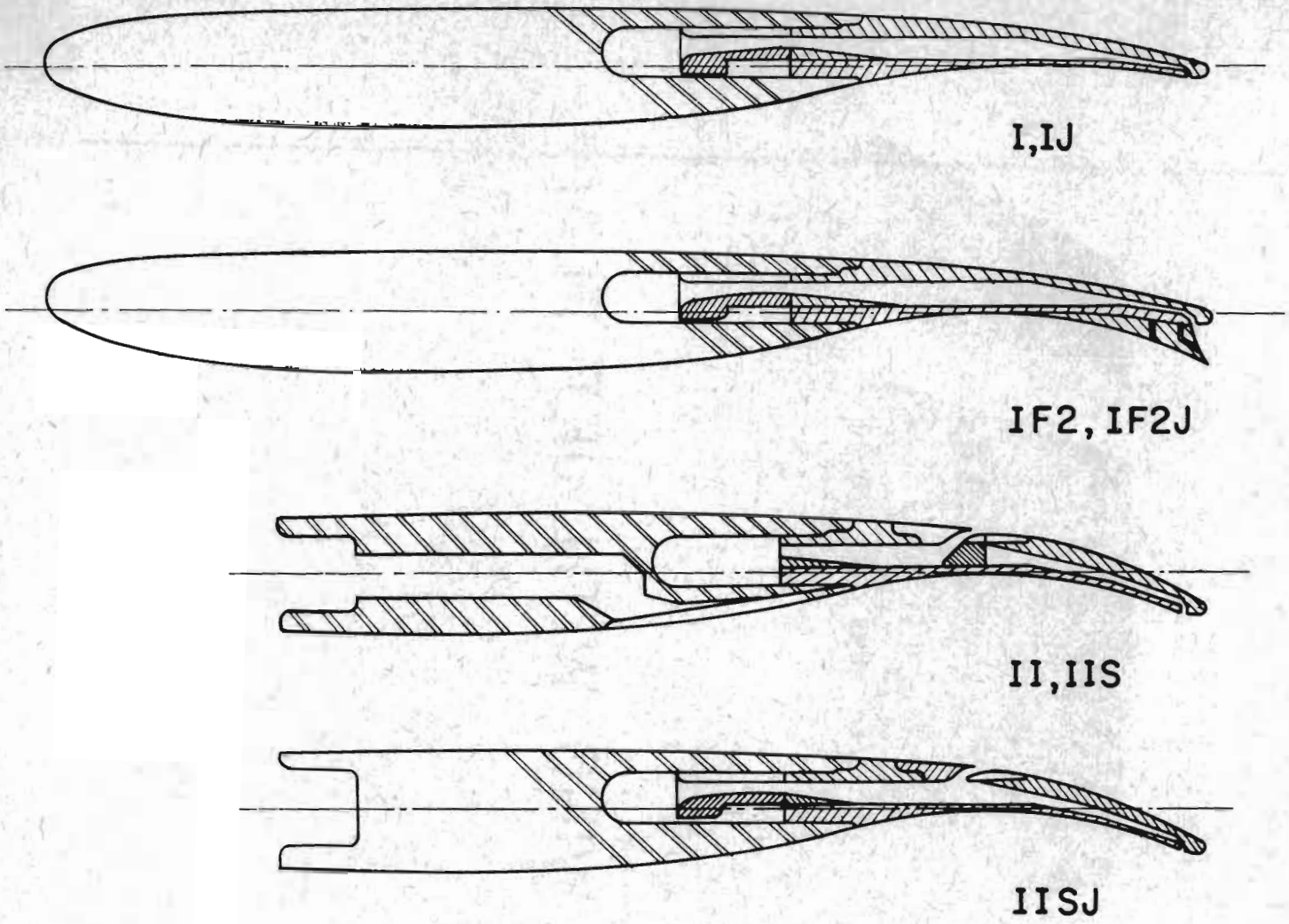

AEROFOIL CONFIGURATIONS

FIG. 1

FIG. 2

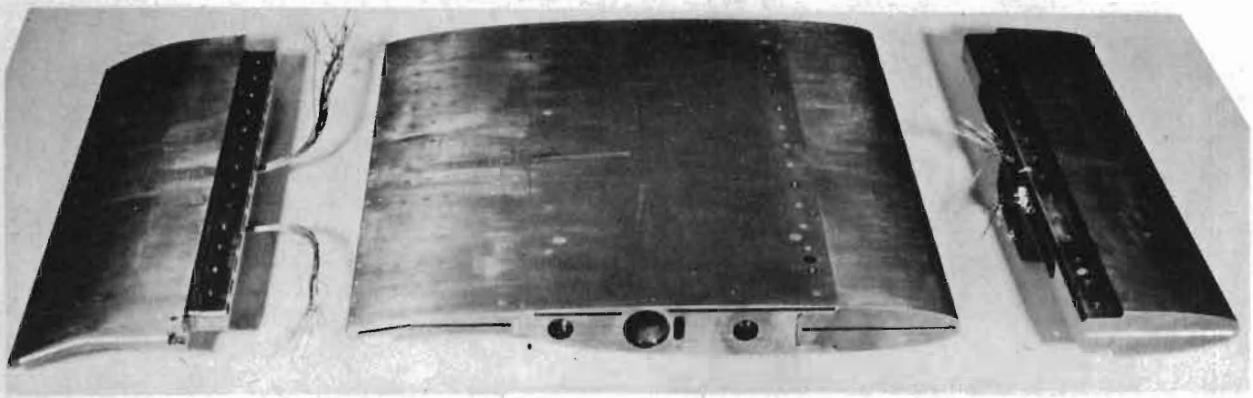

MODEL WING WITH JET FLAP

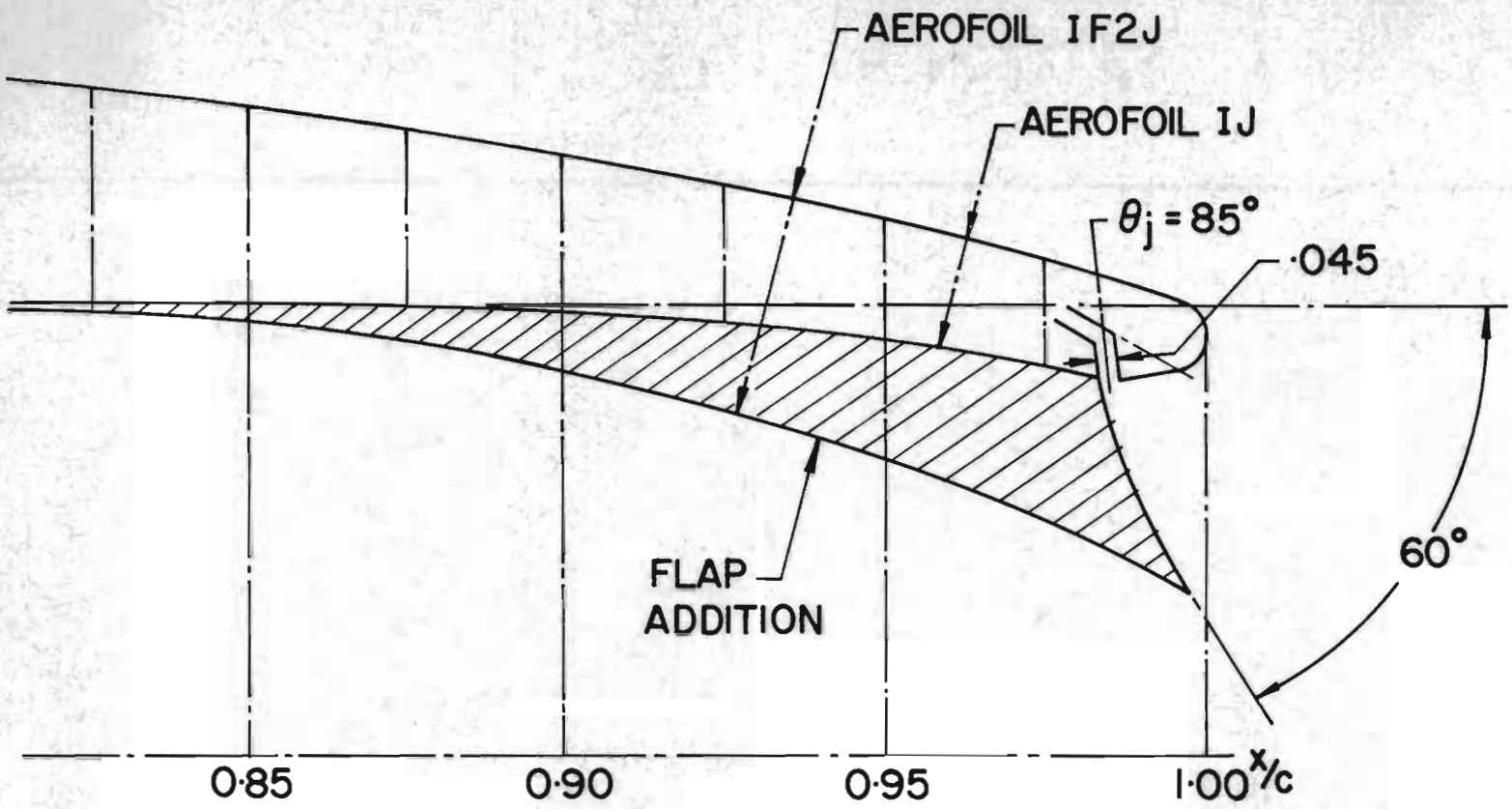

DETAILS OF AEROFOILS IJ AND IF2J

FIG. 3.1

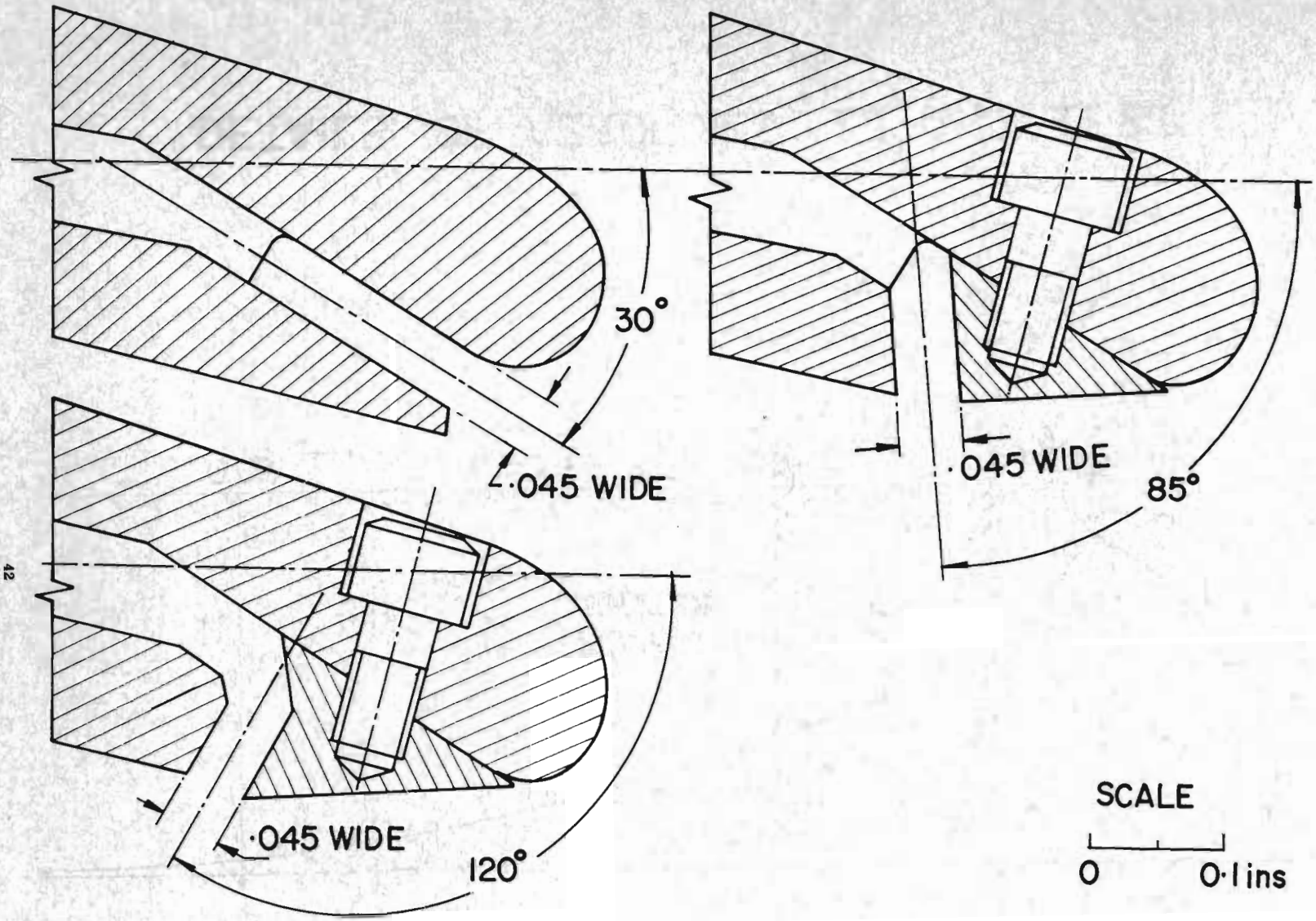

JET FLAP NOZZLES

FIG. 3.2

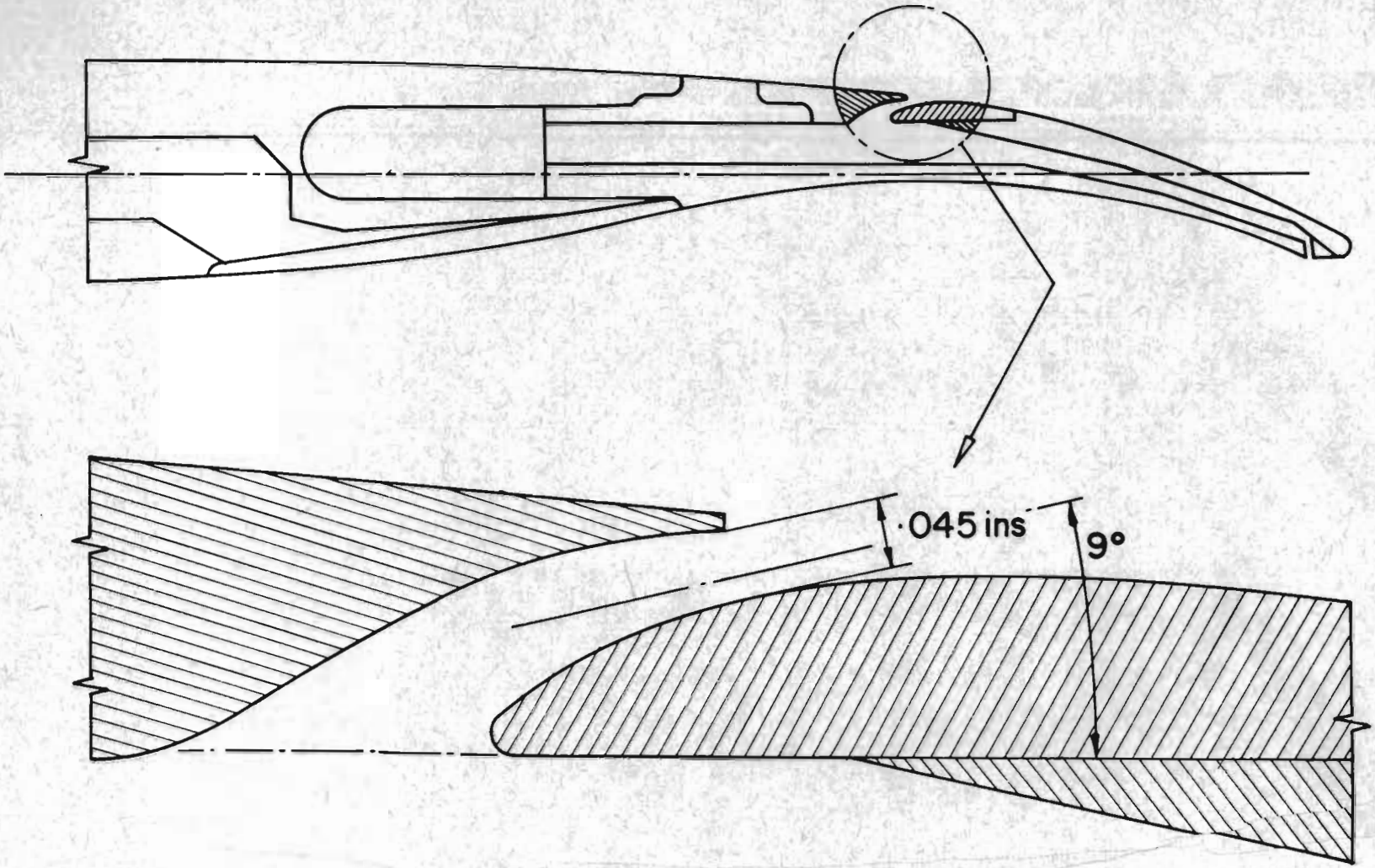

SLOT BLOWING NOZZLE ON AEROFOIL II

FIG. 3.3

FIG. 4

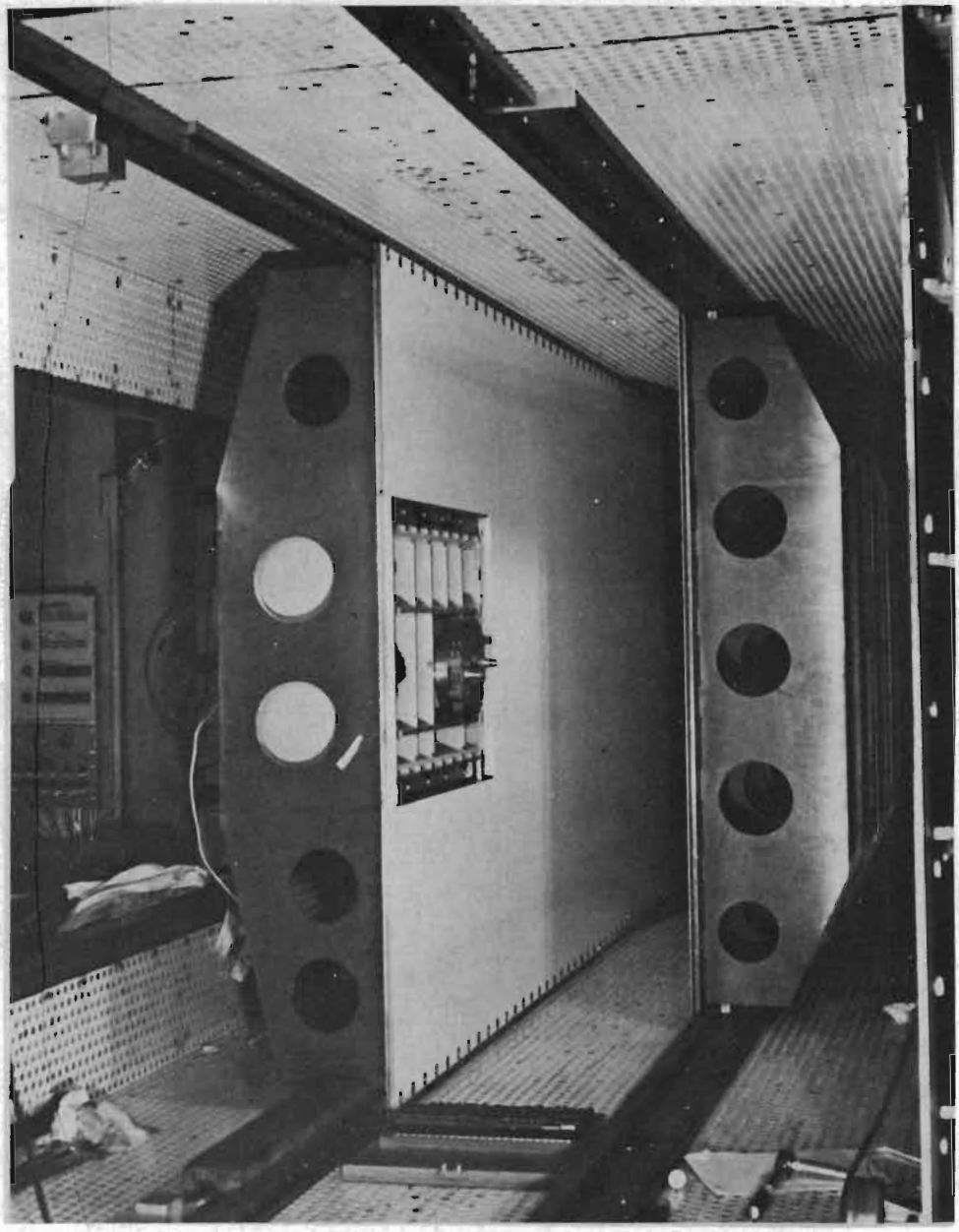

INSTALLATION OF 2-D INSERTS INTO THE 60 INCH X 60 INCH TRANSONIC WORKING SECTION

FIG. 5

RUN No 8057 TOP SIDE

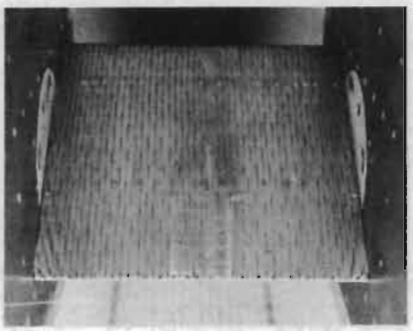

$C\mu = 0, \alpha_w = 2.31°; C_{NB} = 0.704$

UNDERSIDE

RUN No 8054 TOP SIDE

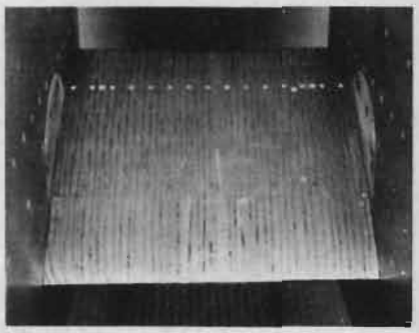

$C\mu = 0.019, \alpha_w = 2.17°, C_{NB} = 1.074$

RUN No 8052 TOP SIDE

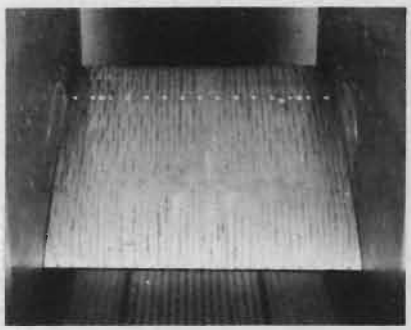

$C\mu = 0.029, \alpha_w = 2.18°; C_{NB} = 1.154$

INDICATORS OF FLOW TWO-DIMENSIONALITY: FLOW VISUALISATION AT SIDEWALL SUCTION VELOCITY RATIO, $v_N / u_\infty \cong 0.0055$, AT $M_\infty \cong 0.8$ AND $R_c \cong 30.10^6$

FIG. 6.1

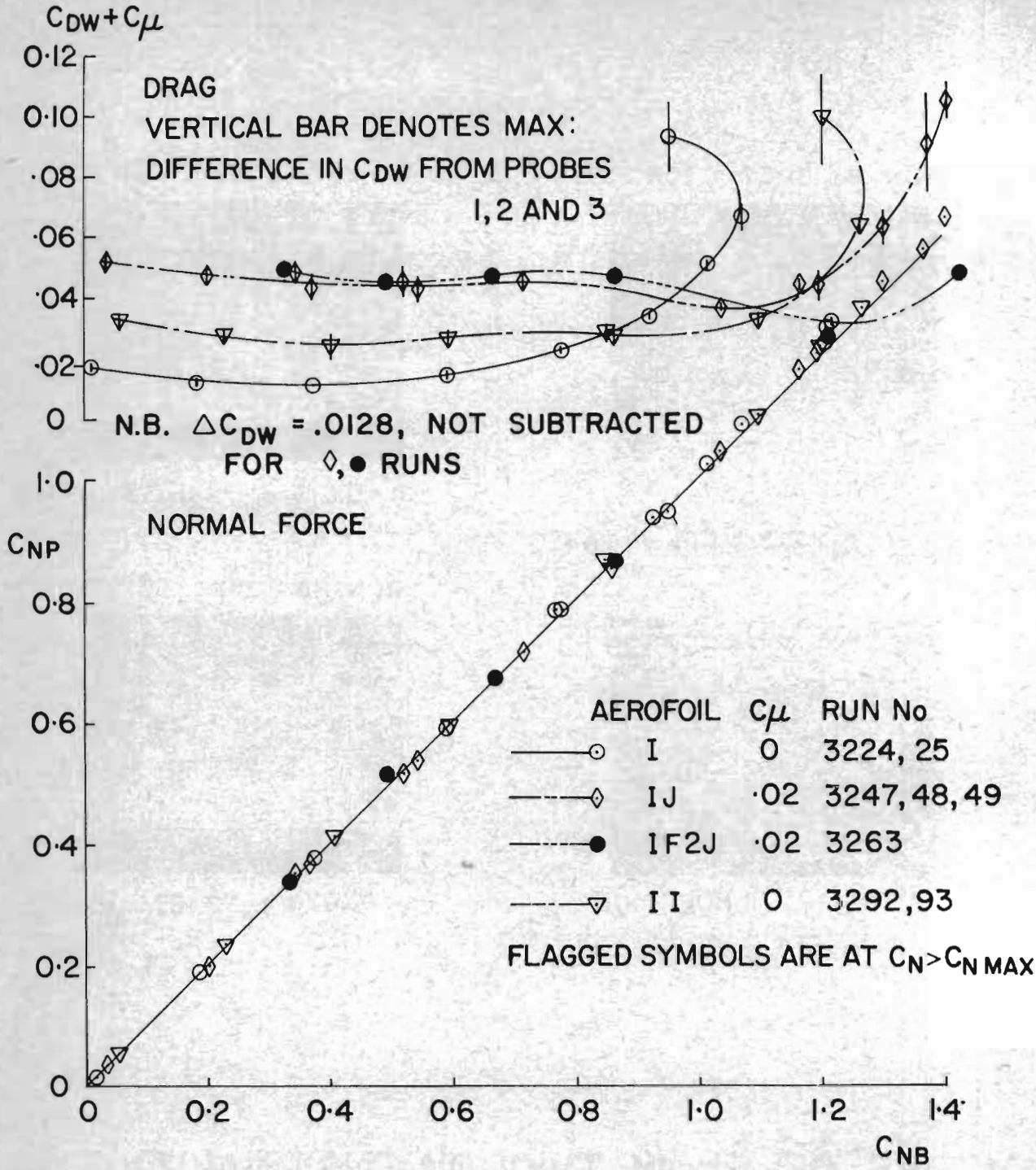

INDICATORS OF FLOW TWO-DIMENSIONALITY: FORCES FROM AEROFOILS I AND II AT $M_\infty \cong 0.8$

FIG. 6.2

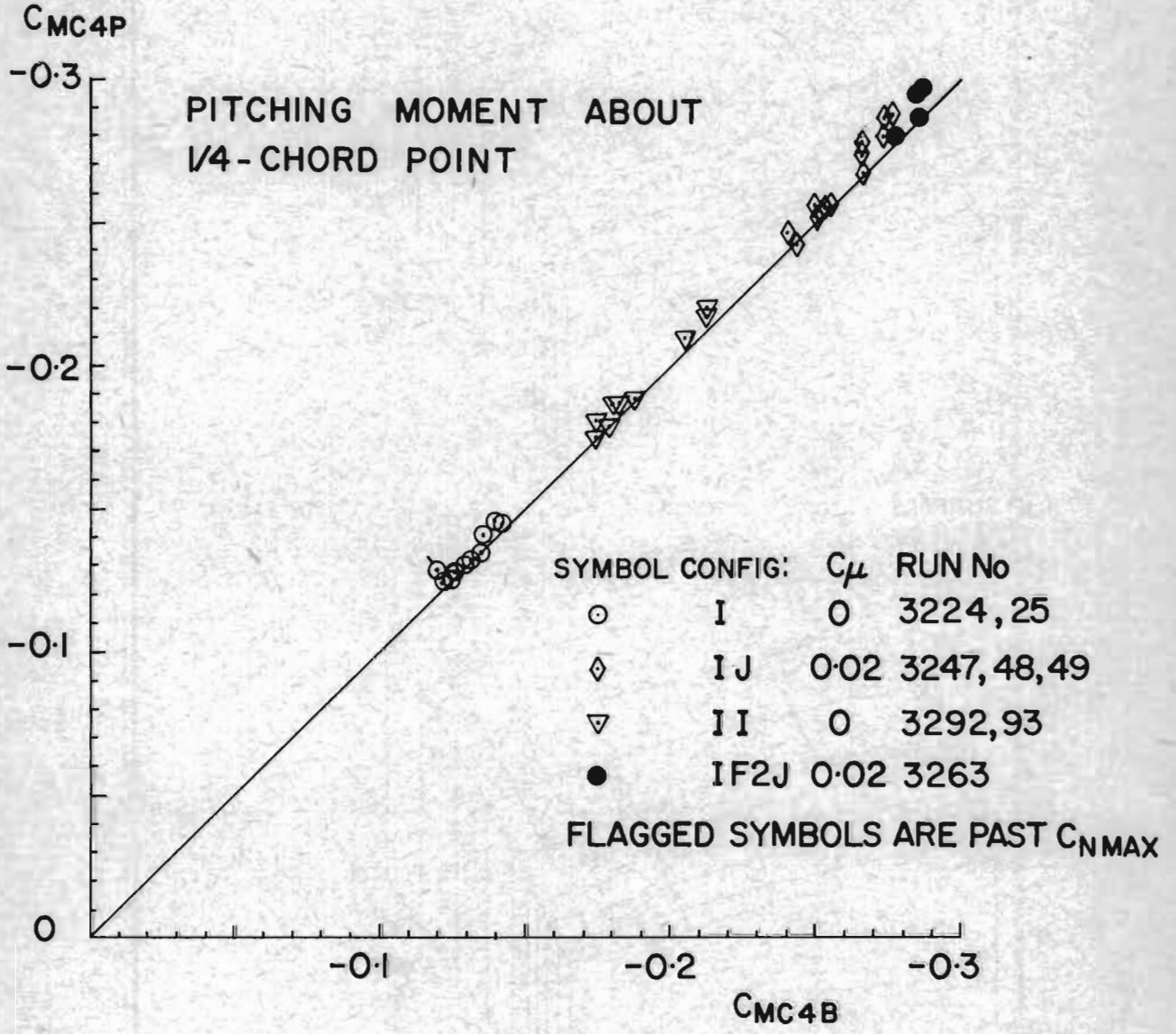

INDICATORS OF FLOW TWO-DIMENSIONALITY: PITCHING MOMENTS FROM AEROFOILS I AND II AT $M_\infty \cong 0.8$

FIG. 7.1

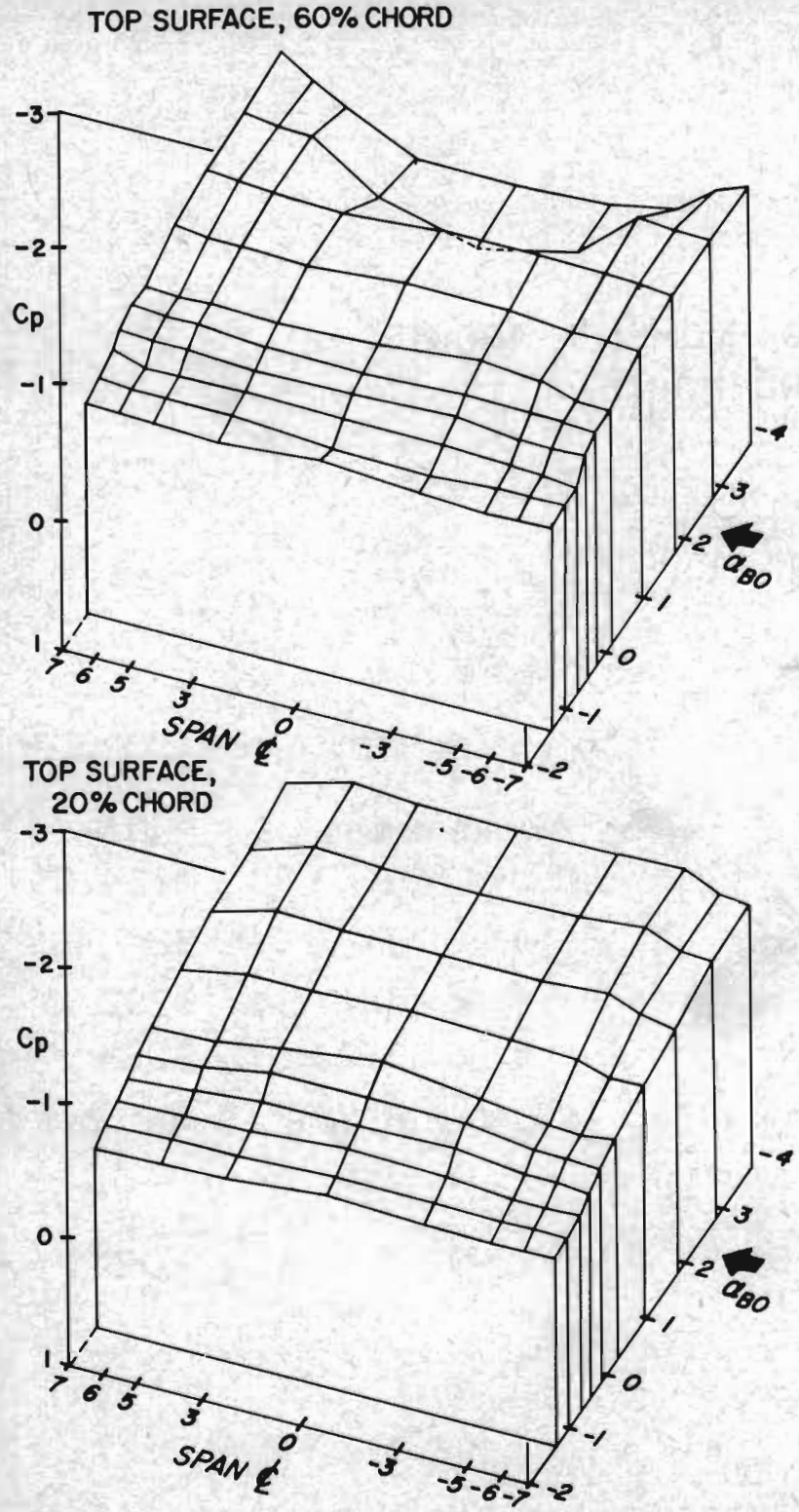

INDICATORS OF FLOW TWO-DIMENSIONALITY: PRESSURE COEFFICIENTS ACROSS THE SPAN OF A SUPERCRITICAL AEROFOIL, AT $M_\infty \cong 0.84$, $x/c = 0.20$ AND 0.60

SCAN	1	2	3	4	5	6
α_w°	−4·32	−2·28	0·40	2·33	4·45	6·46
C_{ND}	−0·28	0.089	0·455	0·864	1·093	1·003

FIG 7·2

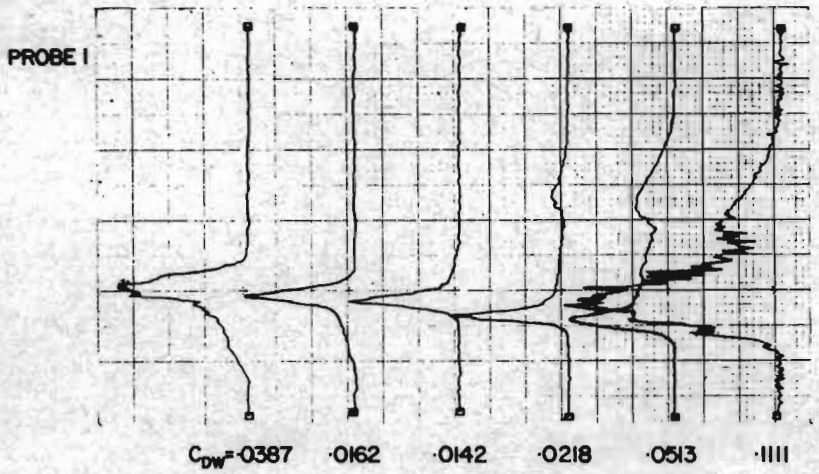

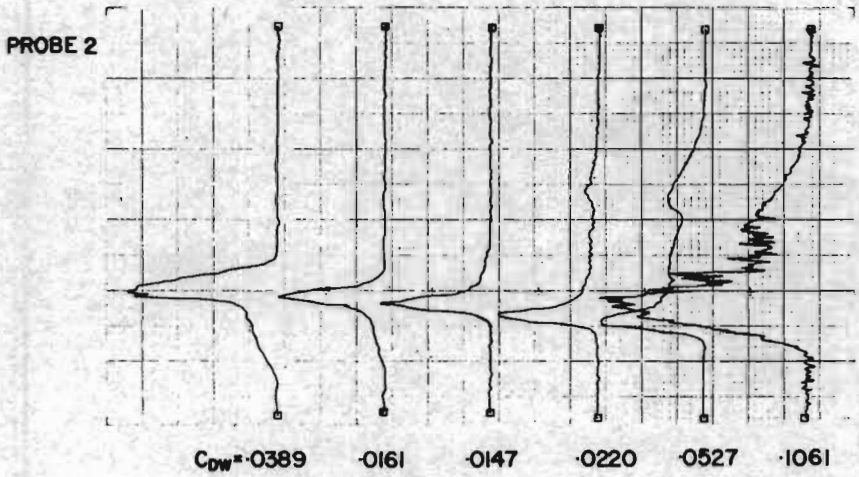

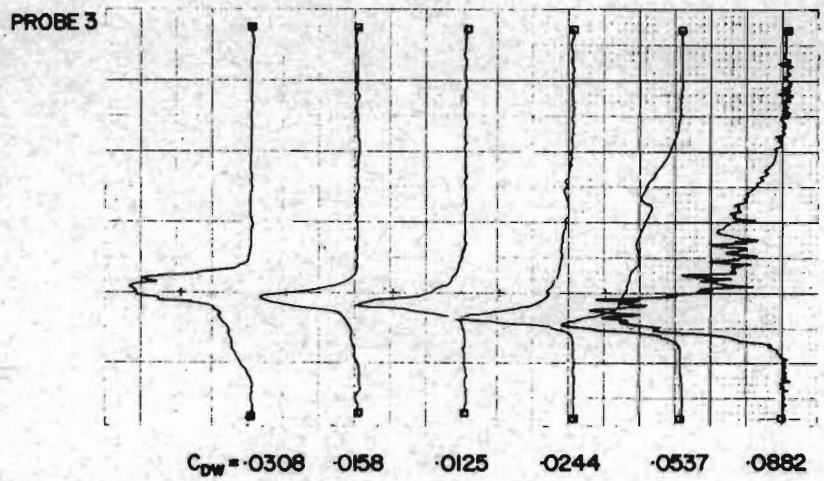

RUN 3350, C_μ=0; θ_j=120°; WAKES MEASURED AT ONE CHORD DOWNSTREAM OF T.E

INDICATORS OF FLOW TWO-DIMENSIONALITY:– PROFILES OF PITOT PRESSURE DEFICIT IN WAKE BEHIND AEROFOIL I AT $M_\infty \cong 0.8$

FIG. 8

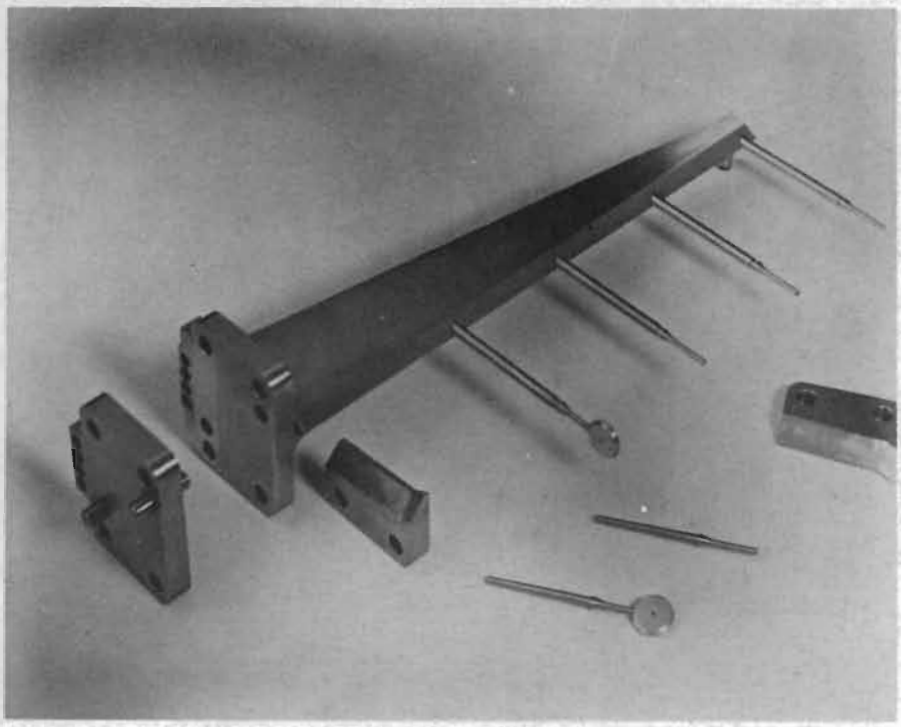

WAKE RAKE WITH DISC PROBE
AT POSITION 4

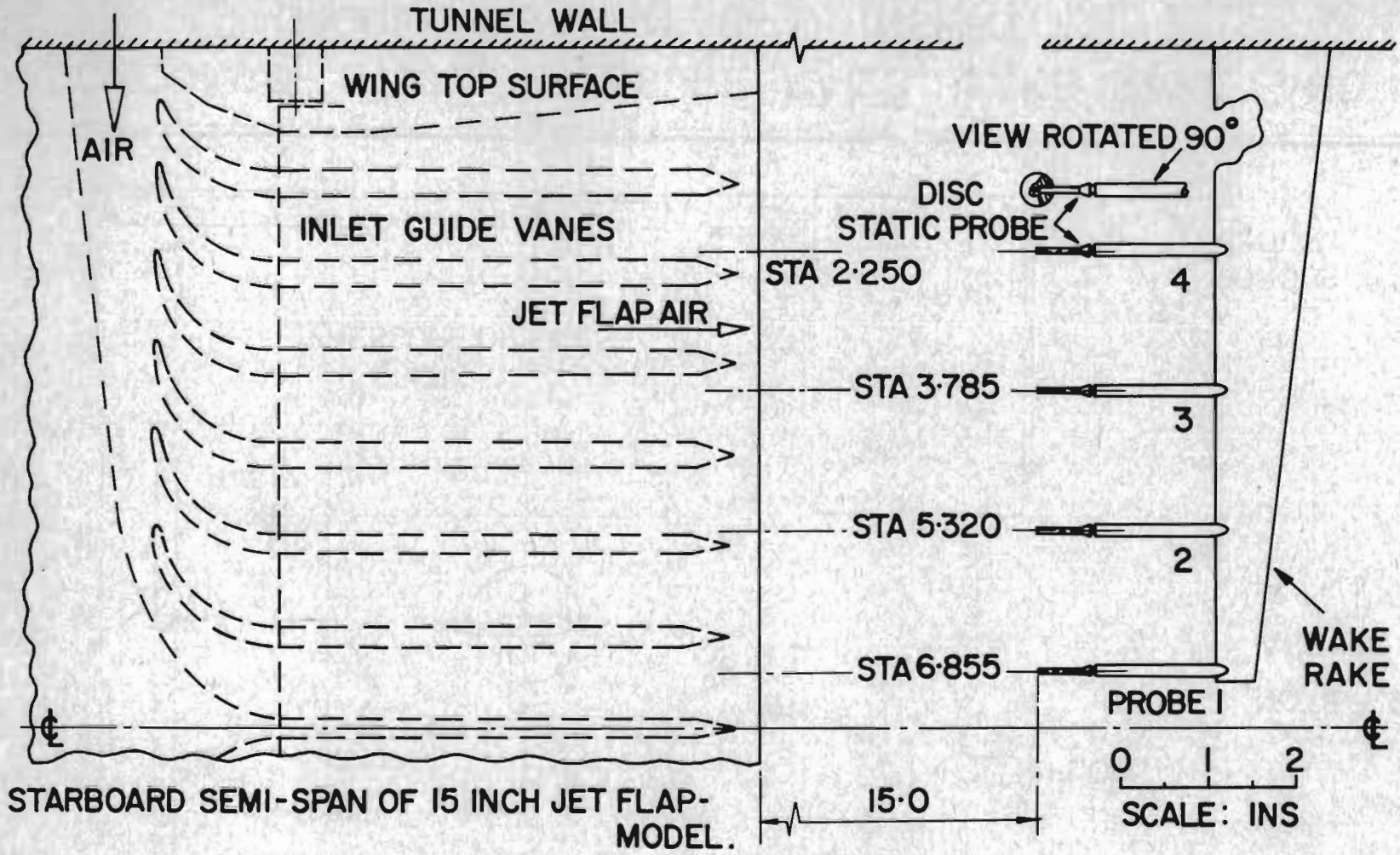

FIG. 9

LOCATION OF WAKE RAKE WITH RESPECT TO MODEL WING

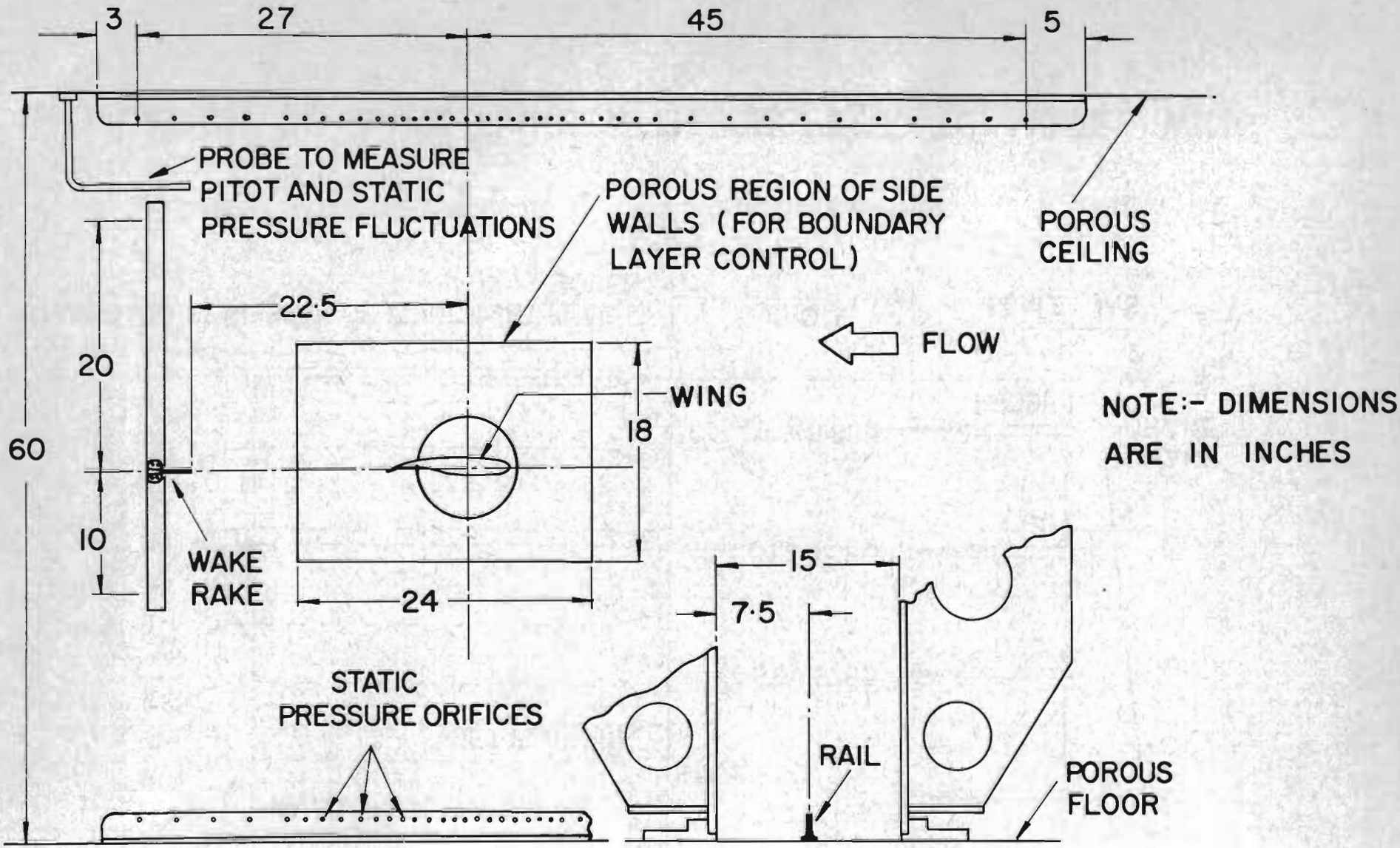

LOCATION OF STATIC PRESSURE RAILS, WAKE RAKE AND MODEL WING IN 2-D INSERT

FIG. 10

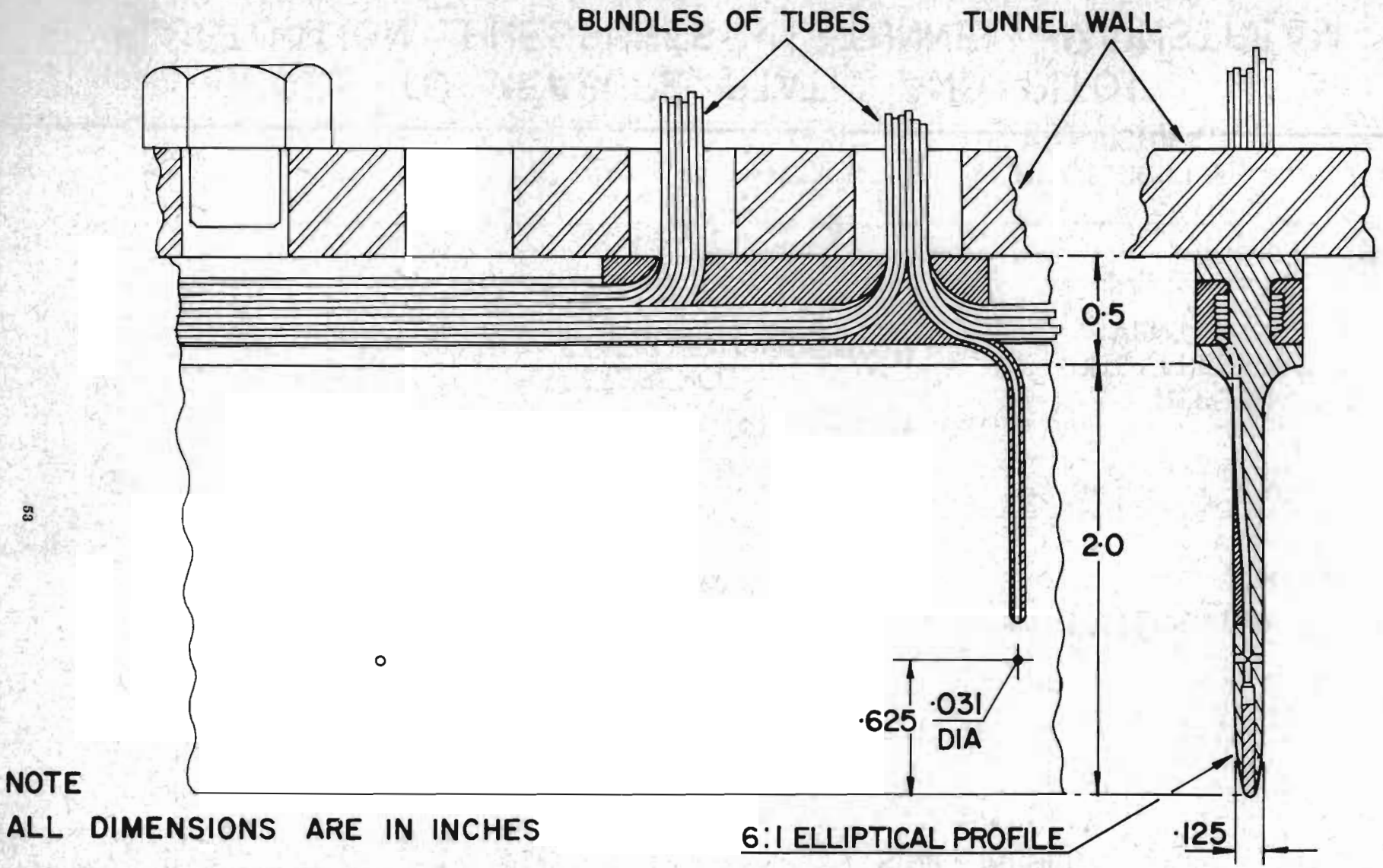

DETAILS OF STATIC PRESSURE RAILS

FIG. 11

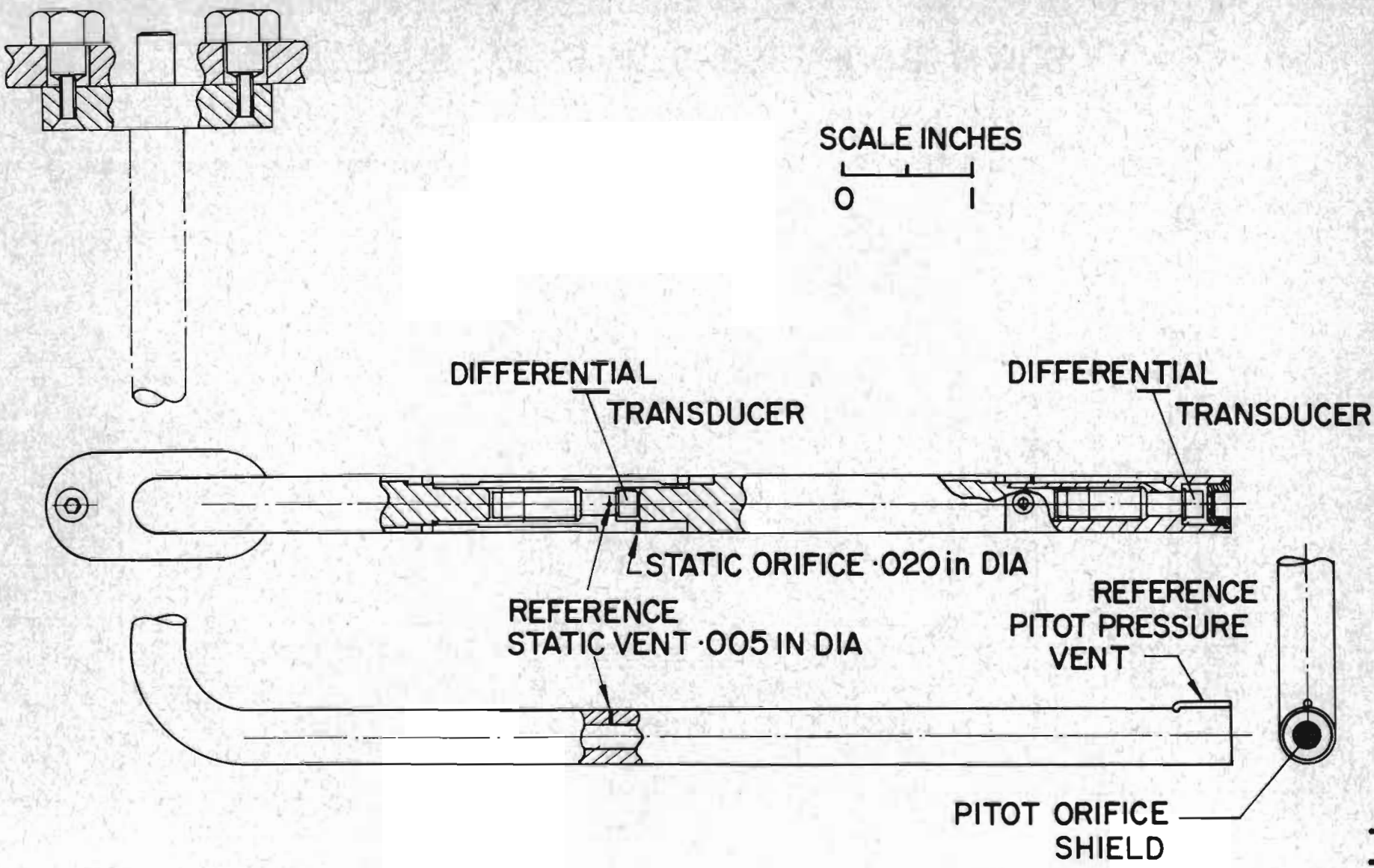

PROBE TO MEASURE STATIC AND PITOT FLUCTUATION PRESSURES IN TUNNEL MAINSTREAM

FIG 12

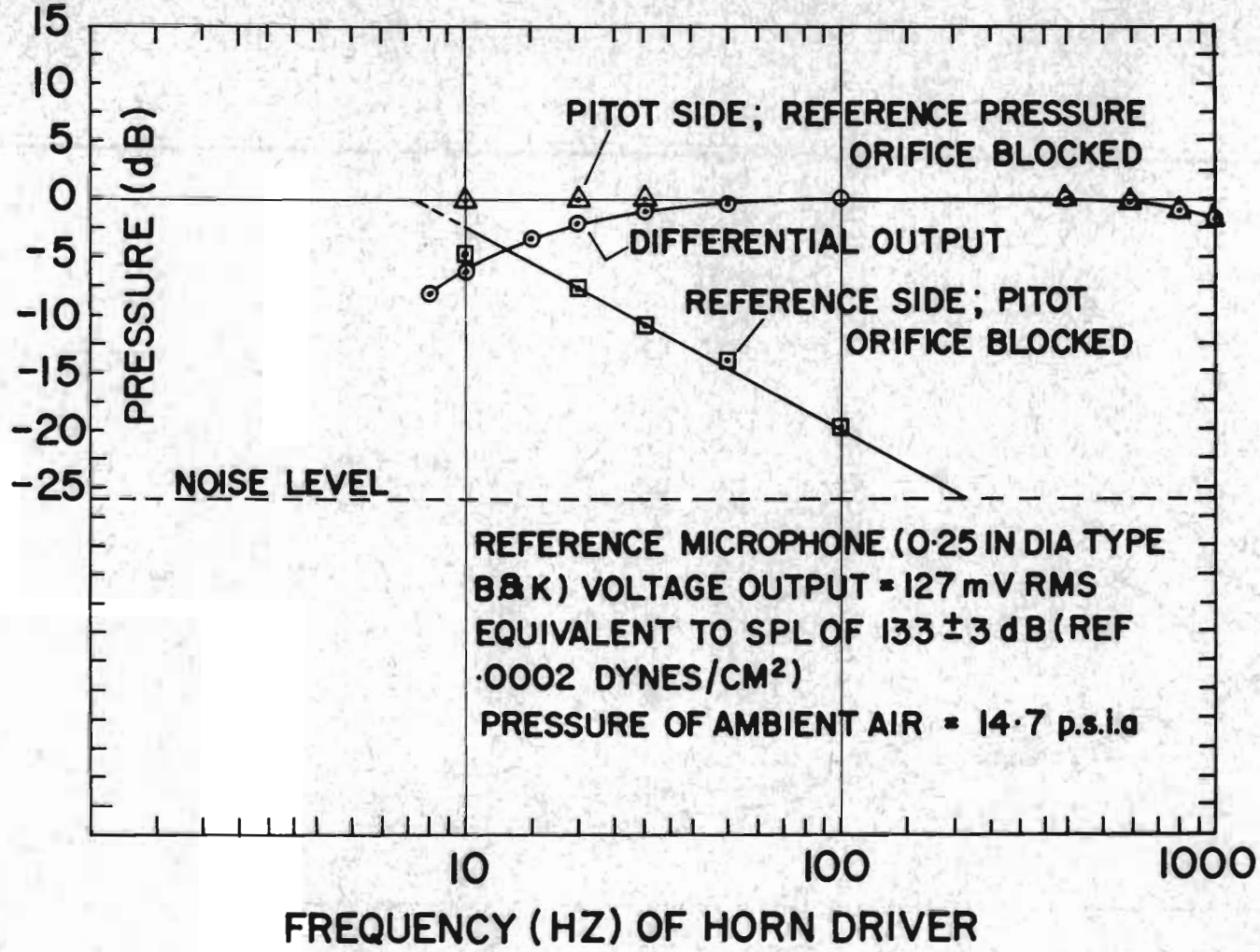

FREQUENCY RESPONCE OF FLUCTUATION PITOT PRESSURE TRANSDUCER

FIG. 13

FIG. 14.1

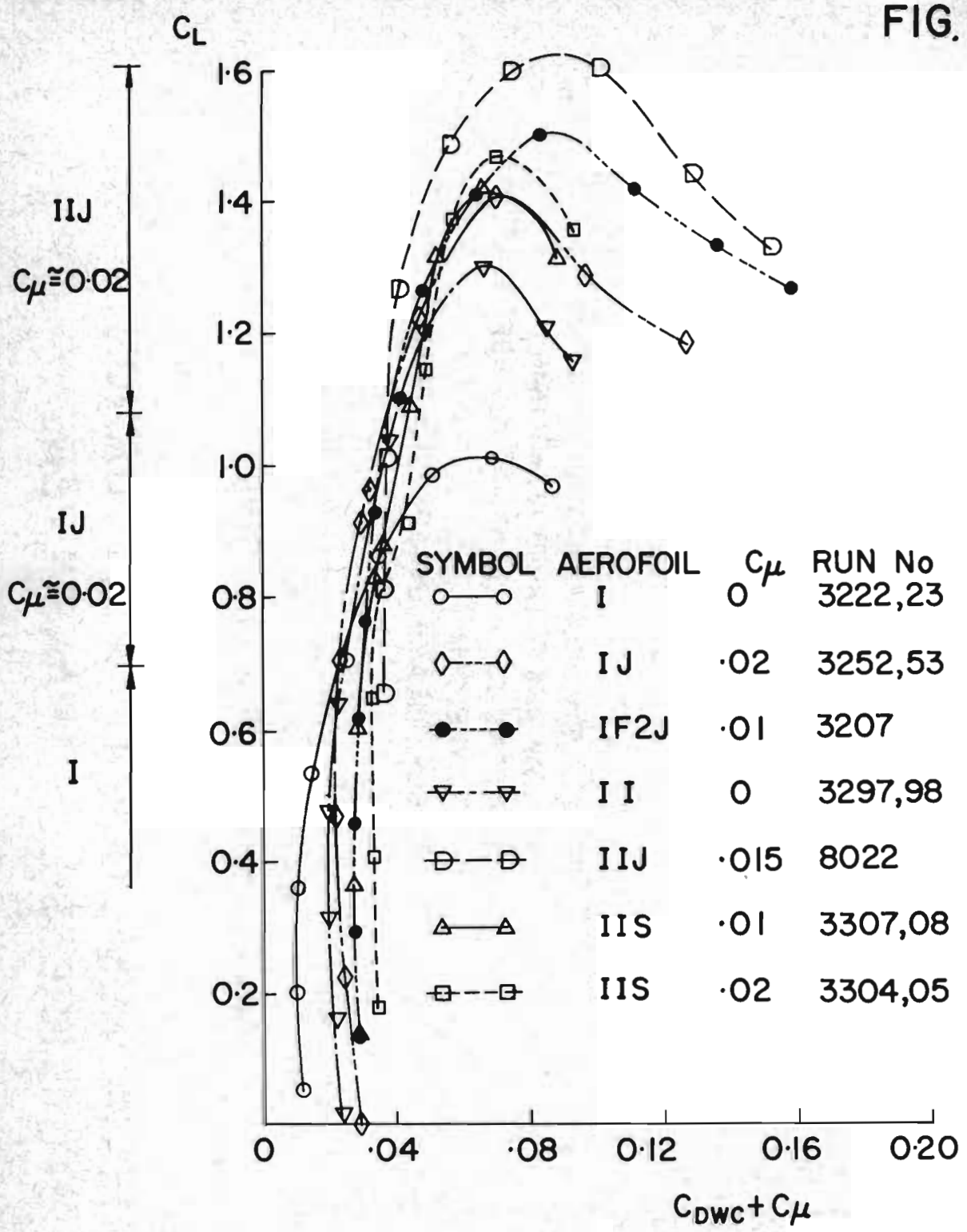

LIFT / DRAG POLARS FOR AEROFOILS I AND II AT $M_\infty \cong 0.75$

FIG. 14.2

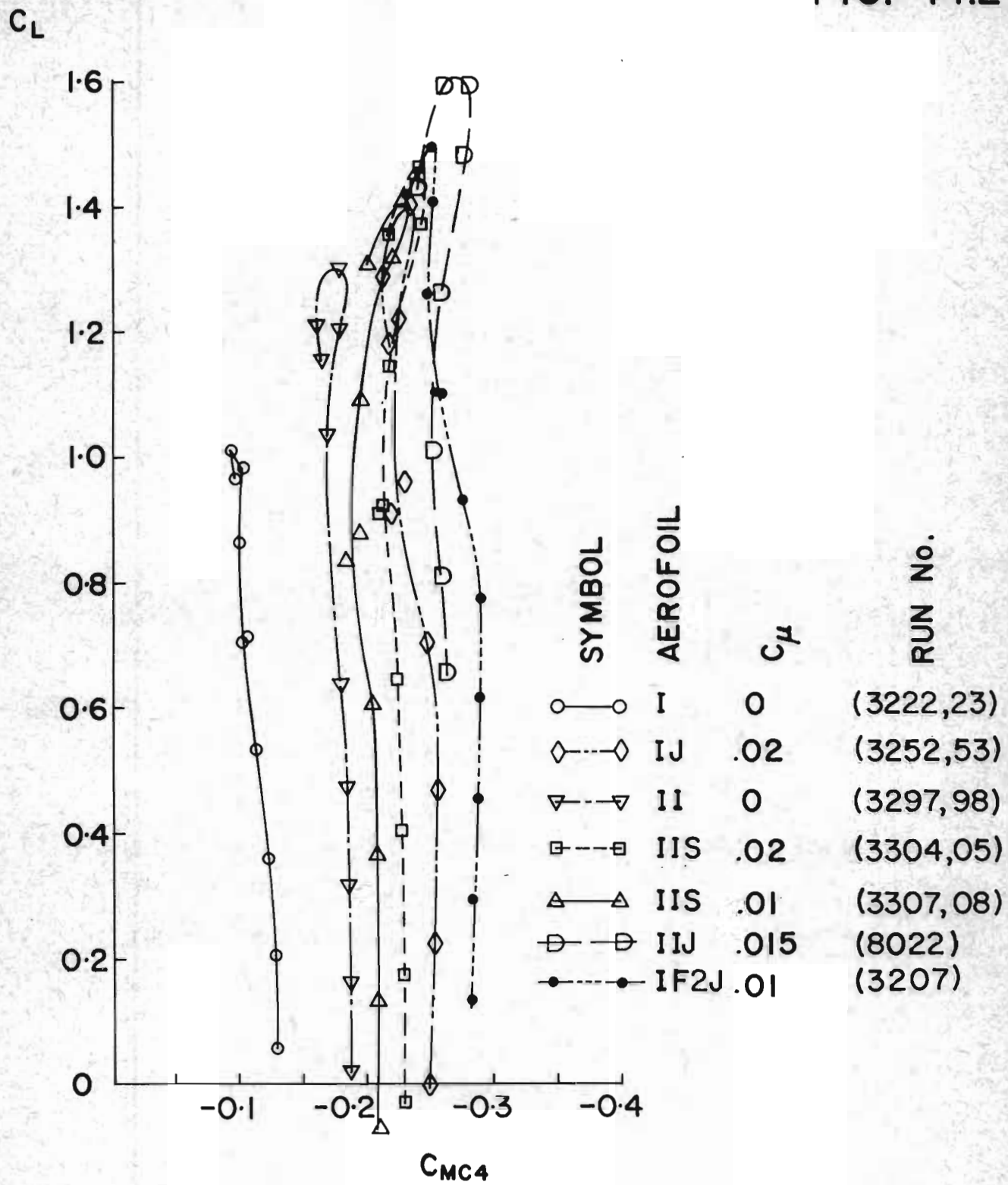

LIFT / PITCHING MOMENT PLOTS FOR AEROFOILS I AND II AT $M_\infty \cong 0.75$

FIG. 15.1

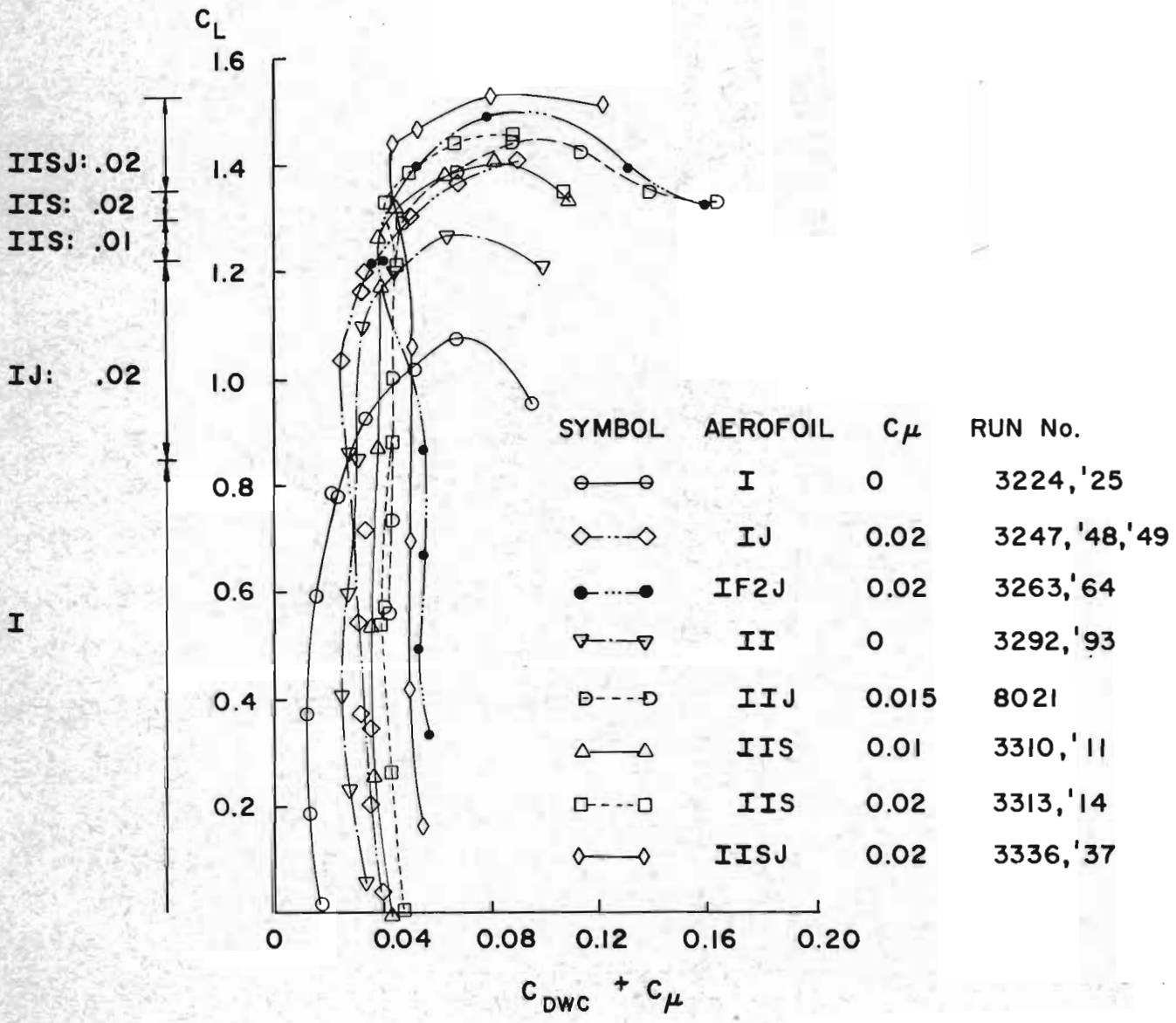

LIFT/ DRAG POLARS FOR AEROFOILS I AND II
AT $M_\infty \cong 0.80$

FIG. 15.2

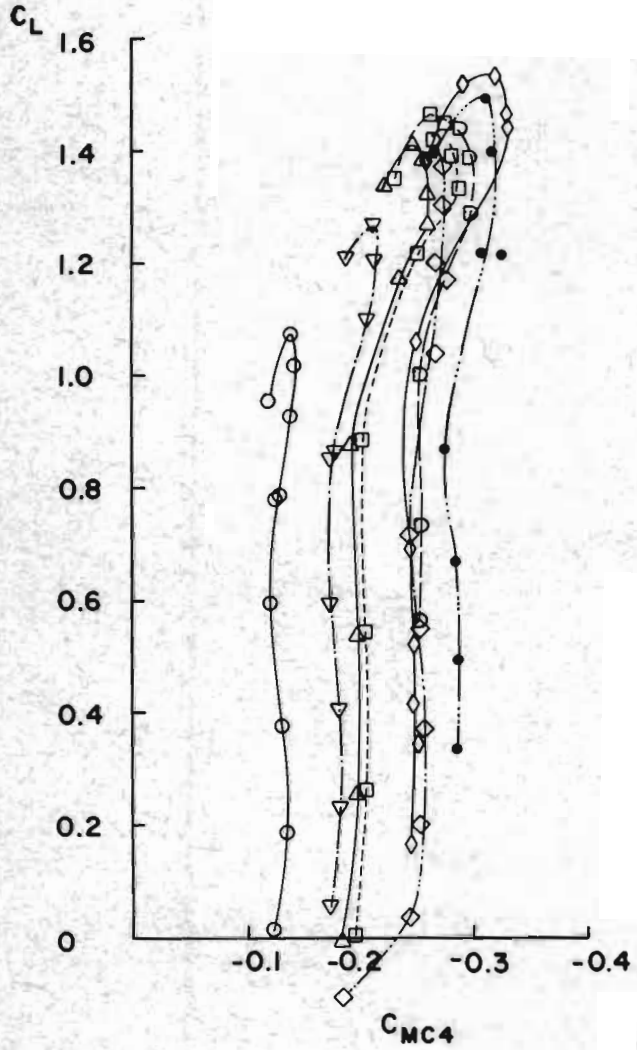

SYMBOL	AEROFOIL	C_μ	RUN No.
	I	0	3224,'25
	IJ	0.02	3247,'48,'49
	II	0	3292,'93
	IIS	0.02	3313,'14
	IIS	0.01	3310,'11
	IISJ	0.02	3336,'37
	IF2J	0.02	3263,'64
	IIJ	0.015	3021

LIFT/ PITCHING MOMENT PLOTS FOR AEROFOILS I AND II AT $M_\infty \cong 0.80$

FIG. 16.1

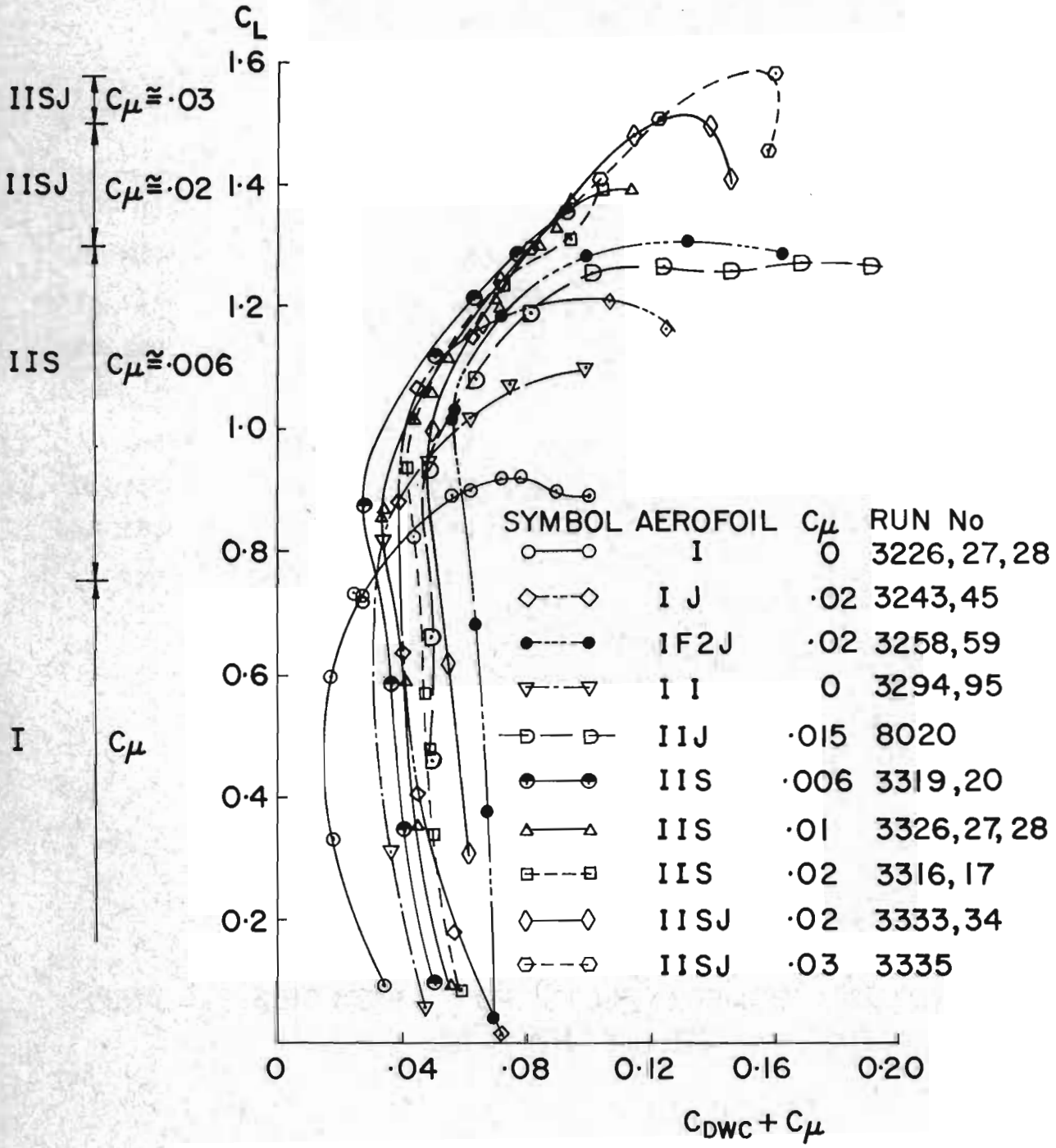

LIFT / DRAG POLARS FOR AEROFOILS I AND II AT $M_\infty \cong 0.85$

FIG. 16.2

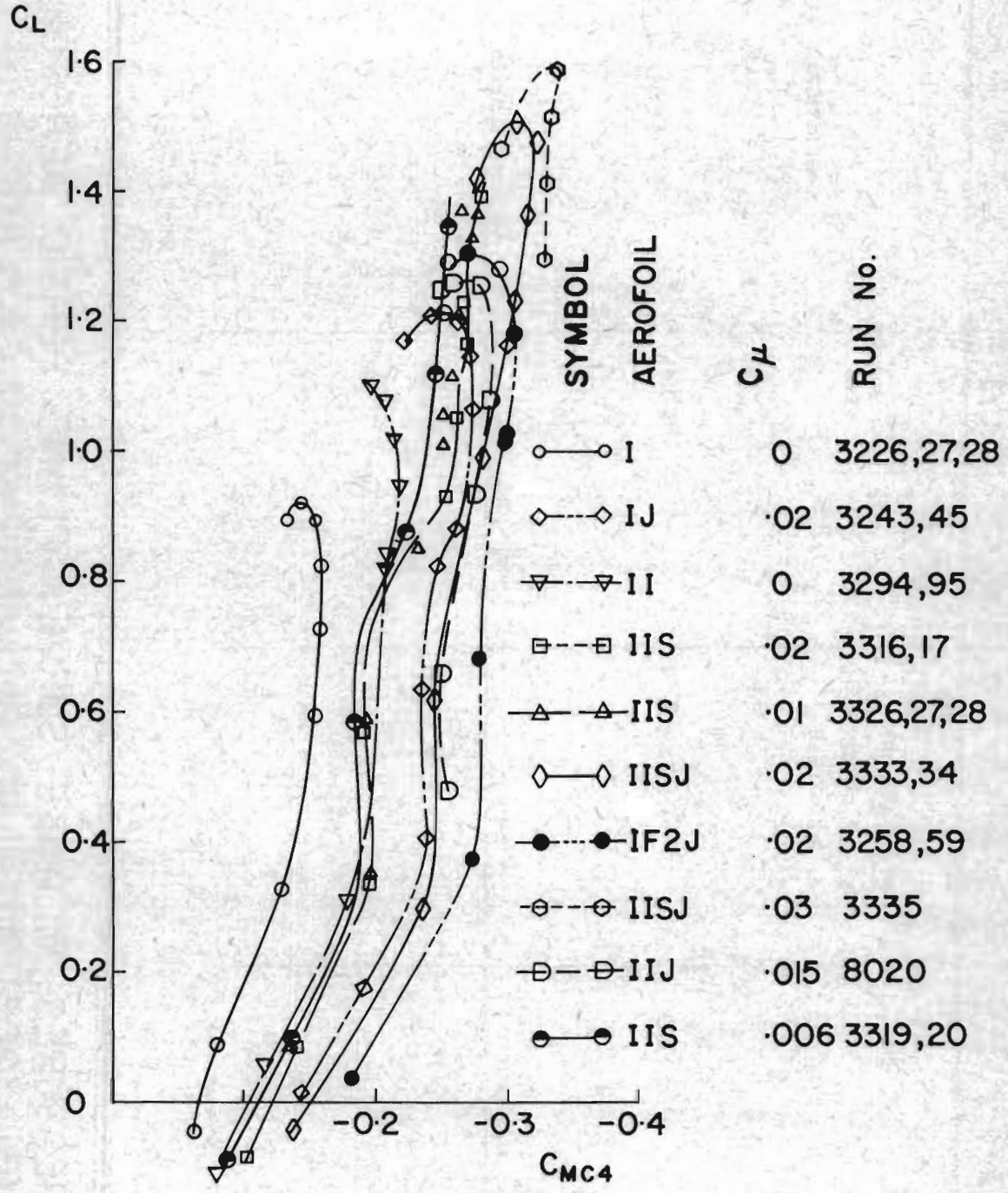

LIFT / PITCHING MOMENT PLOTS FOR AEROFOILS I AND II AT $M_\infty \cong 0.85$

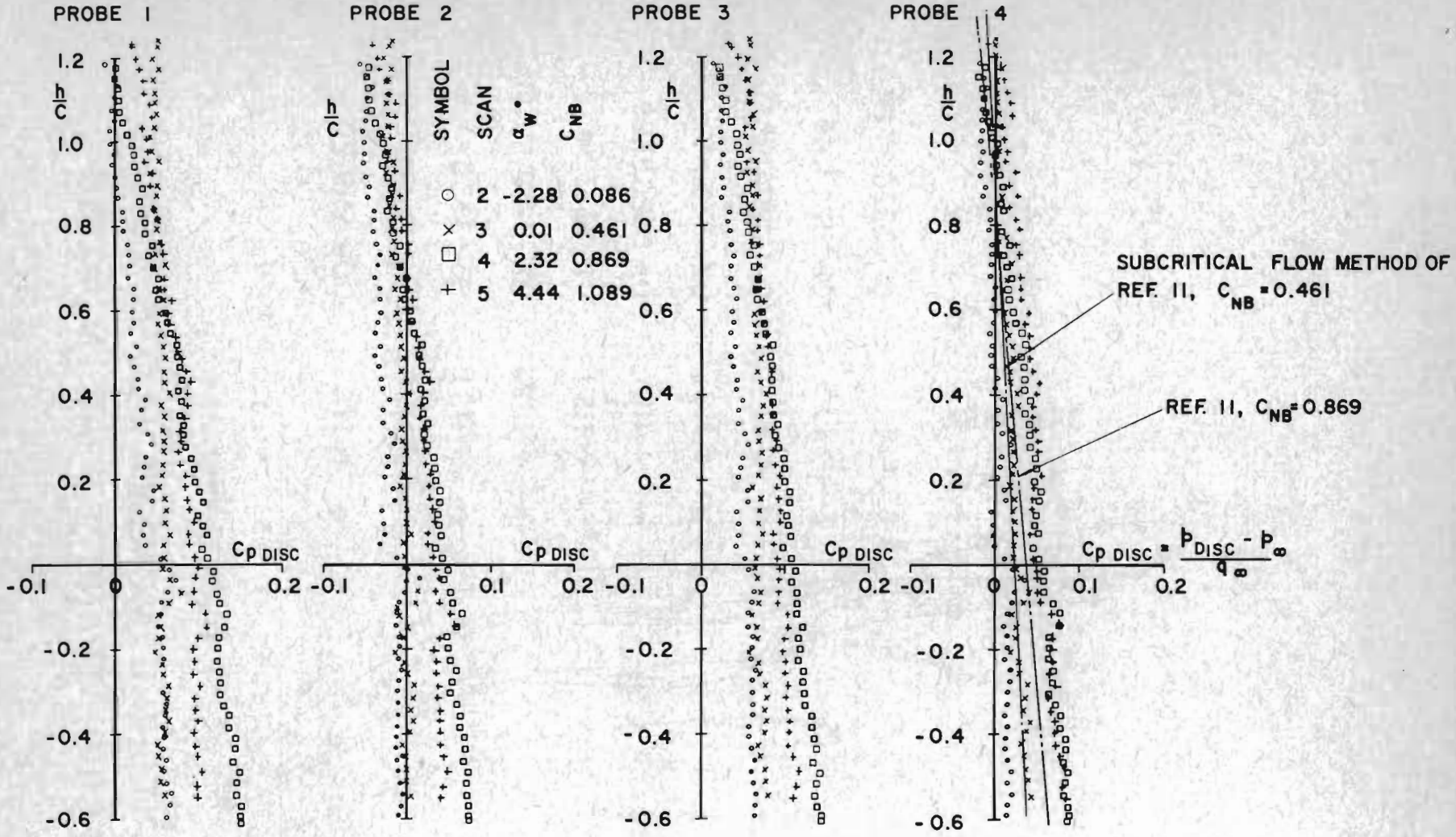

STATIC PRESSURES IN WAKE SURVEY PLANE BEHIND AEROFOIL I (θ_j = 120°) WITH NO BLOWING, AT $M_\infty \cong 0.80$

FIG. 171

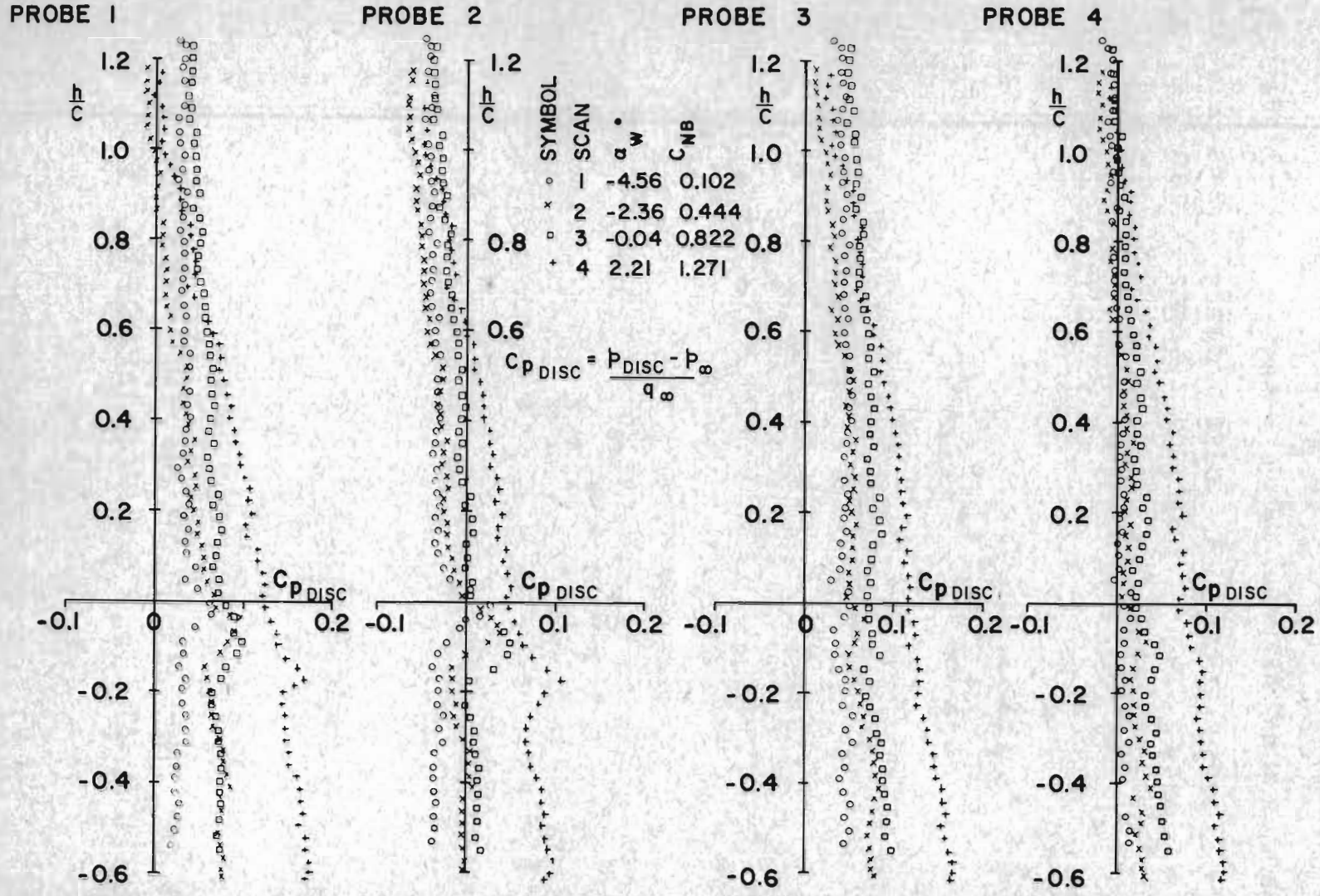

STATIC PRESSURES IN WAKE SURVEY PLANE BEHIND AEROFOIL IJ ($\theta \cong 120°$) WITH BLOWING AT $C_\mu = 0.02$, $M_\infty \cong 0.80$

FIG 172

FIG. 18

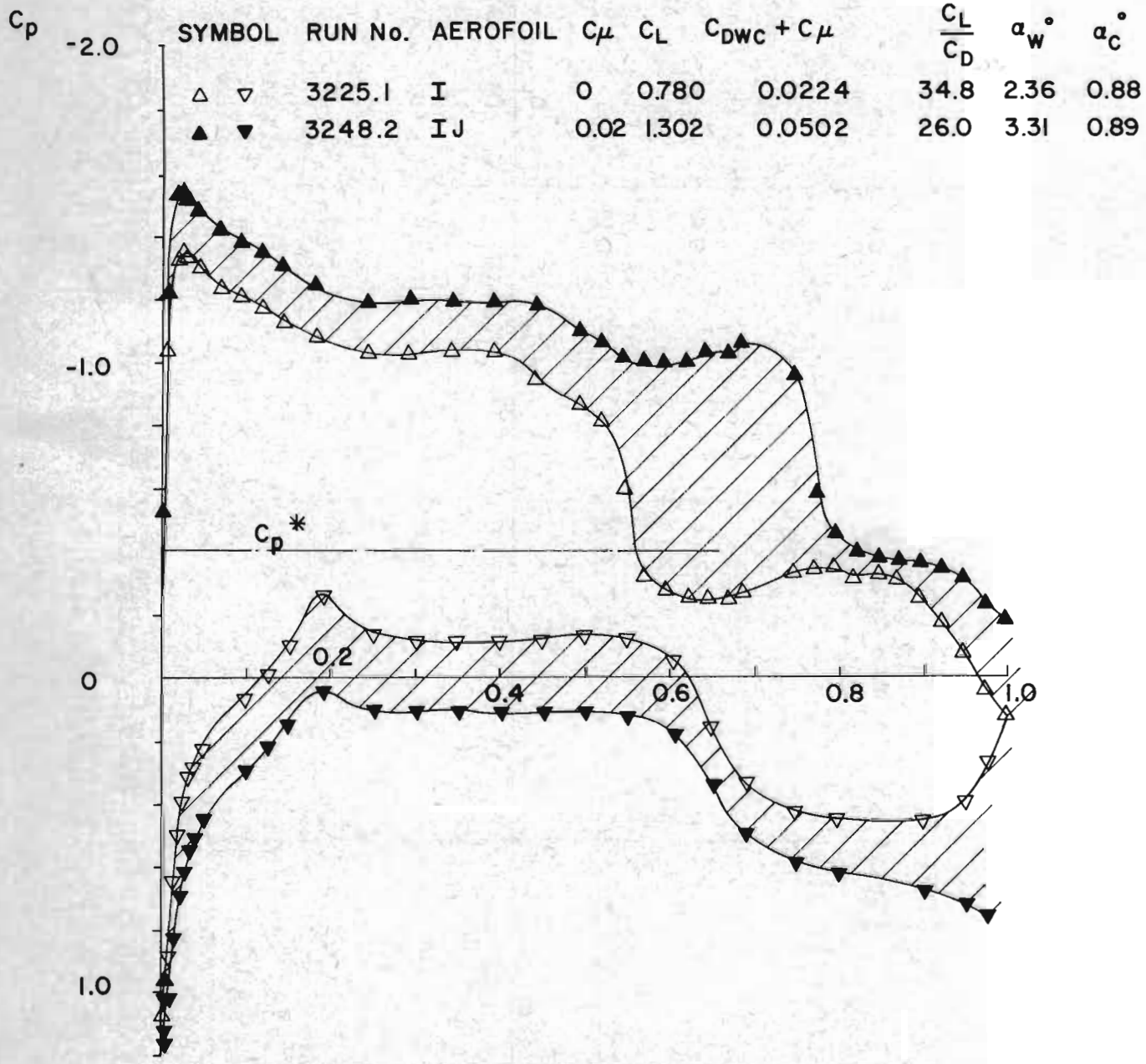

SYMBOL	RUN No.	AEROFOIL	$C\mu$	C_L	$C_{DWC} + C\mu$	$\frac{C_L}{C_D}$	α_w°	α_c°
△ ▽	3225.1	I	0	0.780	0.0224	34.8	2.36	0.88
▲ ▼	3248.2	IJ	0.02	1.302	0.0502	26.0	3.31	0.89

EFFECT OF THE JET FLAP ON THE PRESSURE DISTRIBUTION AT $M_\infty \cong 0.8$ FOR AEROFOIL I

FIG. 19

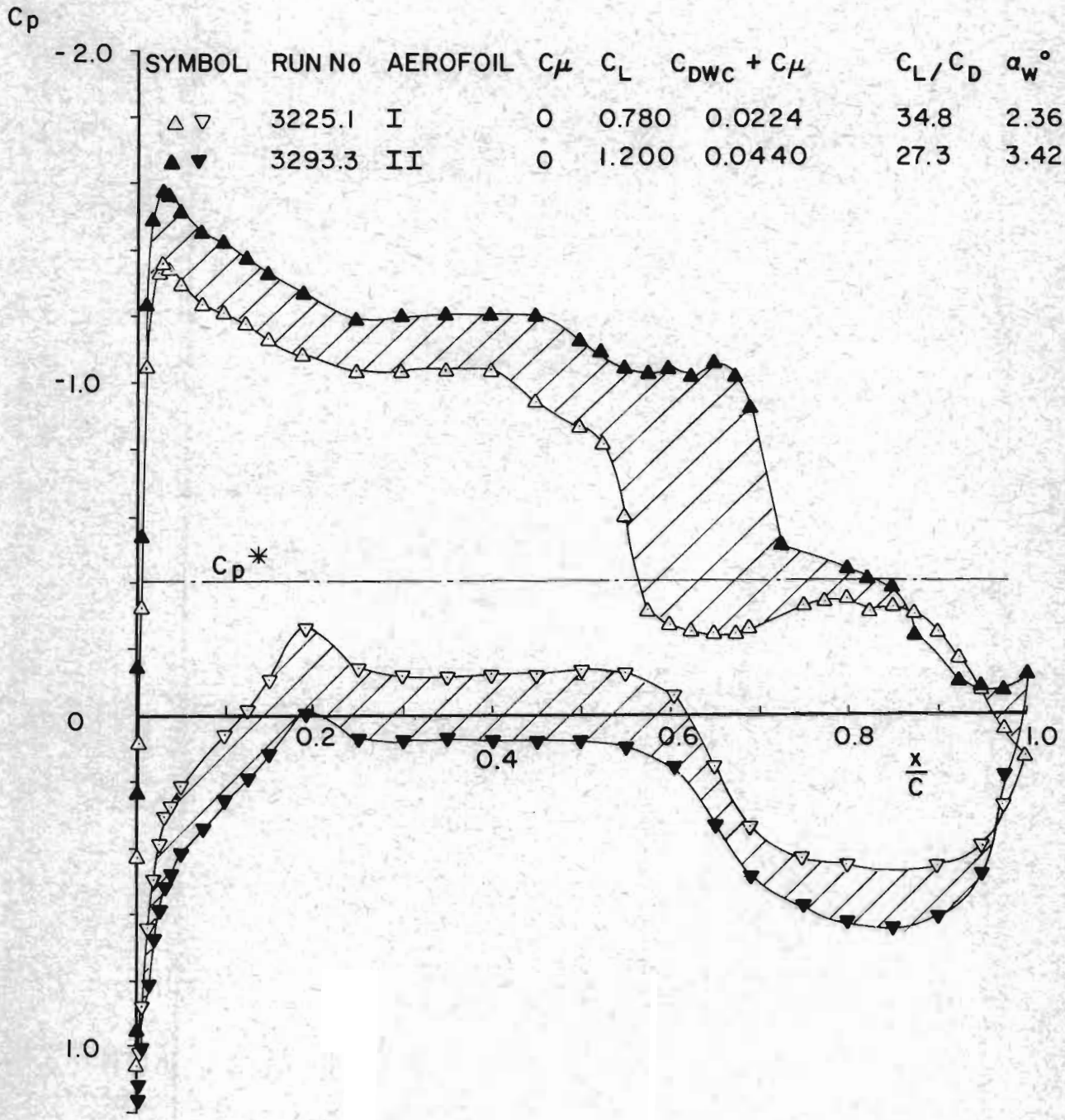

SYMBOL	RUN No	AEROFOIL	C_μ	C_L	$C_{DWC} + C_\mu$	C_L/C_D	$\alpha_w°$	$\alpha_c°$
△ ▽	3225.1	I	0	0.780	0.0224	34.8	2.36	0.88
▲ ▼	3293.3	II	0	1.200	0.0440	27.3	3.42	1.22

EFFECT OF AFT CAMBER ALONE ON THE PRESSURE DISTRIBUTION AT $M_\infty \cong 0.8$

FIG. 20

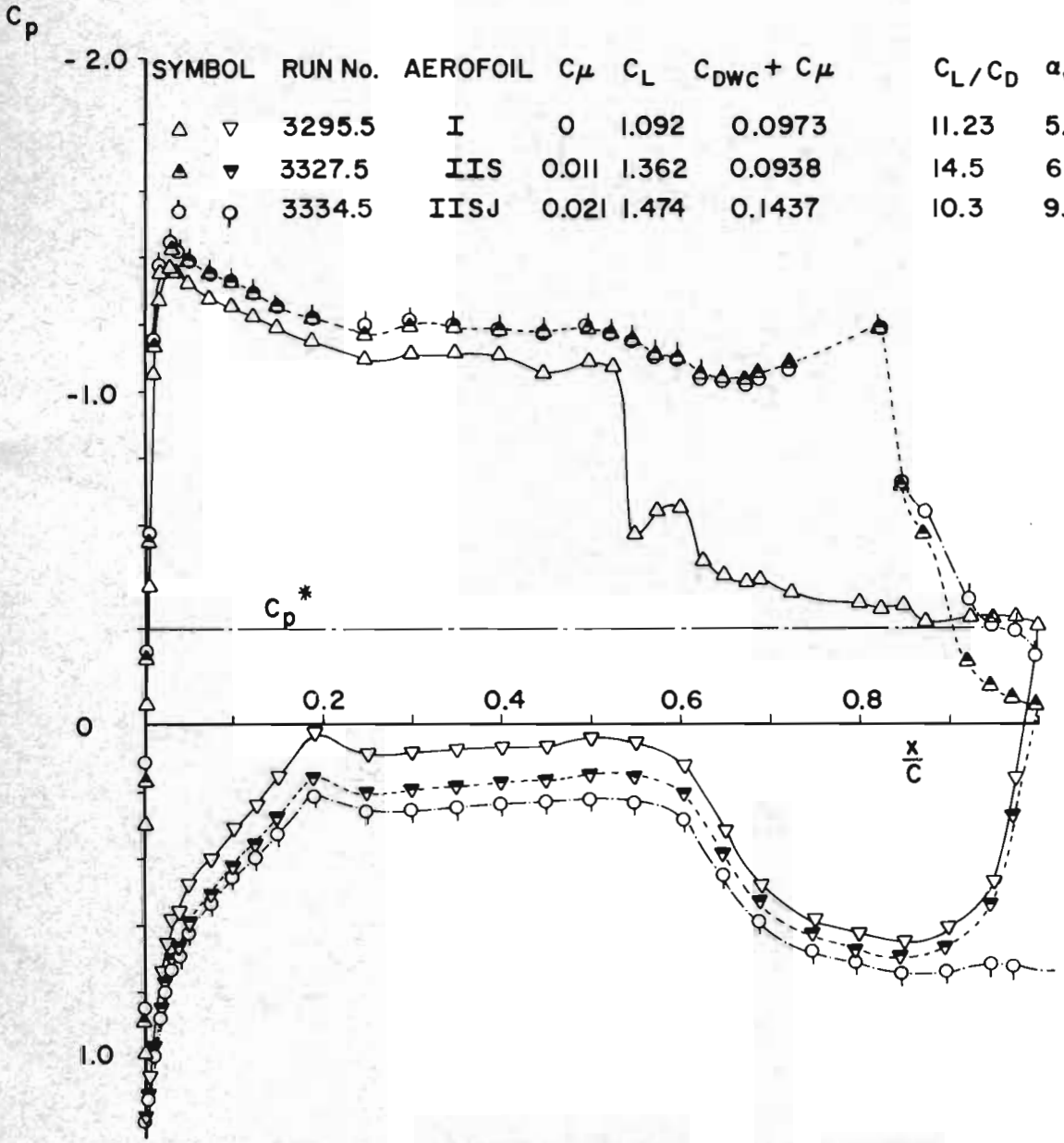

SYMBOL	RUN No.	AEROFOIL	C_μ	C_L	$C_{DWC} + C_\mu$	C_L / C_D	$\alpha_w^\bullet$	$\alpha_c^\bullet$
△ ▽	3295.5	I	0	1.092	0.0973	11.23	5.38	2.98
▲ ▼	3327.5	IIS	0.011	1.362	0.0938	14.5	6.34	3.34
○ ♀	3334.5	IISJ	0.021	1.474	0.1437	10.3	9.38	3.03

EFFECT OF SLOT BLOWING IN COMBINATION WITH THE JET FLAP ON AEROFOIL II AT $M_\infty \cong 0.85$

FIG 21

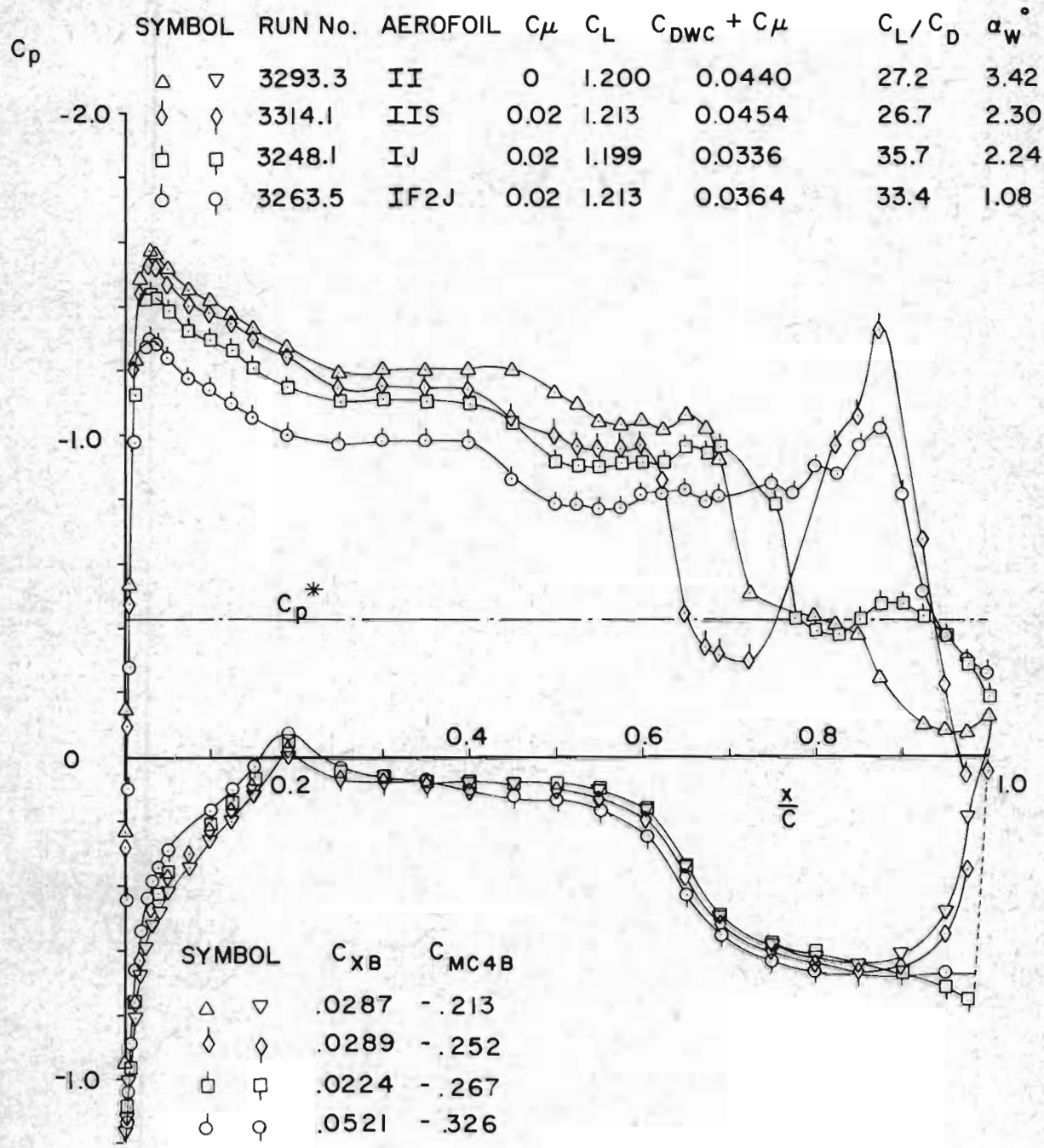

EFFECT OF CONFIGERATION CHANGE ON DRAG AT CONSTANT LIFT $C_L = 1.2$, AT $M_\infty \cong 0.8$

FIG. 22

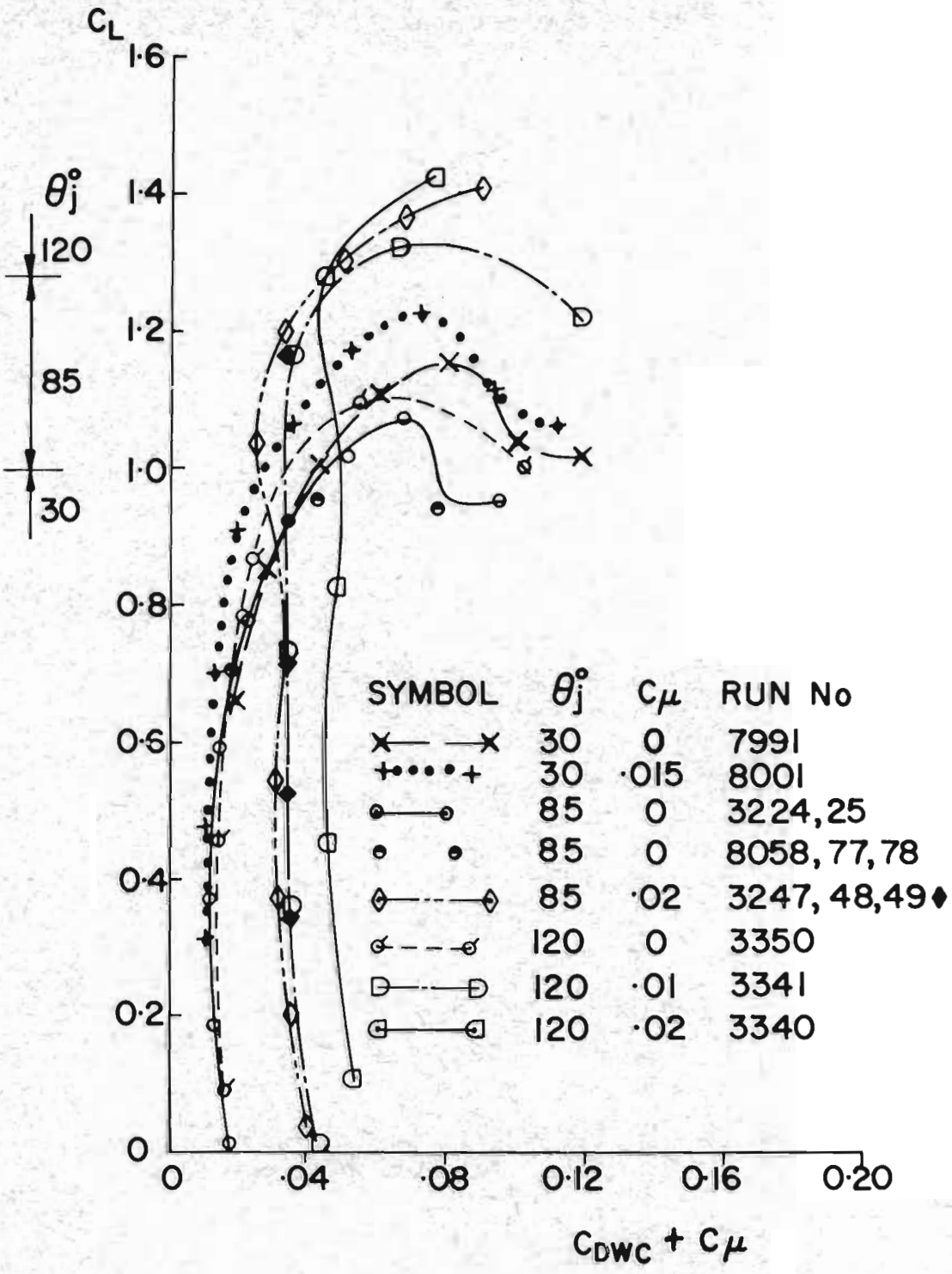

EFFECT OF CHANGING JET FLAP ANGLE, θ_j, ON AEROFOIL I AT $M_\infty \cong 0.8$

FIG. 23·1

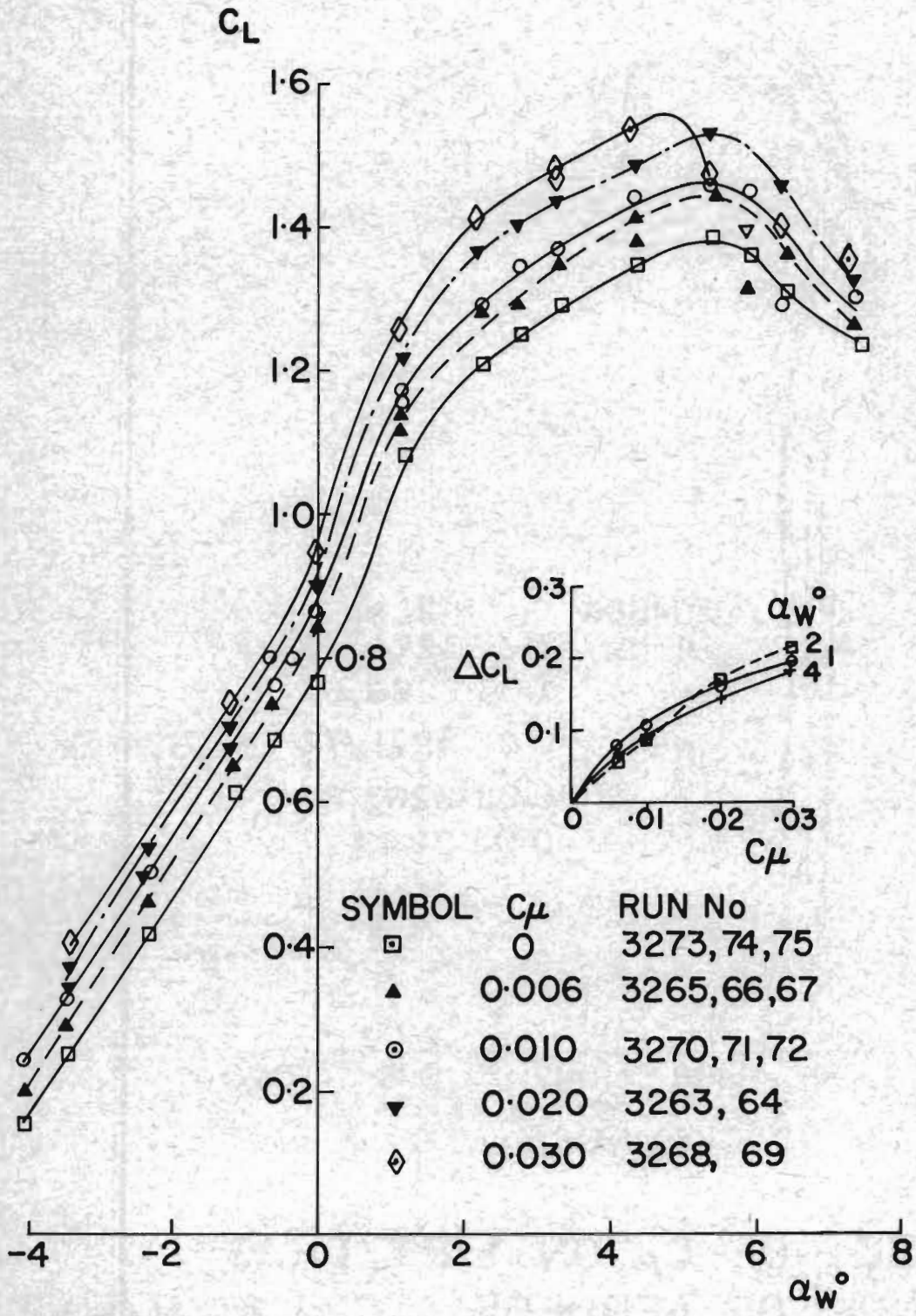

EFFECT OF $C\mu$ ON LIFT PERFORMANCE OF AEROFOIL IF2J AT $M_\infty \cong 0·8$

FIG.23.2

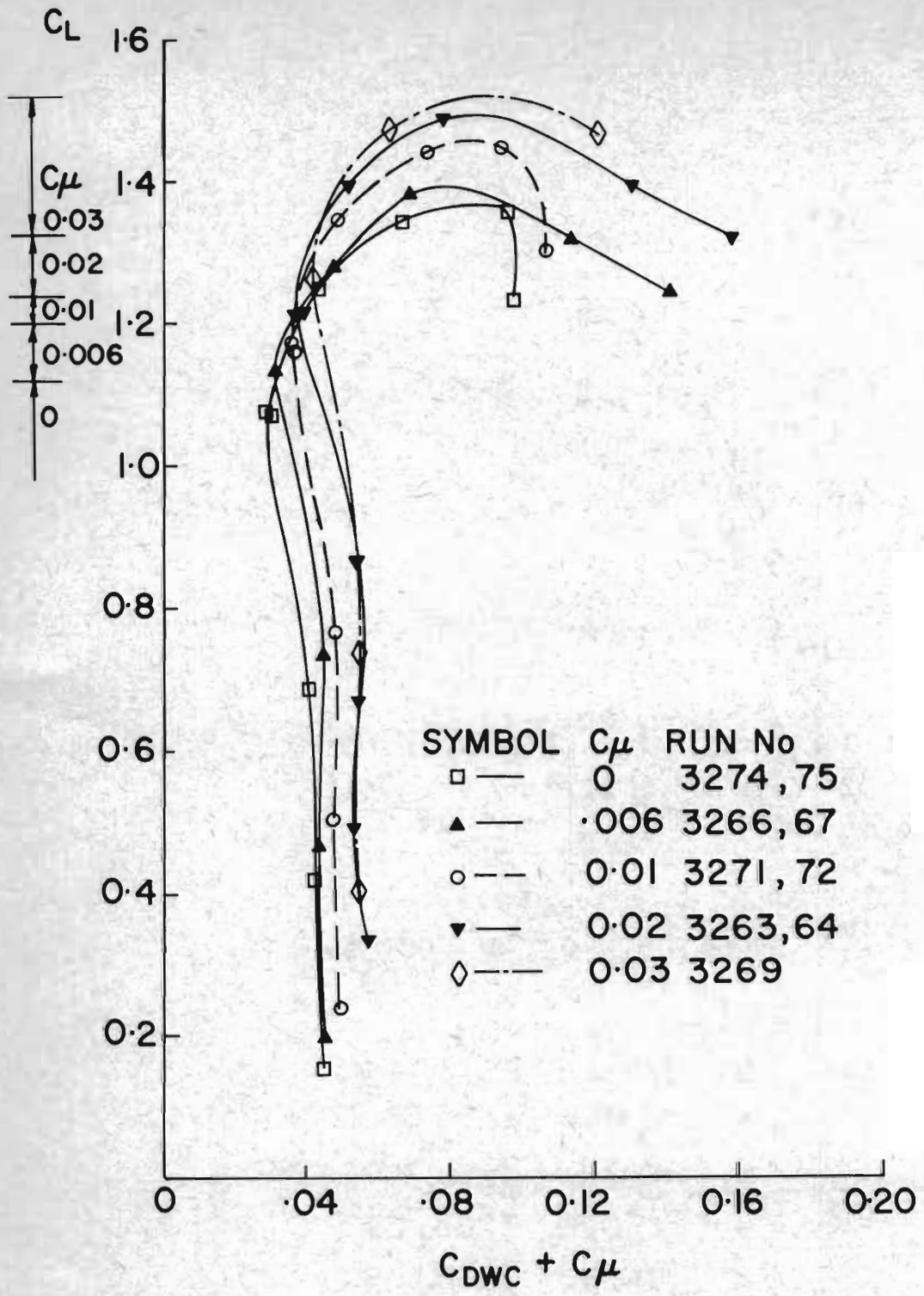

EFFECT OF $C\mu$ ON LIFT/DRAG PERFORMANCE OF AEROFOIL IF2J AT $M_\infty \cong 0.8$

FIG. 23.3

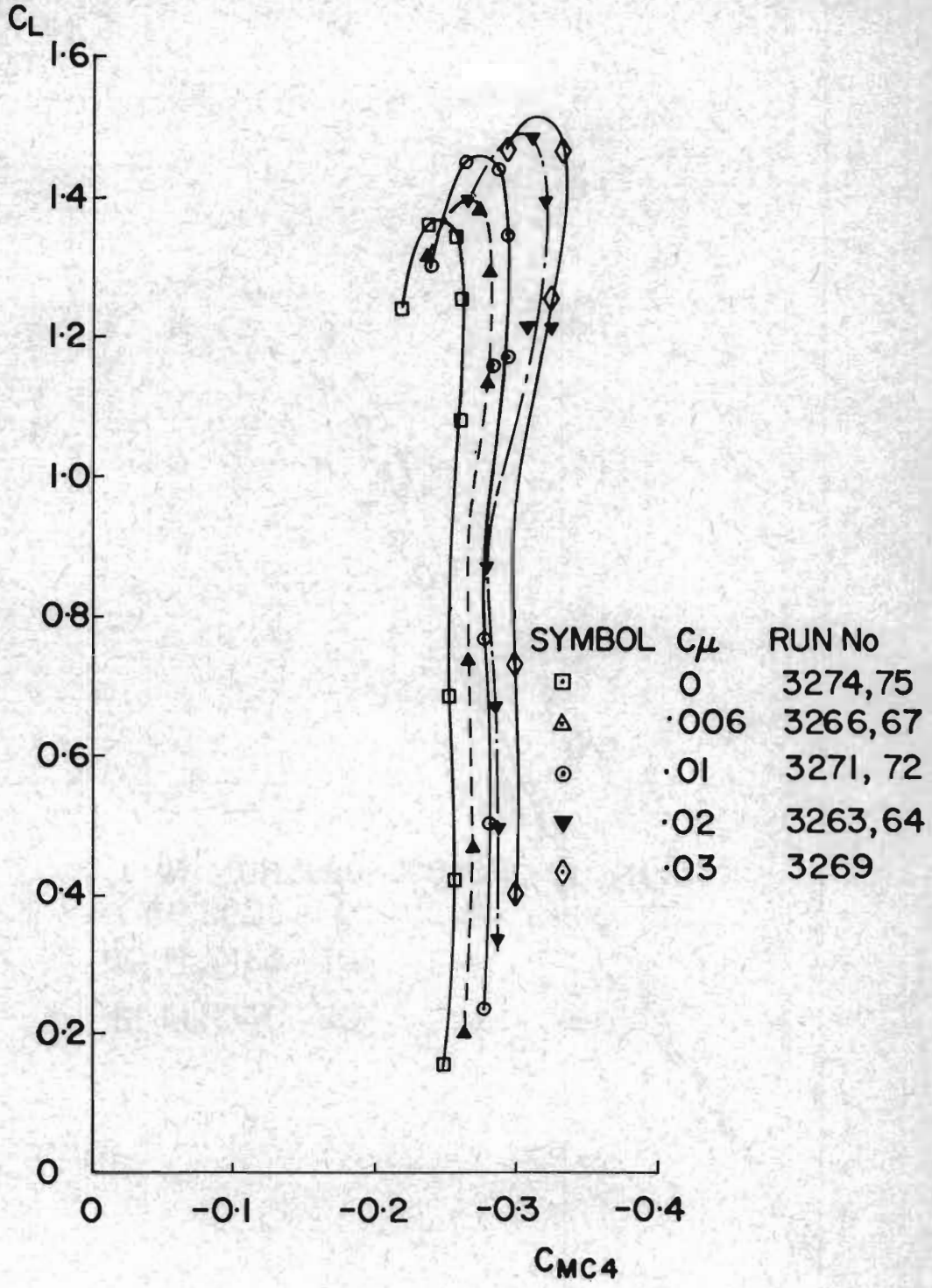

EFFECT OF C_μ ON LIFT/PITCHING MOMENT PERFORMANCE OF AEROFOIL IF2J AT $M_\infty \cong 0.8$

FIG. 24·1

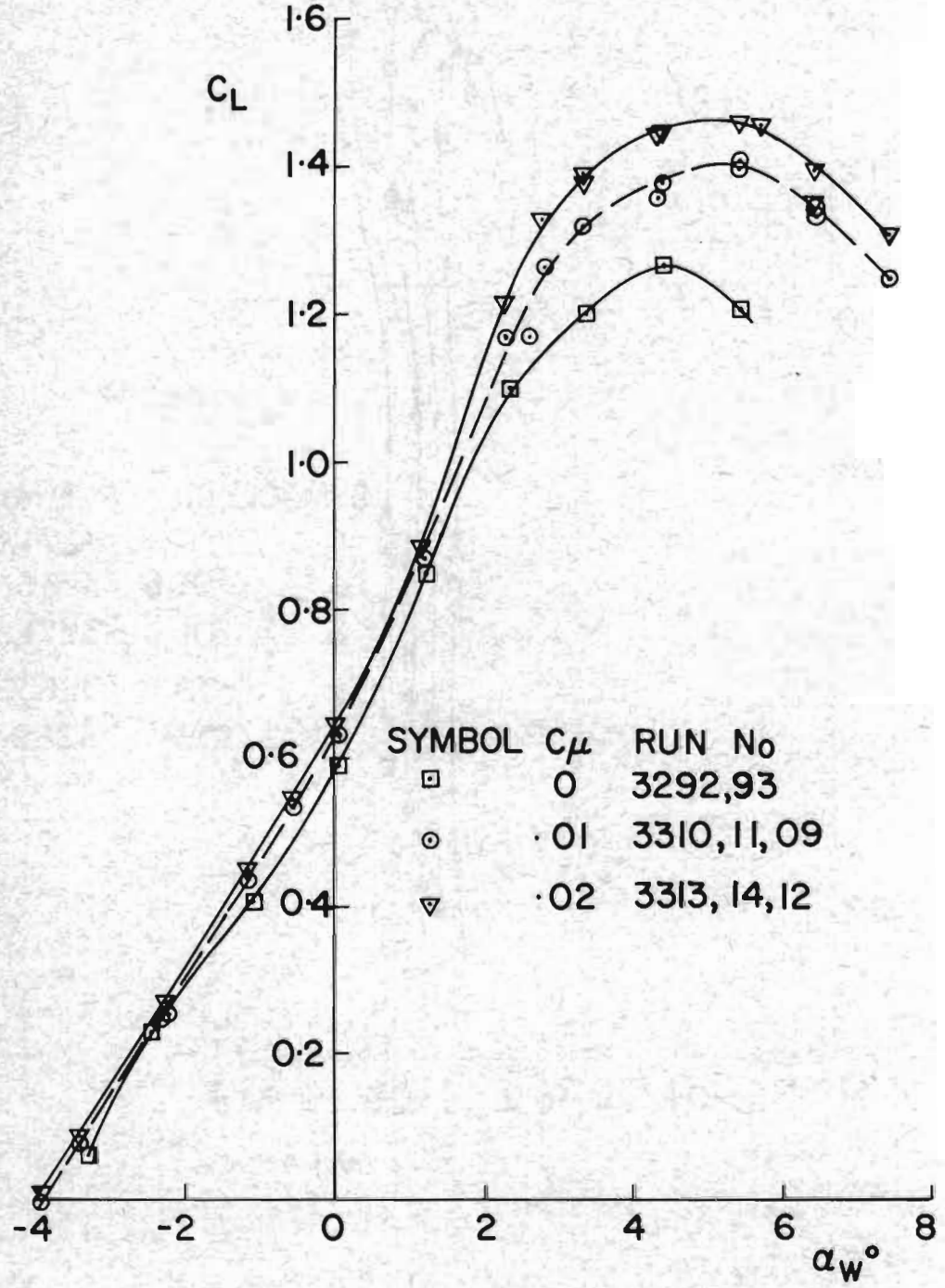

EFFECT OF Cμ ON LIFT PERFORMANCE OF AEROFOIL
I I S AT $M_\infty \cong 0·8$

FIG. 24.2

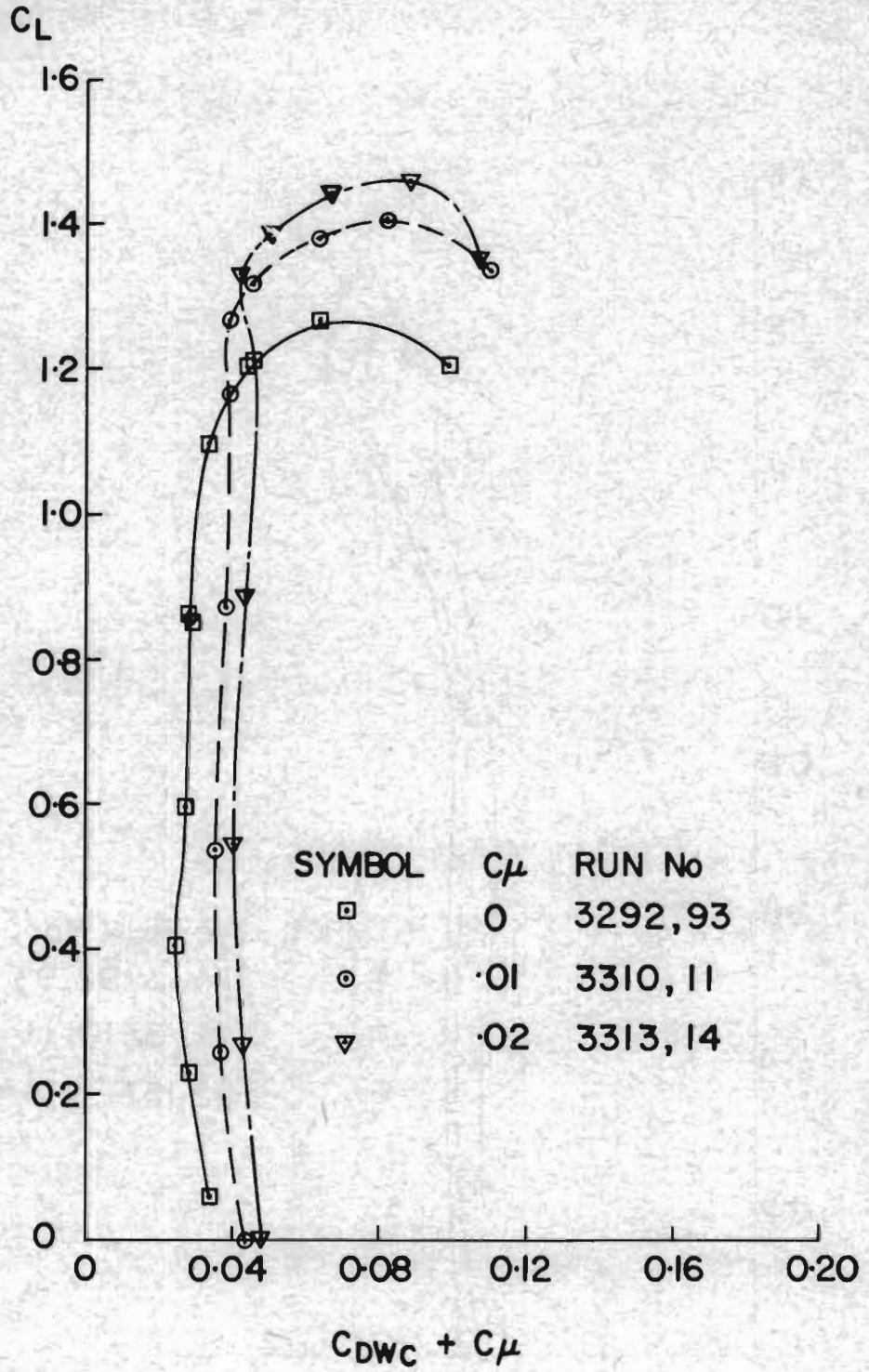

EFFECT OF C_μ ON LIFT/DRAG PERFORMANCE OF AEROFOIL IIS AT $M_\infty \cong 0.8$

FIG. 24·3

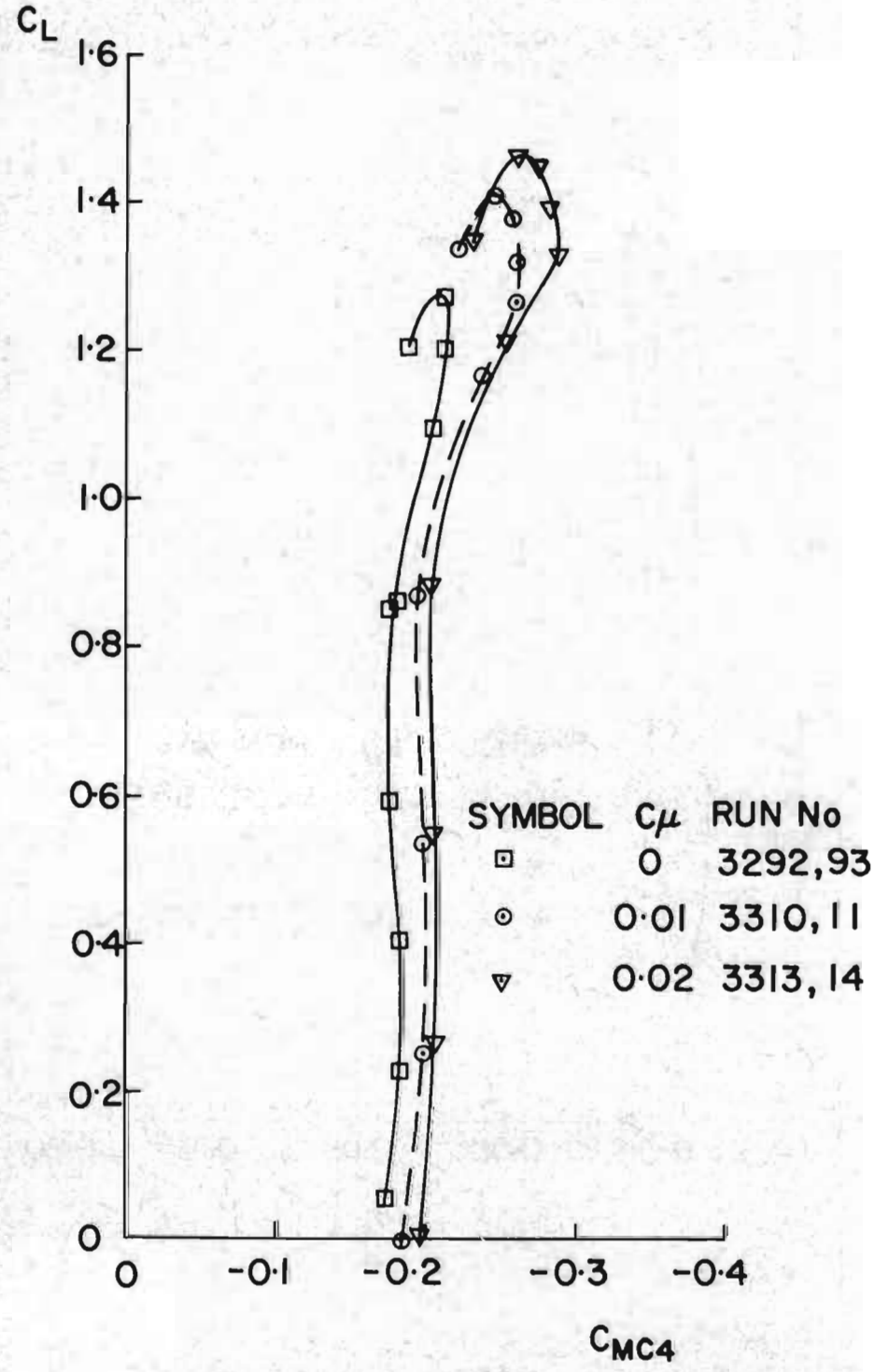

EFFECT OF C_μ ON LIFT/PITCHING MOMENT PERFORMANCE OF AEROFOIL I I S AT $M_\infty \cong 0{\cdot}8$

FIG. 25

SYM	CONF	$C\mu$	θ_j°
⅄	IISJ	·02	85
▲	IIJ	·015	85
⊡	IIS	·020	
◈	IF2J	·020	85
◇	IJ	·020	85
+	IJ	·020	120
▼	II	0	
⊙	I	0	85
×	I	0	120

N.B. SHADED SYMBOLS ARE FROM TESTS IN REFS. 1 & 7

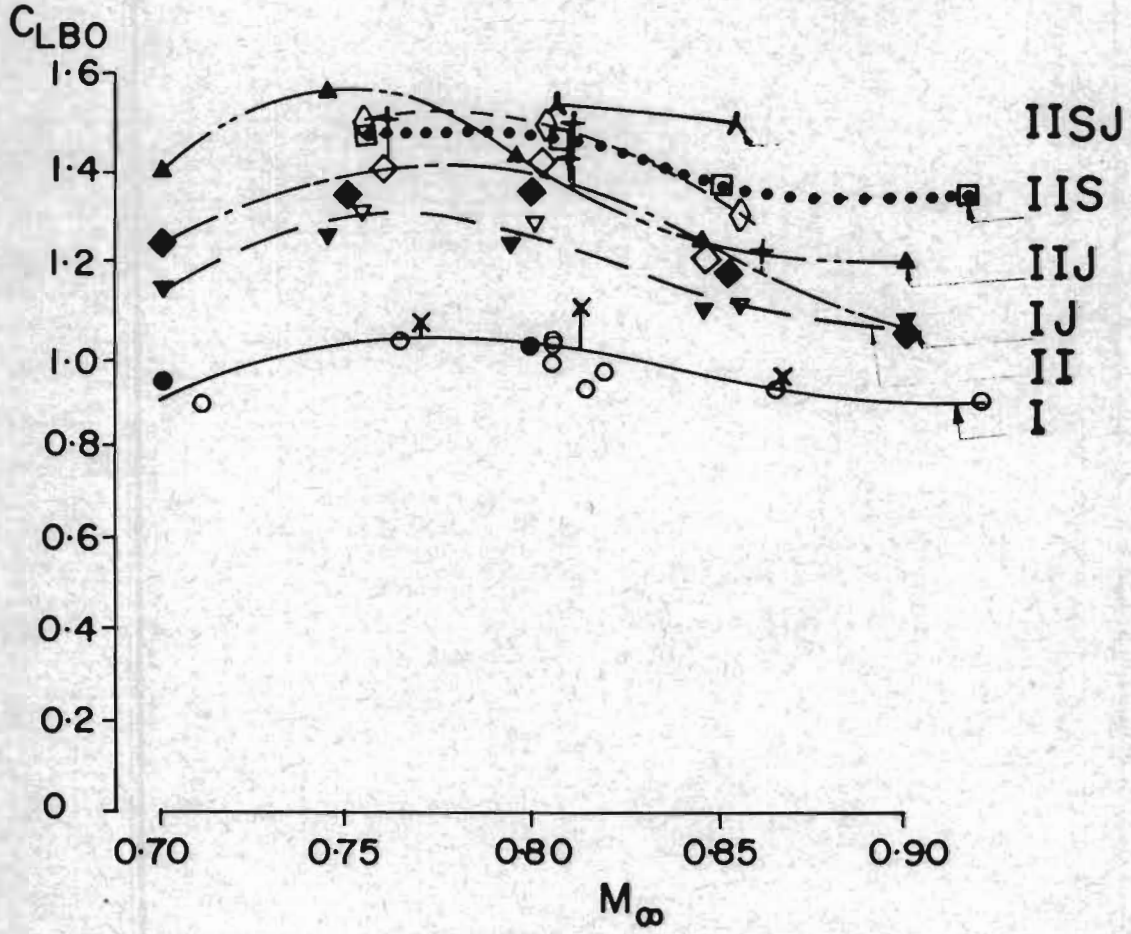

BUFFET ONSET PERFORMANCE FOR AEROFOILS I AND II

AT $R_C = 30 \cdot 10^6$

FIG. 26

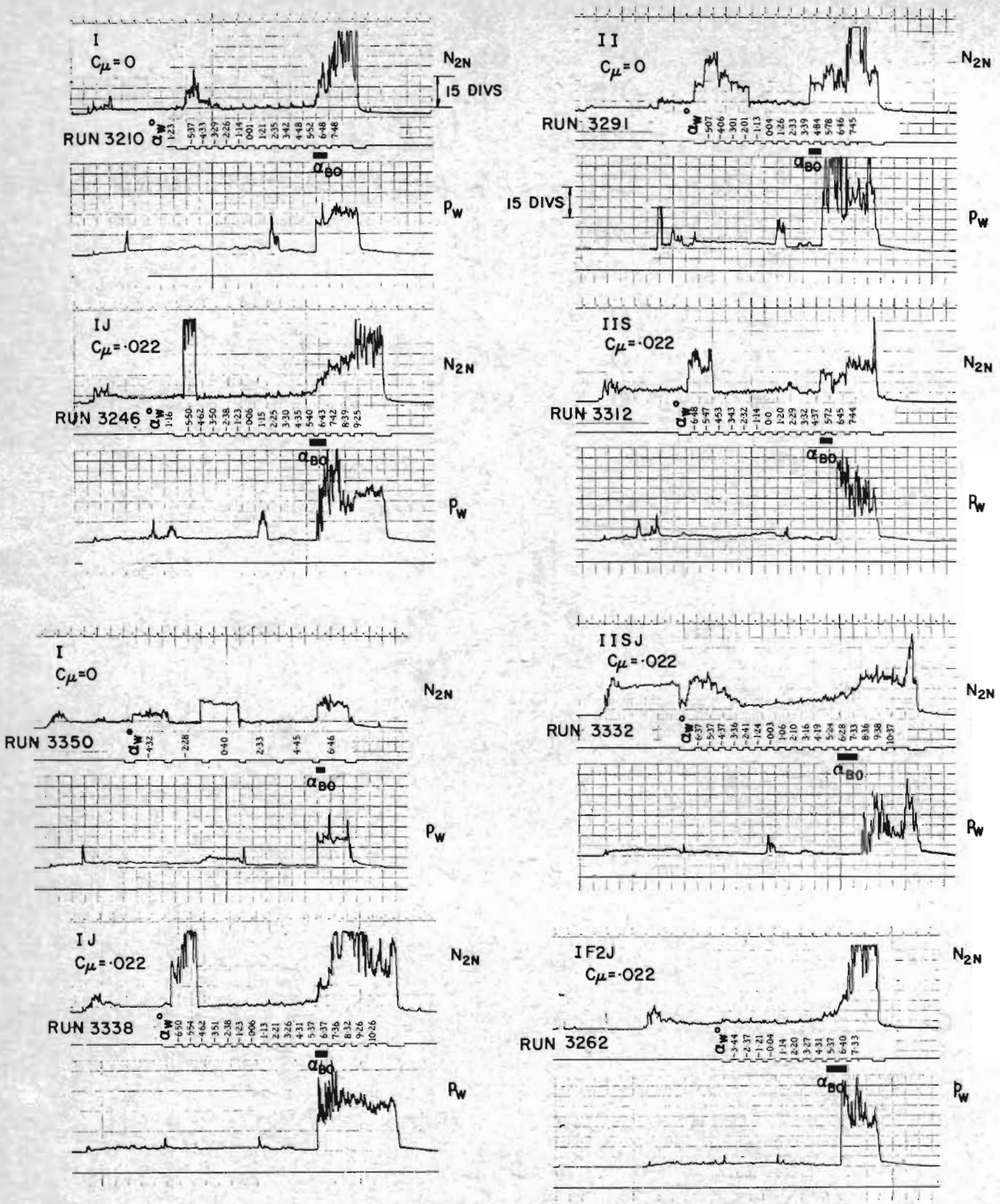

$N_{2N} = 4{\cdot}8n$ lb wt; $p_w = 0{\cdot}113n$ p.s.i; $q_\infty \tilde{=} 25{\cdot}1$ p.s.i; WING AREA 225 sqin
n = No OF DIVISIONS

OSCILLOGRAPH RECORDS OF RMS FLUCTUATING NORMAL FORCE AND SURFACE PRESSURE ON AEROFOILS I AND II AT $M_\infty \tilde{=} 0.8$

FIG. 27.1

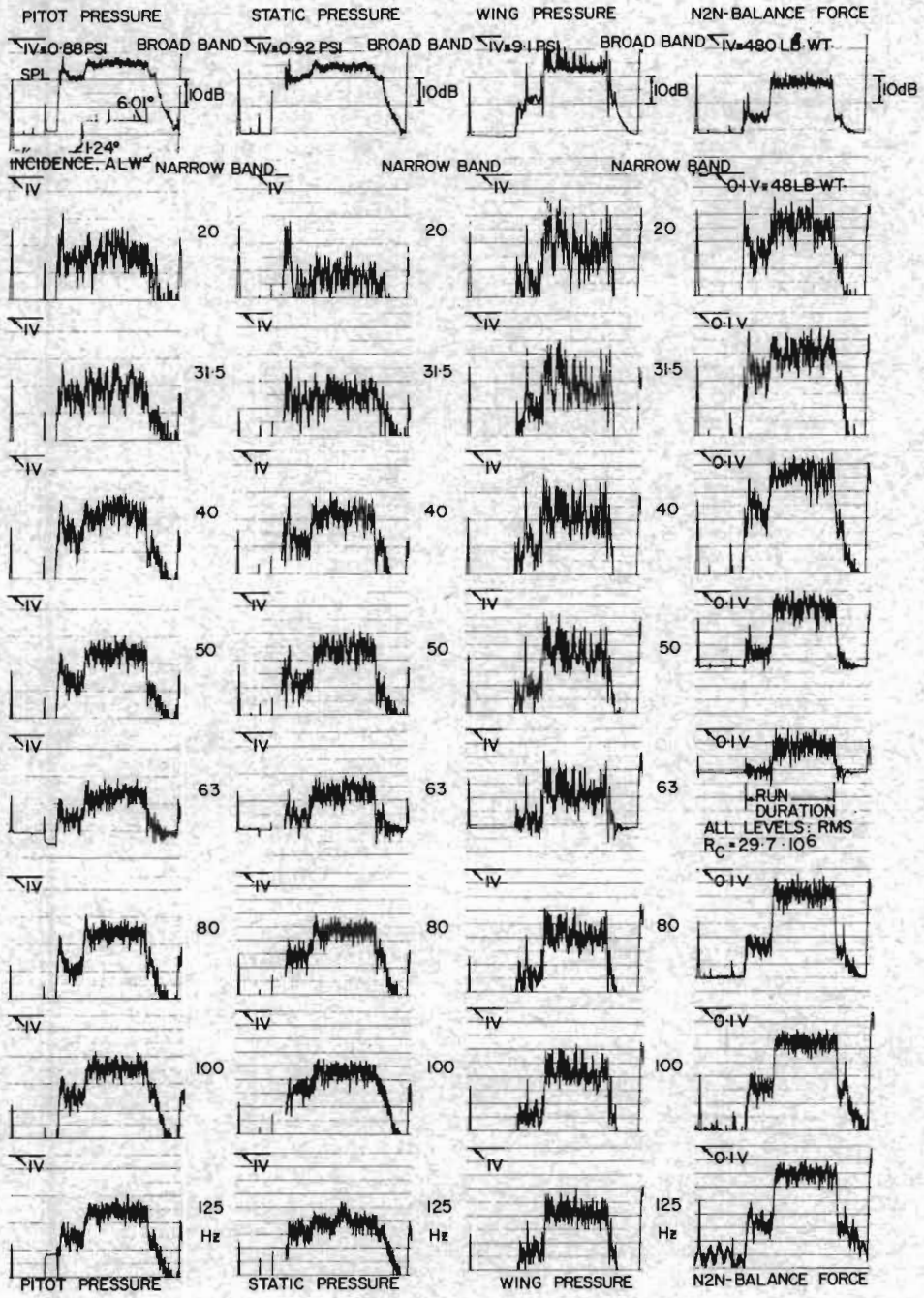

RESULTANT BROADBAND OUTPUTS AT CRUISE AND BUFFET ONSET: RUN 3287

PITOT Δp rms			STATIC Δp rms			WING Δp rms			BALANCE N_{2N} rms		
CR	BO		CR	BO		CR	BO		CR	BO	
156	161	dB	155	159	dB	159	172	dB	13·5	60·5	lb.wt.
0·18	0·31	psi	0·17	0·26	psi	0·26	1·14	psi	0·002	0·011	ΔC_N rms
0·7	1·3	$\%q_\infty$	0·7	1·1	$\%q_\infty$	1·0	4·6	$\%q_\infty$			

BROADBAND AND NARROW BAND (1/3 OCTAVE CENTRE FREQUENCY: f = 20 - 125 Hz) FLUCTUATING PRESSURES AND FORCES VERSUS RUN TIME.

FIG. 27.2

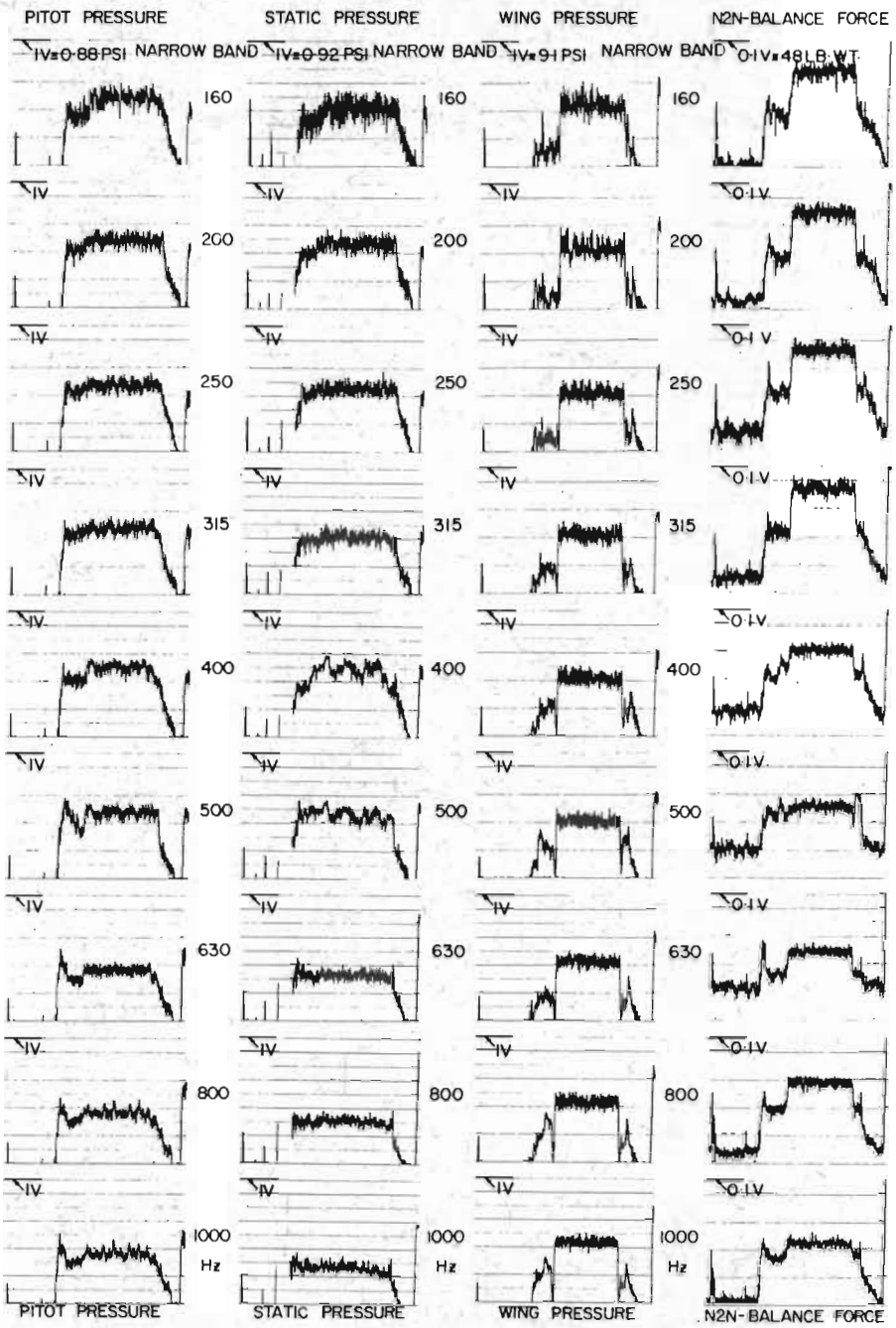

MEAN LEVELS FOR RUN 3287

$M_\infty = 0{\cdot}819$, $q_\infty = 24{\cdot}8$ psi, $p_o = 83{\cdot}2$ psi, $R_c = 29{\cdot}7$ million

$\alpha_w = 1{\cdot}24^\circ$ at cruise, $C_L = 0{\cdot}592$

$\alpha_w = 6{\cdot}01^\circ$ at buffet onset, $C_L = 0{\cdot}956$

BROADBAND AND NARROW BAND (1/3 OCTAVE CENTRE FREQUENCY, f = 160 - 1000 Hz) FLUCTUATING PRESSURES AND FORCES VERSUS RUN TIME

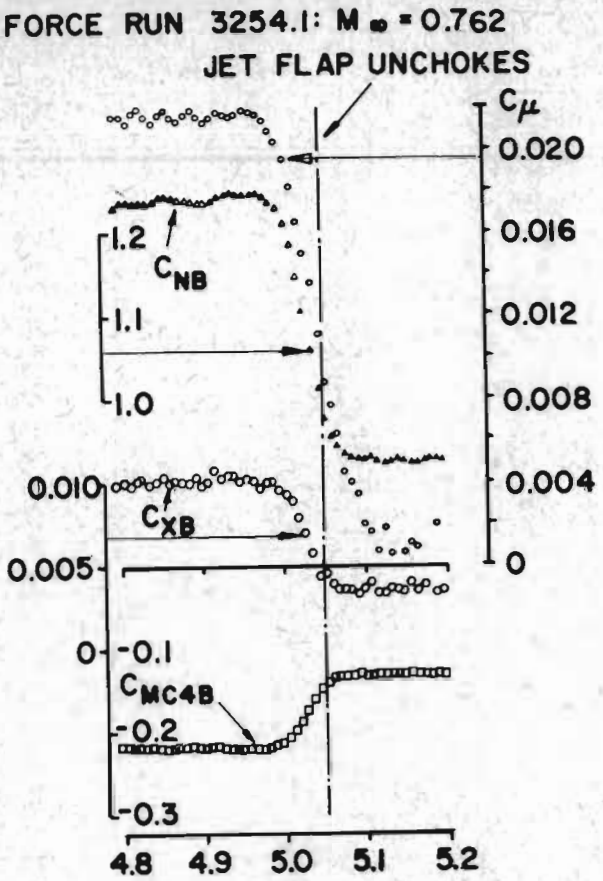

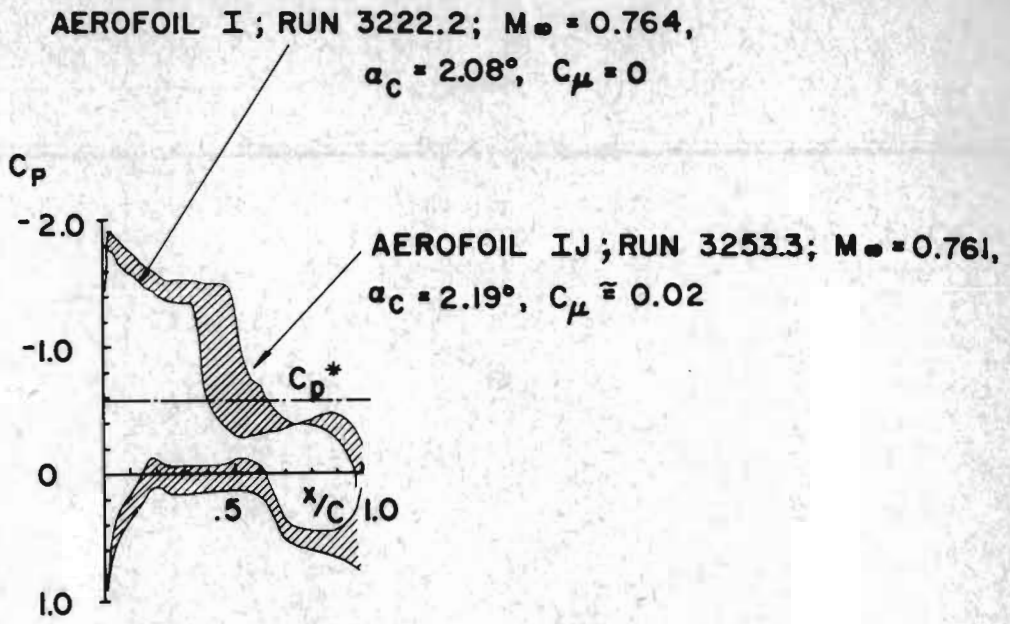

STEADY STATE PRESSURE DISTRIBUTIONS

DECAY OF JET FLAP AUGMENTATION AT $M_\infty \cong 0.75$
FOR AEROFOIL I

FIG. 28

FIG. 29·1

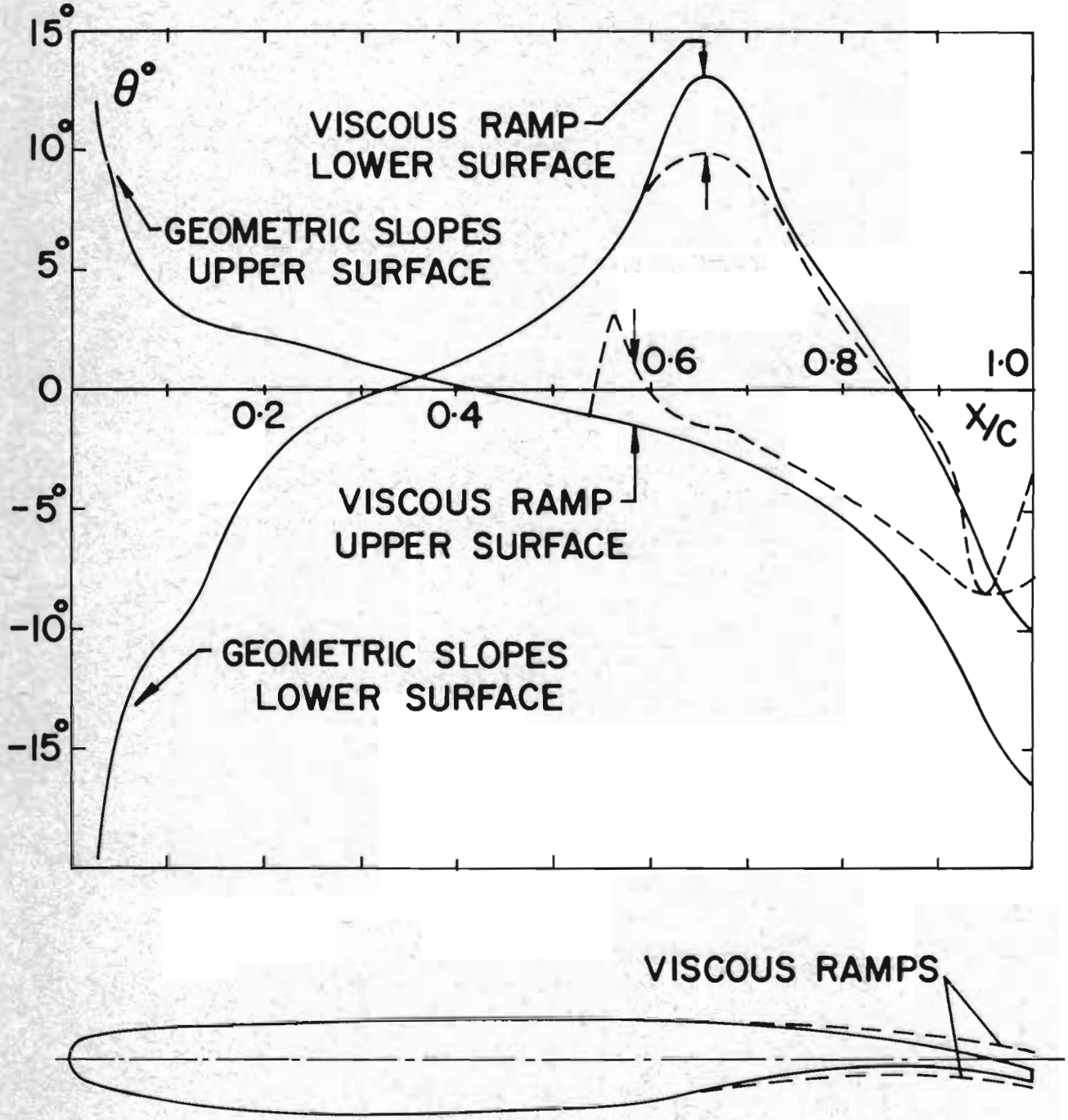

FINITE DIFFERENCE CALCULATION OF VISCOUS RAMP IN PRESENCE OF PERFORATED WALLS AT $M_\infty \cong 0{\cdot}8$

FIG. 29.2

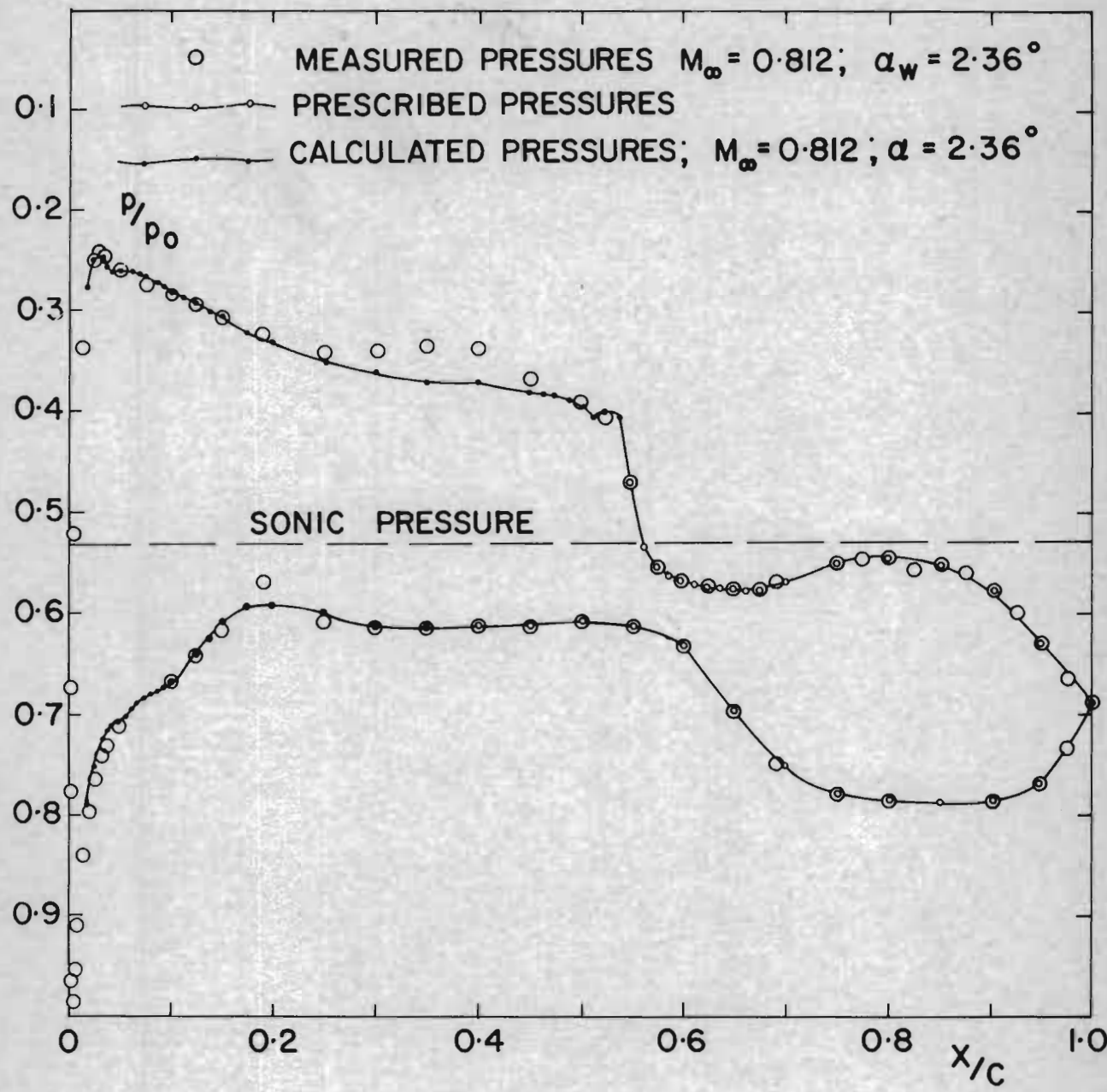

FINITE DIFFERENCE CALCULATION OF PRESSURE DISTRIBUTION IN PRESENCE OF PERFORATED WALLS AT $M_\infty \cong 0.8$

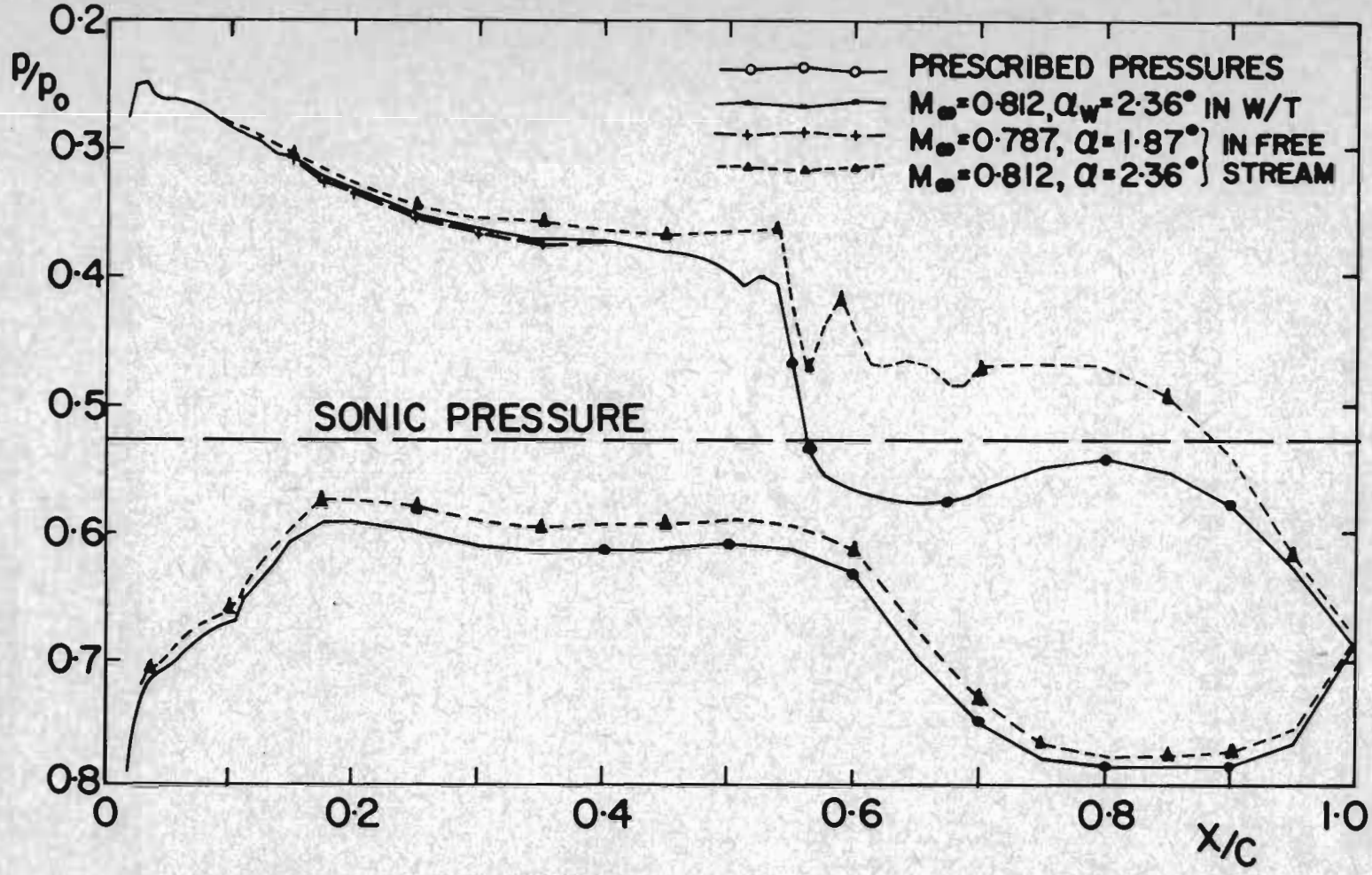

COMPARISON OF THE VARIOUS PRESSURE DISTRIBUTIONS FROM FINITE DIFFERENCE CALCULATIONS

FIG. 30

FIG. 31

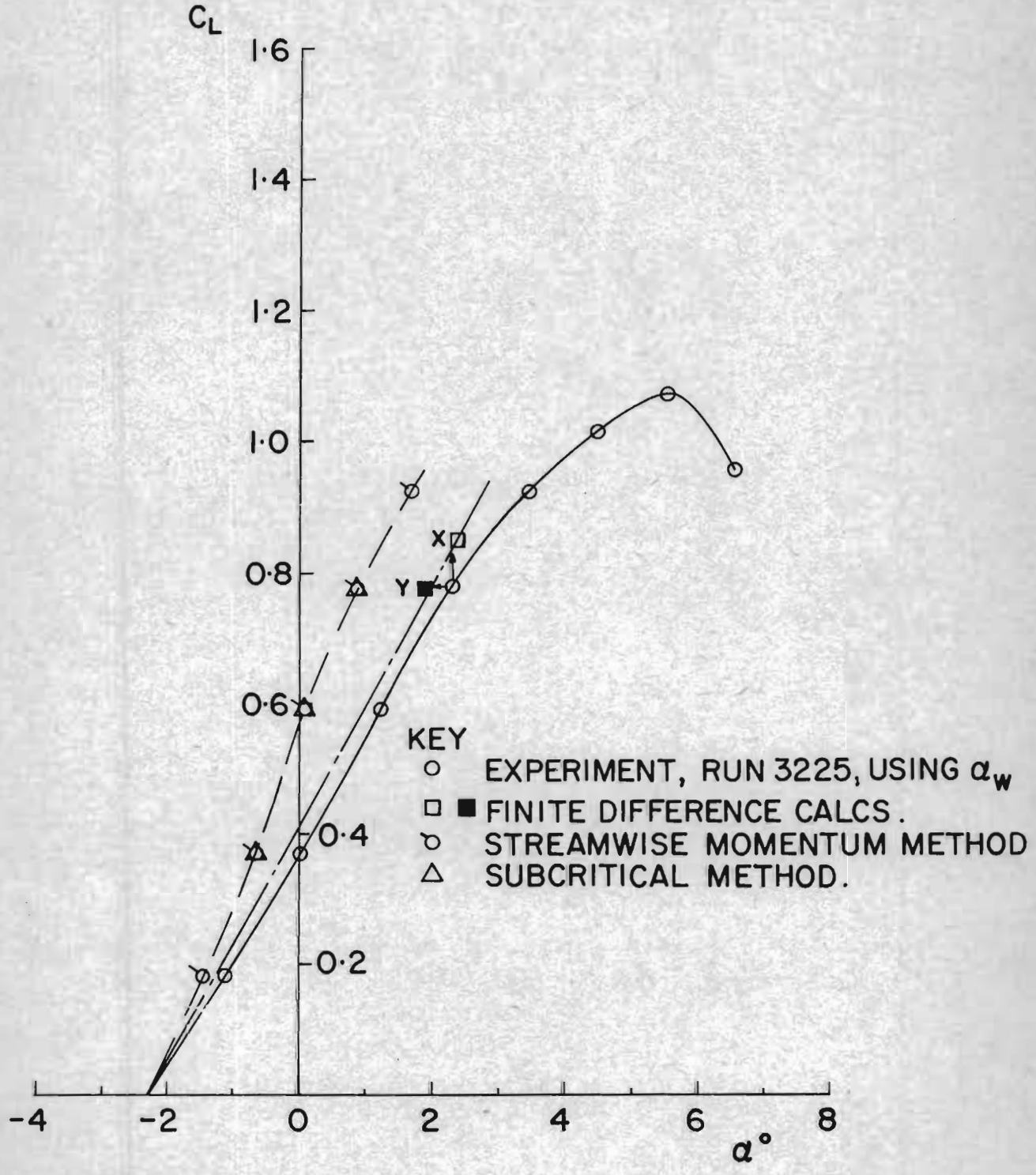

WALL INTERFERENCE CORRECTIONS TO LIFT CURVE SLOPE COMPARED AT $M_\infty \cong 0{\cdot}8$ AND $C_\mu = 0$ FOR AEROFOIL I

FIG.32

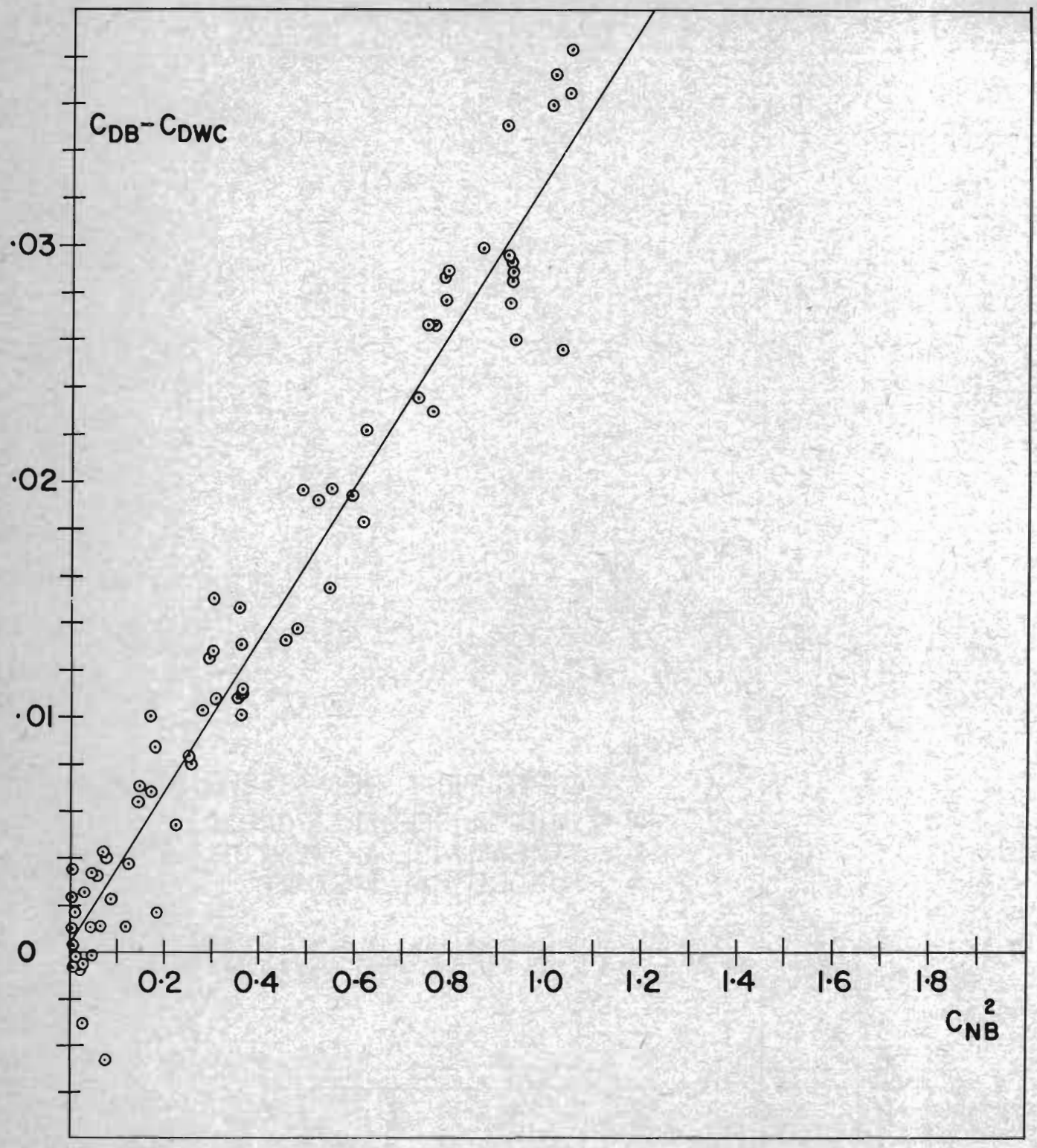

DETERMINATION OF K AND ΔC_{DO} FACTORS AT $M_\infty \cong 0{\cdot}81$ IN STREAMWISE MOMENTUM APPROACH TO WALL INTERFERENCE

FIG. 33

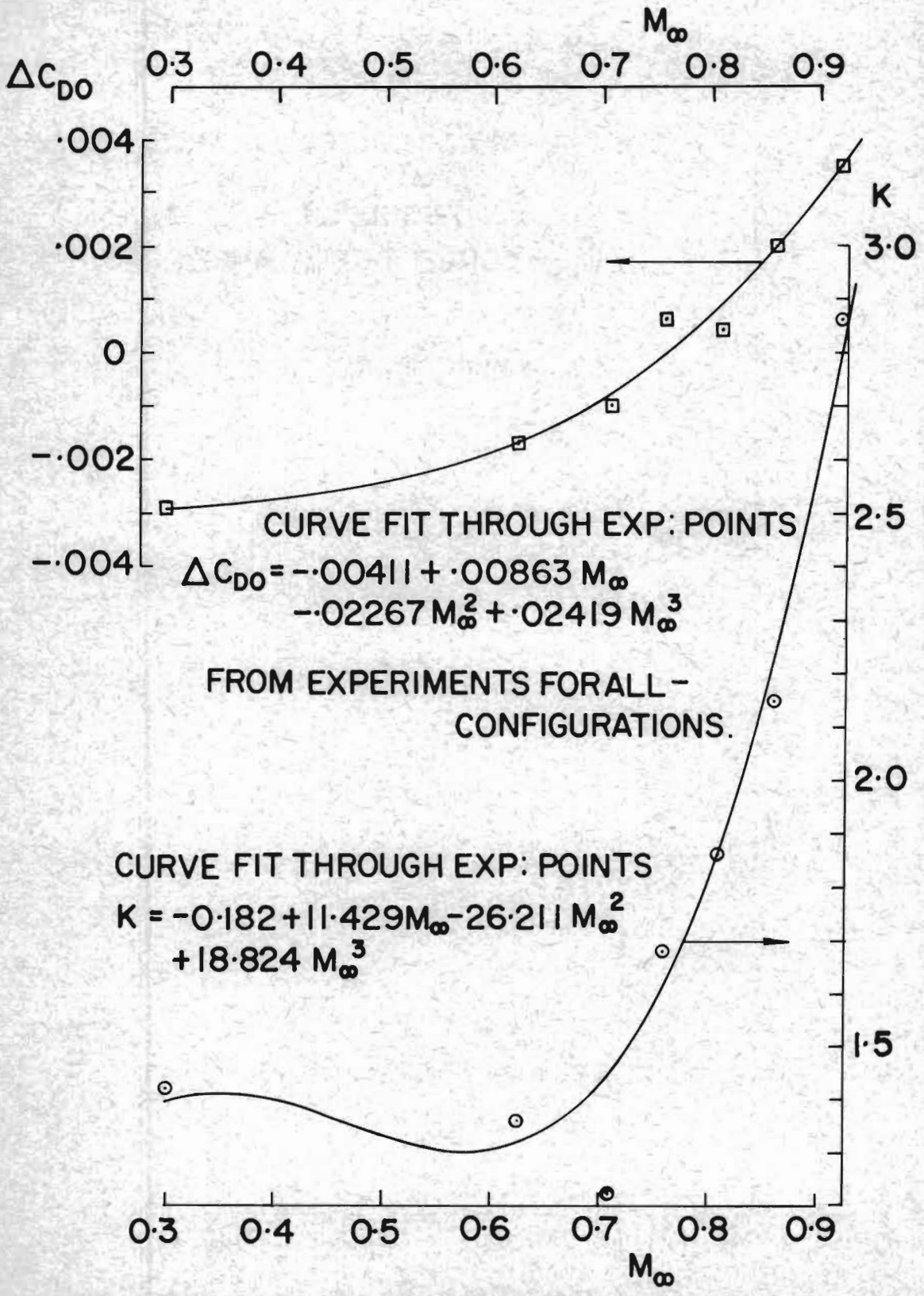

VARIATIONS OF WALL INTERFERENCE CORRECTION FACTORS, K AND ΔC_{DO} WITH M_∞

FIG.34

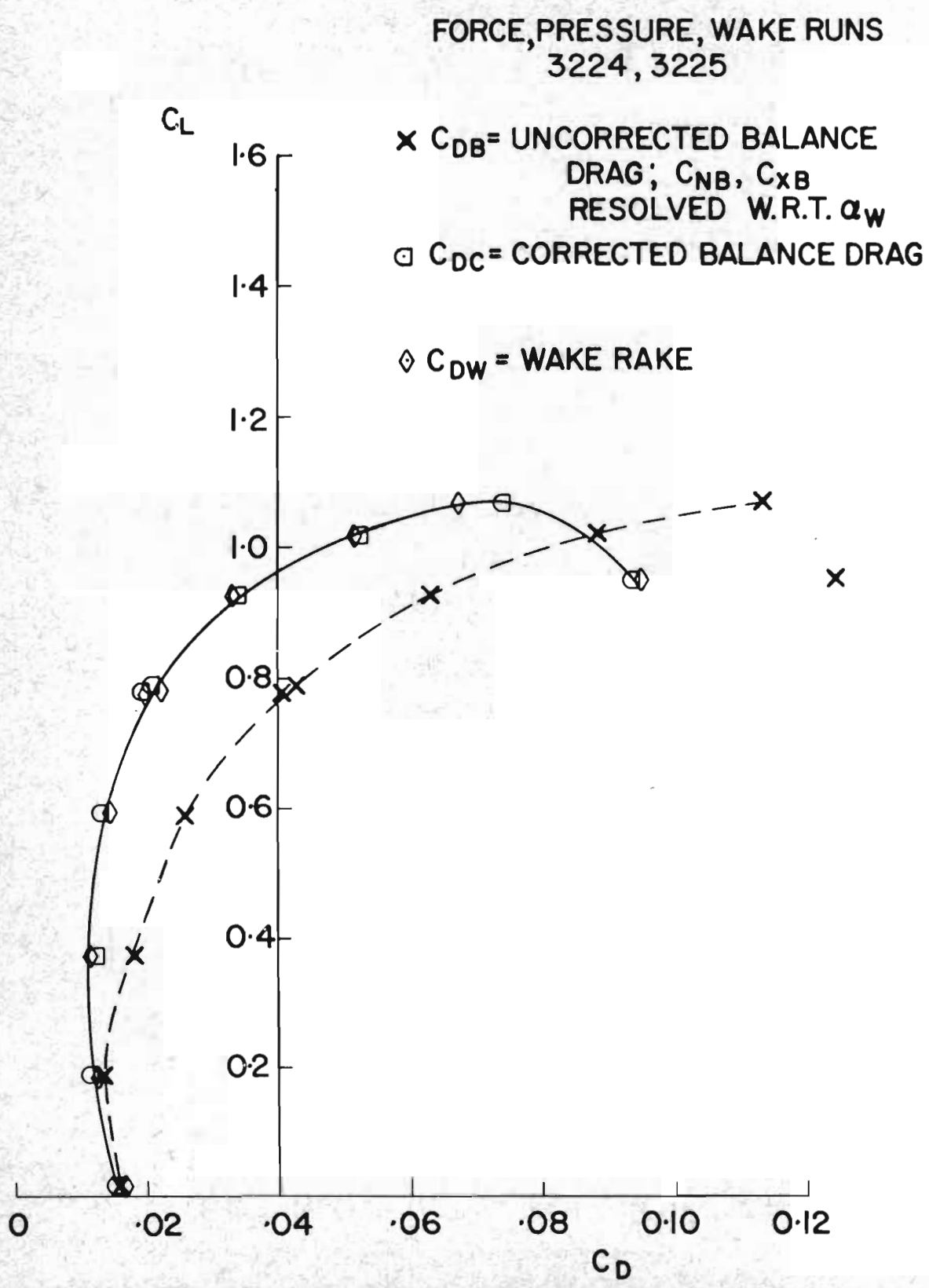

SAMPLE COMPARISON OF CORRECTED AND UNCORRECTED DRAG DATA AT $M_\infty \cong 0{\cdot}8$ FOR AEROFOIL I ($C_\mu = 0$)

FIG. 35

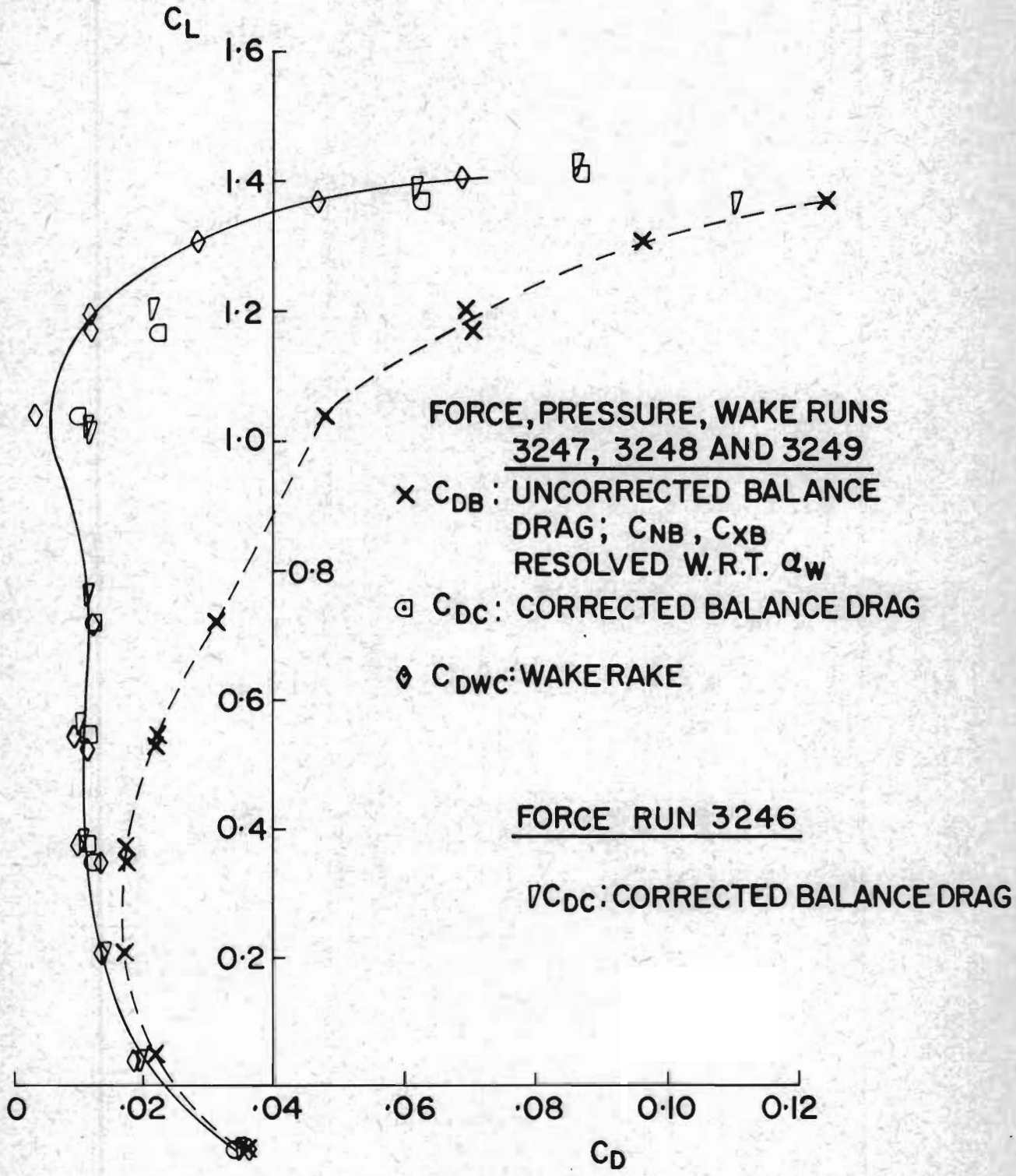

SAMPLE COMPARISON OF CORRECTED AND UNCORRECTED DRAG DATA AT $M_\infty = 0{\cdot}8$ FOR AEROFOIL IJ ($C_\mu \cong {\cdot}02$)

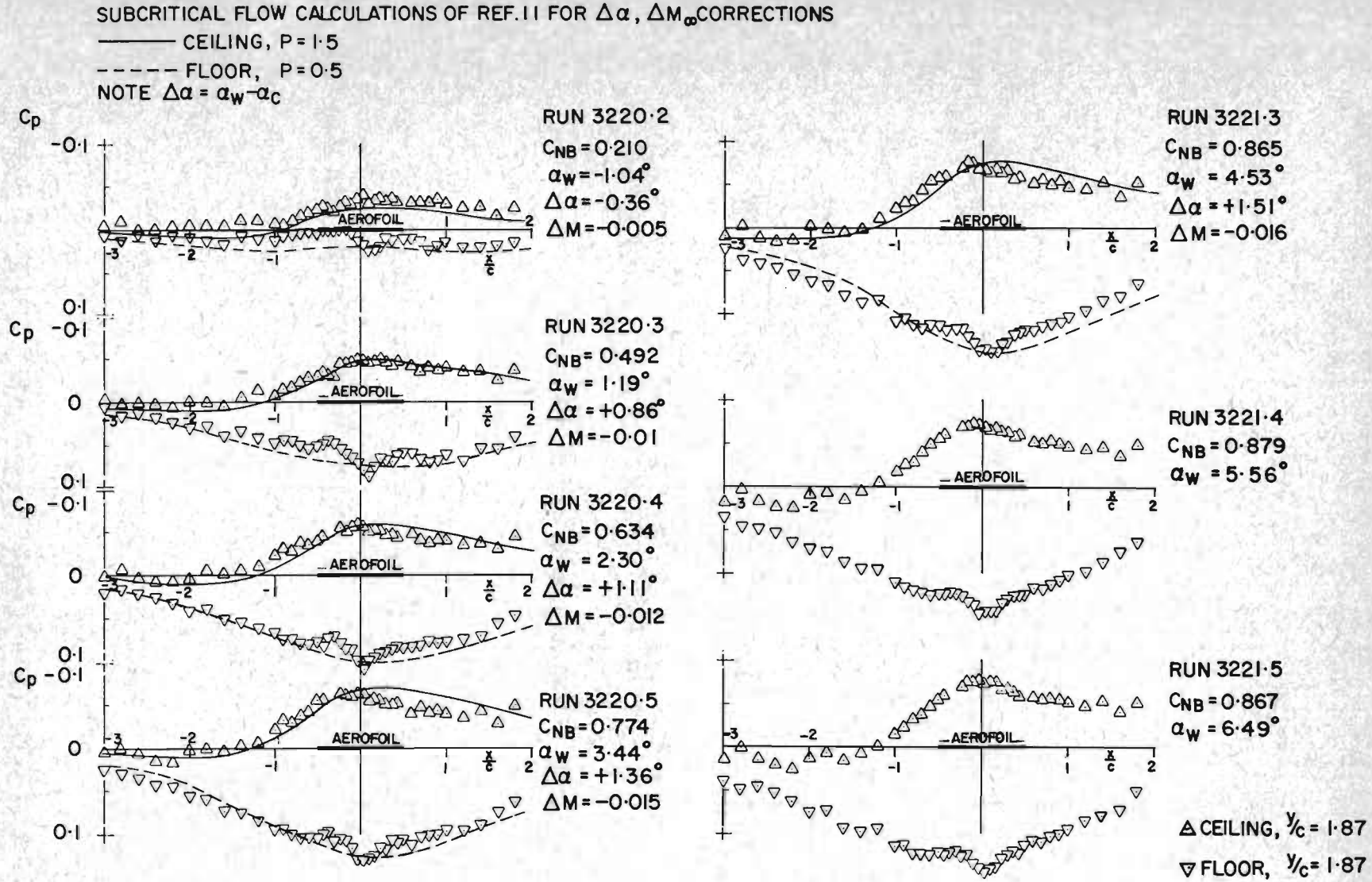

STATIC PRESSURE ADJACENT TO CEILING AND FLOOR OF 2D INSERT AT $M_\infty \cong 0.7$ FOR AEROFOIL I ($C_\mu = 0$)

FIG.36

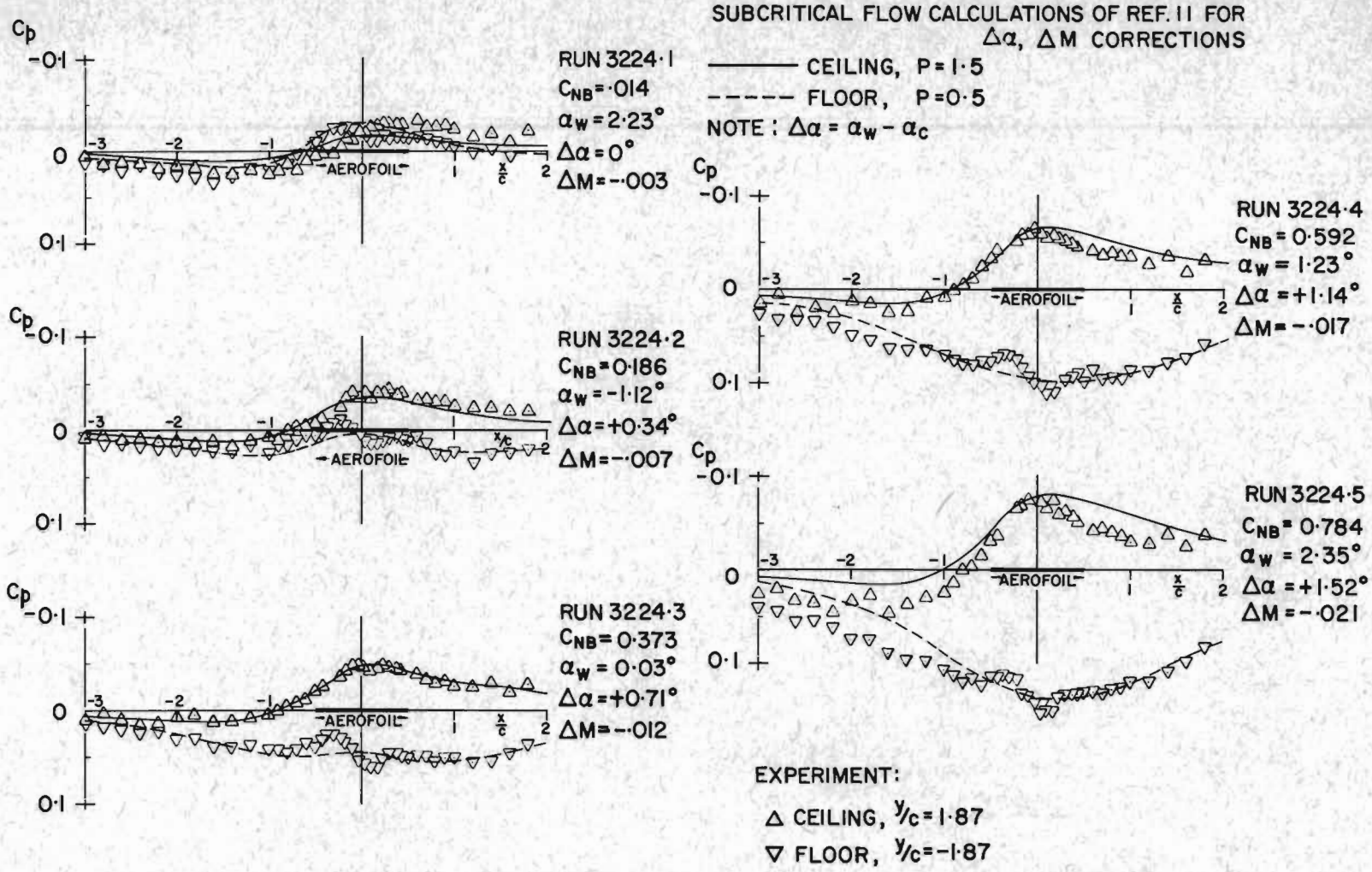

STATIC PRESSURES ADJACENT TO CEILING AND FLOOR OF 2D INSERT AT $M_\infty \cong 0{\cdot}8$ FOR AEROFOIL I ($C_\mu = 0$)

FIG 37·1

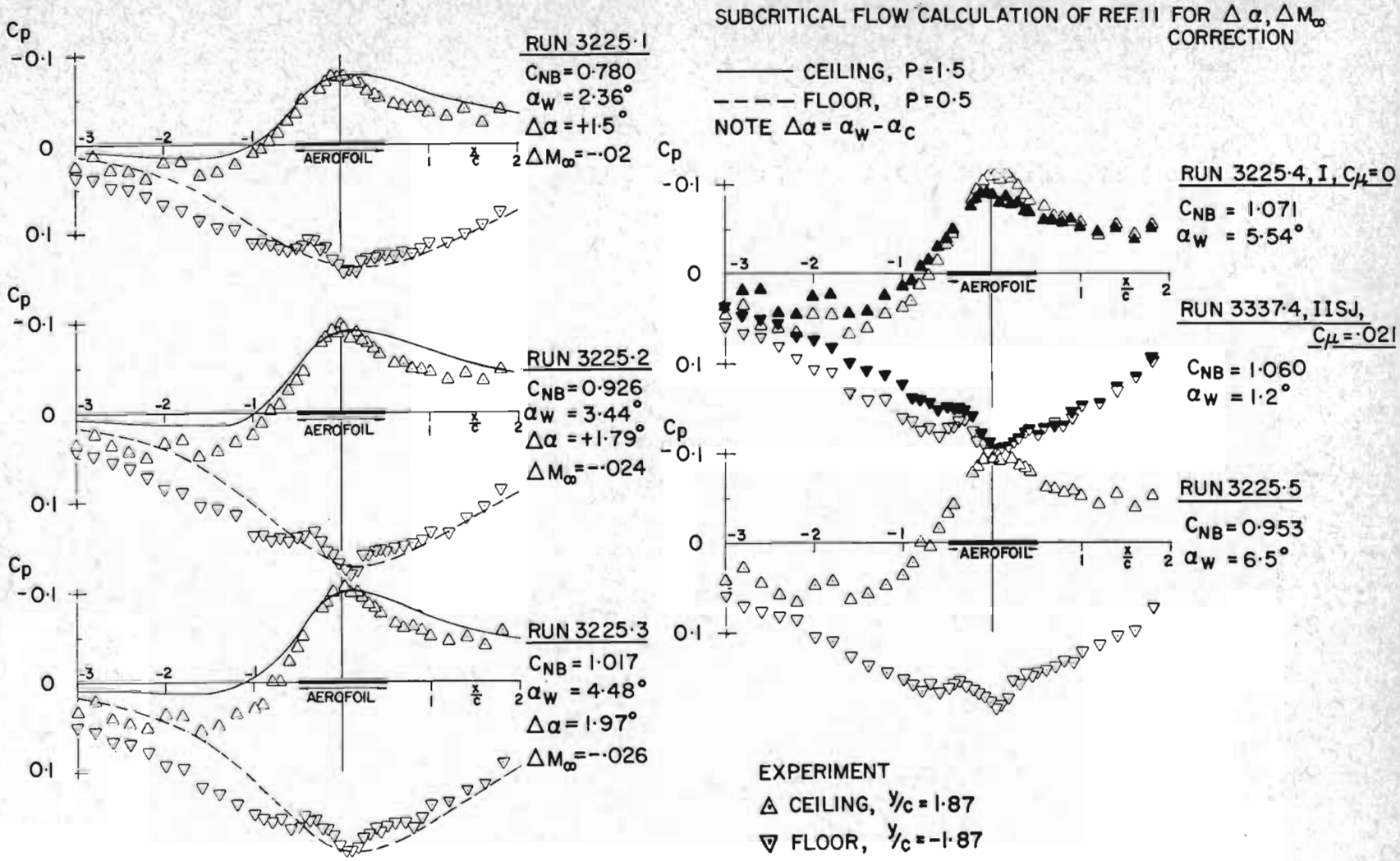

STATIC PRESSURE ADJACENT TO CEILING AND FLOOR OF 2D INSERT AT $M_\infty \cong 0.8$ FOR AEROFOIL I ($C\mu = 0$)

FIG. 37.2

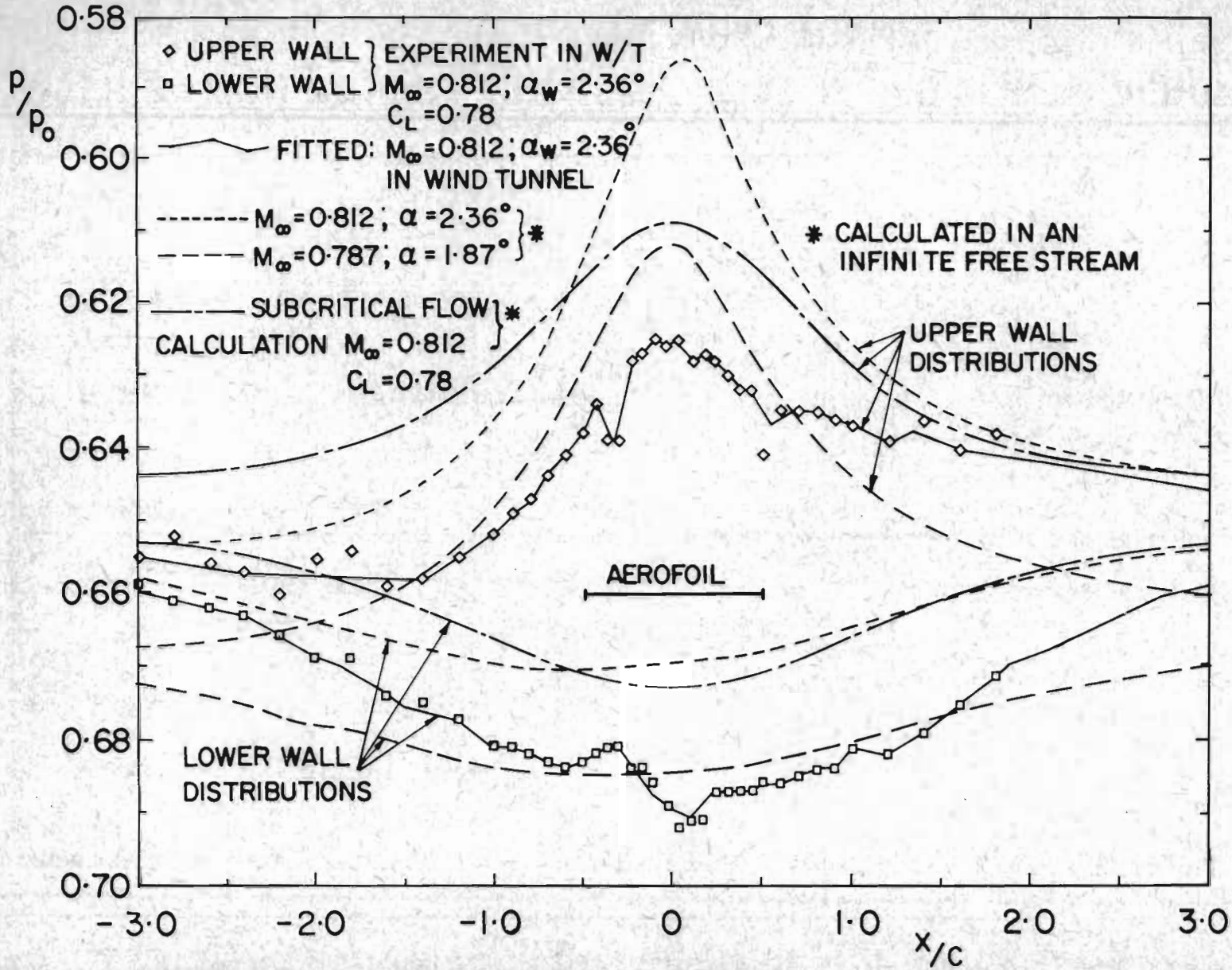

COMPARISON OF THE WALL PRESSURE DISTRIBUTIONS AT $M_\infty \cong 0{\cdot}8$ FOR AEROFOIL I

FIG. 38

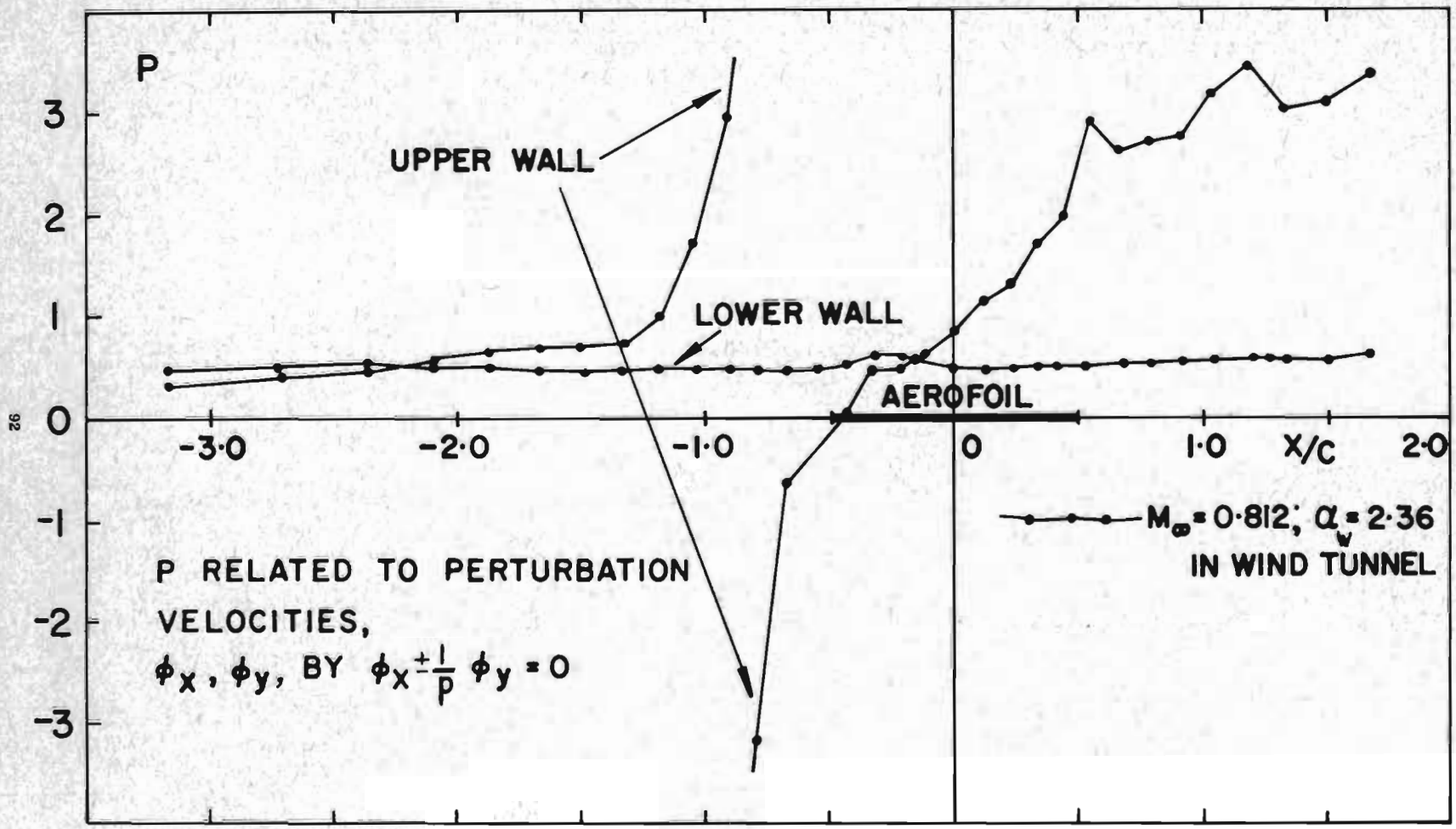

DISTRIBUTION OF WALL POROSITY P AT $M_\infty \cong 0{\cdot}8$ WITH AEROFOIL I IN THE WIND TUNNEL

FIG 39

D I S C U S S I O N

R. Legendre (ONERA, Chatillon, France): I did not have the opportunity to ask Dr. Whitcomb - what are the flutter characteristics of these supercritical wings? I suppose it is important to know them from a practical point of view.

D.J. Peake: Since at a given cruise Mach number, one is able to operate with a supercritical aerofoil section that is thicker than that of a conventional aerofoil, one might assume that the supercritical section would be more stable in bending and in torsion, and hence from the structural point of view, possess improved flutter characteristics.

B.G. Newman (McGill University, Montreal, Canada): Have you done any tests on the relative usefulness of vortex generators instead of blowing as a means of delaying shockwave boundary-layer separation?

D.J. Peake: No, we have not tried any tests with vortex generators. Pearcey, in Ref. 1, found relatively good comparison between the beneficial effects on separation produced by vortex generators and tangential injection. But the vortex generators may only be required for purposes of control in a restricted range of flight conditions. Hence if they are not retractable, they may be a source of unnecessary drag.

Reference 1:

Pearcey, H.H., "Shock-induced Separation and its Prevention by Design and Boundary-Layer Control", Part IV of Boundary Layer and Flow Control, Ed. by G.V. Lachmann, Pergamon Press 1961, pp. 1260-1333.

G.M. Lilley (University of Southampton, U.K.):
1. In the results of your various experiments you show that there exist downstream of shock waves regions of local separation or the formation of bubbles. This indicates that the results are likely to be dependent on Reynolds number. There are then the problems of Reynolds number effects associated with the boundary layer and the related effects of boundary layers with slot blowing and the jet flap. I should be pleased if you could indicate what experience there exists on Reynolds number effects on your results especially for the cases of jet flap and jet flap with slot blowing.
2. In the presentation of the results it seems that the use of the effective drag coefficient as the sum of C_μ and the measured wake drag coefficient is likely to be an overestimate since in a practical case the combined effect of recovery jet momentum and momentum inlet loss would be less than C_μ .

D.J. Peake: 1. The effects of Reynolds number on the performance of supercritical jet-flapped aerofoils were discussed in an earlier paper (2) where the chord Reynolds number was varied between 11 and 40 million. In brief, there is an improvement in suction pressure levels on the aerofoil top surface and a small shock wave movement downstream with increase of Reynolds number, as the scale of any separation bubble is reduced. In addition, there is an elevation in maximum lift coefficient, drag divergence Mach number and buffet onset lift coefficient with increase of Reynolds number.

Above a Reynolds number of 30 million, however, the relative gains in performance achieved by increasing the Reynolds number are small. The test conditions, here, were hence chosen to be at 30 million.

No tests at varying Reynolds number were tried with slot blowing in the present series, but again, we would expect to see only small changes above R_c = 30 million.

2. The definition of a total drag coefficient that is written as $C_D = C_{DWC} + C_\mu$, where C_{DWC} is the profile drag of the section and C_μ is the blowing momentum coefficient, is useful, since it accounts to some degree for the performance penalty arising from the necessity to use power to provide blowing from the slot and the jet flap (bleed from a compressor stage, for example). It has been used previously in tests with low speed circulation controlled aerofoils - see Ref. 3, for instance.

C_D probably will not be too much of an overestimate, particularly when the jet flap efflux is at $\theta_j = 85°$, for under these conditions, only a small thrust recovery is measured. We might interpret this to be caused by high mixing losses between the jet and mainstream, as the jet sheet leaves the aerofoil.

References:

2) Peake,D.J., Yoshihara,H.,et al "The Transonic Performance of Two-Dimensional, Jet-Flapped Aerofoils at High Reynolds Numbers", AGARD CP-83, 1971.

3) Kind,R.J., Maull,D.J., "An Experimental Investigation of a Low-Speed Circulation-Controlled Aerofoil", The Aeronautical Quarterly, Vol.19, May 1968, pp. 170-182.